PLASMONIC ENHANCED DYE-SENSITIZED SOLAR CELLS WITH PHTHALOYL CHITOSAN-BASED GEL POLYMER ELECTROLYTE

SHAHAN SHAH

FACULTY OF SCIENCE
UNIVERSITI MALAYA
KUALA LUMPUR

2023

PLASMONIC ENHANCED DYE−SENSITIZED SOLAR CELLS WITH PHTHALOYL CHITOSAN−BASED GEL POLYMER ELECTROLYTE

SHAHAN SHAH

THESIS SUBMITTED IN FULFILMENT OF THE REQUIREMENTS FOR THE DEGREE OF DOCTOR OF PHILOSOPHY

DEPARTMENT OF PHYSICS
FACULTY OF SCIENCE
UNIVERSITI MALAYA
KUALA LUMPUR

2023

UNIVERSITI MALAYA
ORIGINAL LITERARY WORK DECLARATION

Name of Candidate: **SHAHAN SHAH**

Registration No: **17051311/1 │ SVA170037**

Name of Degree: **Doctor of Philosophy**

Title of Thesis: **PLASMONIC ENHANCED DYE−SENSITIZED SOLAR CELLS WITH PHTHALOYL CHITOSAN−BASED GEL POLYMER ELECTROLYTE**

Field of Study:

EXPERIMENTAL PHYSICS (PHYSICS)

I do solemnly and sincerely declare that:

(1) I am the sole author/writer of this Work;

(2) This Work is original;

(3) Any use of any work in which copyright exists was done by way of fair dealing and for permitted purposes and any excerpt or extract from, or reference to or reproduction of any copyright work has been disclosed expressly and sufficiently and the title of the Work and its authorship have been acknowledged in this Work;

(4) I do not have any actual knowledge nor do I ought reasonably to know that the making of this work constitutes an infringement of any copyright work;

(5) I hereby assign all and every rights in the copyright to this Work to the Universiti Malaya ("UM"), who henceforth shall be owner of the copyright in this Work and that any reproduction or use in any form or by any means whatsoever is prohibited without the written consent of UM having been first had and obtained;

(6) I am fully aware that if in the course of making this Work I have infringed any copyright whether intentionally or otherwise, I may be subject to legal action or any other action as may be determined by UM.

Candidate's Signature   Date:

Subscribed and solemnly declared before,

Witness's Signature   Date:

Name:
Designation:

PLASMONIC ENHANCED DYE−SENSITIZED SOLAR CELLS WITH PHTHALOYL CHITOSAN−BASED GEL POLYMER ELECTROLYTE

ABSTRACT

In this work, light absorption improves with the use of plasmonic nanoparticles by photovoltaic (PV) devices. Silver (Ag, 100 nm size), gold (Au, 100 nm in size), copper (Cu, 60−70 nm in size) and platinum (Pt) nanoparticles (NP) added to the titanium dioxide (TiO$_2$) active layer of dye sensitized solar cells (DSSCs) have improved performance. The phthaloyl−chitosan based gel polymer electrolytes (GPEs) containing tetrapropylammonium iodide (TPAI) salt, 1−butyl−3−methylimidazolium iodide (BMII) ionic liquid (IL), tert−butyl pyridine (TBP), guanidine thiocyanate (GuSCN) as additives and (I^-/I_3^-) redox couple were used as an ion conducting medium for the DSSCs operation. The highest ionic conductivity 12.69×10^{-3} S cm^{-1} was exhibited by the GPE containing 3 wt.% GuSCN. The photocurrent density−photovoltage (J−V) characteristics, intensity modulated photocurrent spectroscopy (IMPS) and intensity modulated voltage spectroscopy (IMVS) were determined. On illuminating with AM1.5 (1000 W m^{-2}) light, DSSCs fabricated with 0 wt.% of NP constructed photoanode has exhibited comparatively low solar cell efficiency (η) of 4.59% with short−circuit current density J_{sc} of 9.90 mA cm^{-2} and open−circuit voltage V_{oc} of 0.69 V. The same cell also exhibited charge transport time τ_{tr} of 17.13 ms and charge recombination time τ_{rec} of 36.43 ms. On illuminating with AM1.5 light, the cell with 2 wt.% Ag NP in the photoanode exhibits an η of 6.99 %. The J_{sc} is 14.25 mA cm^{-2}, V_{oc} is 0.71 V and fill factor (FF) is 70%. The DSSC with photoanode containing 2 wt.% Ag NP also exhibits τ_{tr} of 7.00 ms and τ_{rec} of 87.22 ms. On illumination with AM1.5 light, the cell with 3 wt.% Au NP in the photoanode exhibits an η of 8.54% with J_{sc} of 19.82 mA cm^{-2}, V_{oc} of 0.72 V and FF of

60%. The same cell also exhibited τ_{tr} of 7.32 ms and τ_{rec} of 115.33 ms. Under the illumination of AM1.5, the DSSC with photoanode containing 3 wt.% of Cu NP exhibits higher η of 7.19% with J_{sc} of 13.35 mA cm^{-2}, V_{oc} of 0.76 V and FF of 71%. The same cell also exhibited the lowest τ_{tr} of 2.30 ms and τ_{rec} of 143.19 ms. Under the illumination of AM1.5, the DSSC with photoanode containing with 3 wt.% of Pt NP exhibits higher η of 6.54% with J_{sc} of 19.60 mA cm^{-2}, V_{oc} of 0.51 V and FF of 65%.

PLASMONIK MENINGKATKAN SEL SURIA TERPEKA PEWARNA DENGAN ELEKTROLIT POLIMER GEL BERASASKAN PHTHALOYL KITOSAN

ABSTRAK

Dalam kerja ini, penyerapan cahaya meningkat dengan penggunaan nanopartikel plasmonik oleh peranti fotovoltaik (PV). Nanopartikel (NP) argentum (Ag, saiz 100 nm), aurum (Au, saiz 100 nm), kuprum (Cu, saiz 60−70 nm) dan platinum (Pt) ditambah pada lapisan aktif titanium dioksida (TiO$_2$) sel suria terpeka pewarna (DSSC) telah meningkatkan prestasi. Elektrolit polimer gel (GPE) berasaskan phthaloyl−kitosan yang mengandungi garam tetrapropylammonium iodida (TPAI), 1−butyl−3−methylimidazolium iodida (BMII) cecair ionik (IL), tert−butyl pyridine (TBP), guanidine thiocyanate aditif dan pasangan redoks (I^- / I_3^-) digunakan sebagai medium pengalir ion untuk operasi DSSC. Kekonduksian ionik tertinggi 12.69×10^{-3} S cm^{-1} telah dipamerkan oleh GPE yang mengandungi 3 wt.% GuSCN. Ciri−ciri ketumpatan arus foto−fotovoltan ($J-V$), spektroskopi arus foto termodulat intensiti (IMPS) dan spektroskopi voltan termodulat intensiti (IMVS) telah ditentukan. Apabila dipancarkan dengan cahaya AM1.5 (1000 W m^{-2}), DSSC yang dipasang dengan 0 wt.% NP fotoanod telah menunjukkan kecekapan sel suria (η) yang agak rendah sebanyak 4.59% dengan ketumpatan arus litar pintas J_{sc} sebanyak 9.90 mA cm^{-2} dan voltan litar terbuka V_{oc} sebanyak 0.69 V. Sel yang sama juga mempamerkan masa pengangkutan cas τ_{tr} sebanyak 17.13 ms dan masa penggabungan semula cas τ_{rec} sebanyak 36.43 ms. Apabila diterangi dengan cahaya AM1.5, sel dengan 2 wt.% Ag NP dalam fotoanod mempamerkan η sebanyak 6.99%. J_{sc} ialah 14.25 mA cm^{-2}, V_{oc} ialah 0.71 V dan faktor isian (FF) ialah 70%. DSSC dengan

fotoanod yang mengandungi 2 wt.% Ag NP juga menunjukkan τ_{tr} 7.00 ms dan τ_{rec} 87.22 ms. Pada pencahayaan dengan cahaya AM1.5, sel dengan 3 wt.% Au NP dalam fotoanod mempamerkan η sebanyak 8.54% dengan J_{sc} sebanyak 19.82 mA cm^{-2}, V_{oc} sebanyak 0.72 V dan FF sebanyak 60%. Sel yang sama juga mempamerkan τ_{tr} sebanyak 7.32 ms dan τ_{rec} sebanyak 115.33 ms. Di bawah pencahayaan AM1.5, DSSC dengan fotoanod yang mengandungi 3 wt.% Cu NP mempamerkan η yang lebih tinggi iaitu 7.19% dengan J_{sc} sebanyak 13.35 mA cm^{-2}, V_{oc} sebanyak 0.76 V dan FF sebanyak 71%. Sel yang yang sama juga mempamerkan τ_{tr} paling rendah iaitu 2.30 ms dan τ_{rec} sebanyak 143.19 ms. Di bawah pencahayaan AM1.5, DSSC dengan fotoanod yang mengandungi 3 wt.% Pt NP mempamerkan η yang lebih tinggi iaitu 6.54% dengan J_{sc} sebanyak 19.60 mA cm^{-2}, V_{oc} sebanyak 0.51 V dan FF sebanyak 65%.

Kata kunci: Sel suria terpeka pewarna, Kesan plasmonik nanopartikel, Elektrolit polimer gel, Kekonduksian, Masa penggabungan semula cas, Masa pengangkutan elektron, Kecekapan pengumpulan cas.

ACKNOWLEDGEMENTS

Alhamdulillah, all admirations go to Allah SWT for giving me strength, patience and fitness in completing the PhD thesis. I am humbled to express my endless gratitude and gratefulness to my honourable GURU, Professor Dr. Abdul Kariem bin Haji Mohd Arof for his continuous guidance and inspiration in completing this research work. He was not only my academic mentor but also a pathfinder in almost every step through the uneven road to finish this thesis. Also, I would like to extend my thanks to my supervisor, Associate Professor Dr. Zul Hazrin bin Zainal Abidin for his continuous support and inspiration in this work.

To all my lab mates in Centre for Ionics Universiti Malaya (CIUM), thank you for the help, support and encouragement in completing this research work. As well, I would like to acknowledge all laboratory officers who have helped me to complete this research.

Moreover, my gratitude also goes to Department of Physics, Universiti Malaya for providing me the chemicals, instruments, equipment, facilities, and apparatus to complete my research work. Also, I would like to acknowledge the financial support form Fundamental Research Grant Scheme (FRGS) under the project No. FG029−17AFR as International Graduate Research Assistant (iGRA) as well as the tuition fee waiver under the Universiti Malaya International Graduate Assistant Scheme (iGRAS) from the Institute of Research Management & Monitoring (IPPP) of Universiti Malaya.

Last but not least, I would like to gratify my parents for their unceasing prayers, support and encouragement in this journey. I owe thanks to a very distinct person, my beloved siblings for their continuous and trustworthy love, sacrifice, support and understanding throughout the PhD study period. It would be highness to him to mention one of beloved friend Dr. Ikhwan Syafiq bin Mohd Noor who build me up during my

Universiti Malaya research journey and lab friends. Without such cooperation, I could not be able to finish this massive work within the stipulated time.

TABLE OF CONTENTS

LIST OF FIGURES

LIST OF TABLES

LIST OF SYMBOLS AND ABBREVIATIONS

η_{cc}	:	charge−collection efficiency
τ_{rec}	:	charge recombination time
τ_{tr}	:	electron transport time
V_{oc}	:	open−circuit voltage
J_{sc}	:	short−circuit current density
η	:	efficiency
R_b	:	bulk resistance
BMII	:	1−butyl−3−methyl imidazolium iodide
CE	:	counter electrode (CE)
CB	:	conduction band
DMF	:	dimethylformamide
DSSC	:	dye−sensitized solar cell
EIS	:	elecrochemical impedance spectroscopy
EC	:	ethylene carbonate
FF	:	fill factor
FTO	:	fluorine−doped tin dioxide
GuSCN	:	guanidinium thiocyanate
GPE	:	gel polymer electrolyte
HOMO	:	highest occupied molecular orbital
ITO	:	indium−doped tin oxide
IMPS	:	intensity modulated photocurrent spectroscopy
IMVS	:	intensity modulated photovoltage spectroscopy
IPCE	:	incident photon−to−current efficiency

LUMO	:	lowest unoccupied molecular orbital
LSPR	:	localised surface plasmon resonance
NREL	:	national renewable energy laboratory
PCE	:	photon conversion efficiency
PEO	:	poly(ethylene oxide)
PhCh	:	phthaloyl chitosan
PDSSs	:	plasmonic dye sensitised solar cell
PV	:	photovoltaics
RT	:	room temperature
SPR	:	surface plasmon resonance
TCO	:	transparent conducting oxide substrate
TBP	:	4−tertbutylpyridine
TPAI	:	tetrapropylammonium
TCF	:	transparent conducting film

LIST OF APPENDICES

CHAPTER 1: INTRODUCTION

1.1   Introduction

Several energy sources in our world regulate our most basic or complex inventions. In 2013, the earth's most dominant natural energy sources were oil, which accounted for approximately 32.9%, coal, which accounted for 30.1%, gases, 23.7%, and water and wind power, which accounted for 13.3%. Regarding the energy problem, several scientific leaders have expressed their opinion in reducing fossil fuel sources. The world's limited supply of fossil fuels poses a hazard to the next generation. Although fossil fuels are still the most often utilised energy source in the world, the Sun has a more abundant energy supply as a natural source around us. Solar photovoltaics (PV) is a low−carbon−emission energy technology, and the power usage has developed significantly. The cost of PV panel for residential has decreased from $12.4 per Watt in 1998 to $4.3 per Watt in 2014 (Feldman et al., 2015). Over the previous decades, solar PV has been nuch studied and developed compared to other power−producing technologies. At the end of 2019, capacity of solar PV has reached over 600 GW (Victoria et al., 2021) and photovoltaic electricity has the potential to satisfy these demands. Nonetheless, these costs have had a significant impact on global economic policies and have increased investment. Renewable energy is responsible for 2.7% of world energy consumption and 5.3% of overall power production (BP Statistical Review of World Energy 2014). This shows solar energy offers many applications in our daily use. Photovoltaic research has been pioneered from a material with highly atomic packed silicon−based solar cells, which have shown improvement results in efficiency levels from its inception to the present. Due to these solar cells' high production costs, the silicon solar cell industry has reduced the cost of electricity per Watt from 100 USD to 4 USD during the previous 20 years.

Unrenewable energies include highly utilised hydrocarbons have generated large quantities of pollutants such as CO_2, CH_4, hexafluoroethane, nitrogen trifluoride, nitrous oxide, sulfur hexafluoride, and tetrafluoromethane. CO_2 gas emitted from the burning of coal can reach one kg $kW^{-1}h^{-1}$. These greenhouse gases can contribute to other pollutants as well (Hameed & Dignon, 1988; Judkins & Fulkerson, 1993; Streets & Waldhoff, 2000). They give rise to respirational or breathing issues as a result of haze and air contamination. These can influence climate change due to heat trapping. Further implications of climate change produced by greenhouse gases include severe weather conditions, shortages of food availability and increasing infernos. Numerous countries have joined in the "Kyoto Protocol to the United Nations Framework Convention on Climate Change" to launch an endeavour to minimize the emission of greenhouse gases (Kyoto Protocol to the United Nations Framework Convention on Climate Change, 1997 & 1998). Solar energy, which is clean and sustainable, is one optimistic option for overcoming this difficulty.

Solar cell technology may be divided into three generations based on the date of their initial implementation. Progress in solar cell technology can be categorizeded into three generations. Solar cells of the first−generation include those fabricated using single crystalline or polycrystalline silicon wafers. Due to their high and consistent industrial performance, silicon cells have captured the market (Pastuszak & Węgierek, 2022). The performance of these first−generation cells is outlined below:

- Single crystalline silicon solar cells: Figure 1.1 depicts the photon conversion efficiency (PCE) of crystalline silicon solar cells achieved (Lameirinhas et al., 2022). One of the highest ever reported power conversion efficiencies (PCE) for silicon solar cells was 26% in 2017 (Yoshikawa et al., 2017).

- The efficiency of polycrystalline silicon solar cells has been shown to be about 23.3% achieved (Lameirinhas et al., 2022) as illustrated in Figure 1.1.
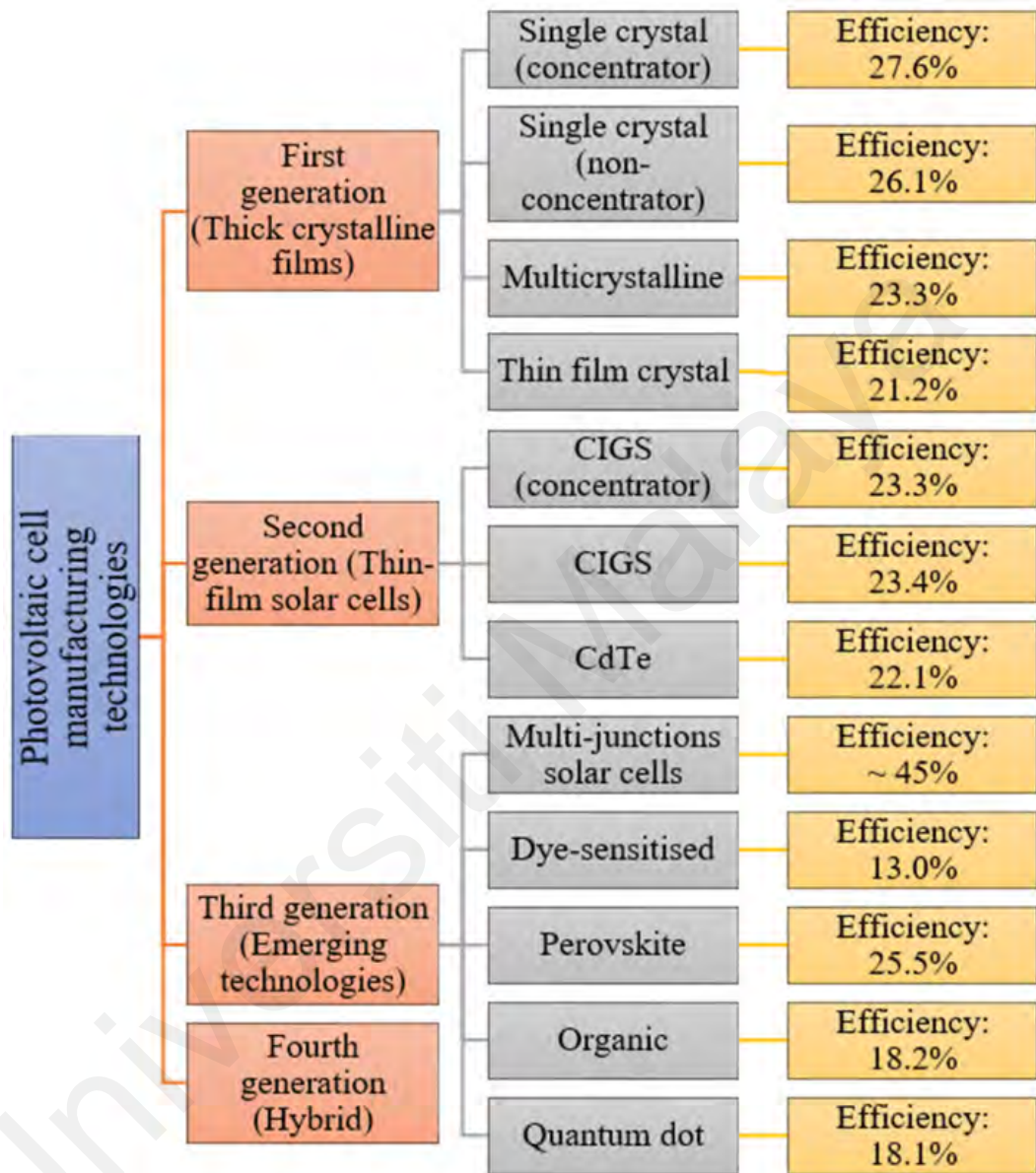
Figure 1.1: Examples of photovoltaic cell efficiencies achieved (Photo sourced from Lameirinhas et al., 2022).

Despite their lower efficiency, single crystalline solar cells are easily marketable since they are cheaper to manufacture. Second−generation solar cells are the thin−film cells. These cells consist of semiconductor layers that are several micrometers in thickness and display lower efficiencies than those of the first−generation. The second−generation cells,

on the other hand, are significantly cheaper to manufacture due to material savings and less expensive production procedures. There are three types of solar cells in this generation: amorphous silicon (a−Si), copper indium gallium selenide (CIGS) and cadmium telluride (CdTe).

As mentioned above, amorphous−silicon (a−Si) solar cells are generally only a few microns thick. This is much thinner than crystalline silicon solar cells that are about 180 µm in thickness. The National Renewable Energy Laboratory (NREL) maintains a database of the highest confirmed research cell conversion efficiencies for various solar systems, dating back to 1976 (NREL's Best Research−Cell Efficiency Chart 2023) indicated in Figure 1.2.
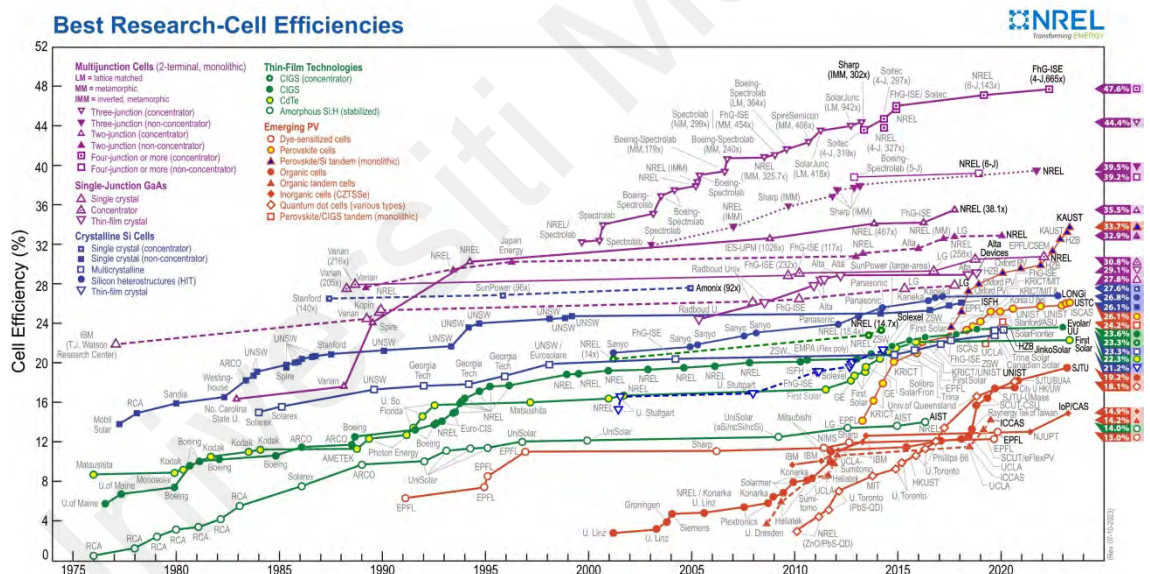
Figure 1.2: Photo sourced from NREL Best Research−Cell Efficiencies chart (NREL's Best Research−Cell Efficiency Chart, 2023).

Since the band gap of CdTe solar cells is 1.44 eV, its absorption spectrum matches the Sun. The laboratory efficiency of CdTe solar cells is 22.1% (Figure 1.1). The low efficiency and the use of rare and hazardous metals (such as Te and Cd), prohibit their extensive commodification. The laboratory efficiency of copper indium gallium

diselenide (CIGS) solar cells, as depicted in Figure 1.1, is 23.4%. However, mass manufacturing CIGS cells at reasonable pricing poses many problems (NREL's Best Research−Cell Efficiency Chart, 2022). This is due to the vacuum operating conditions required, the high temperatures involved in the manufacturing process and the lack of indium element.

The third−generation solar cells comprise a collection of scientific knowledge on the concentrator and tandem solar cells, organic solar cells, quantum dots sensitised solar cells and dye−sensitive solar cells. Other types of solar cells include perovskites and inorganic cell (CZTSSe) cell has efficiency about 24.2% and 13.0%, respectively shown Figure 1.2 The objectives of developing these cells is to improve power output and lifetime, decrease manufacturing costs, and create non−traditional items that offer market diversity. The progress of third−generation solar cells is still at the laboratory stage due to problems associated with poor efficiency, short lifespan, and high production costs.

Since its inception in 1991, dye sensitised solar cells (DSSCs) have proven more cost−effective photovoltaic devices than traditional silicon−based solar cells (O'Regan & Gratzel, 1991). The major reasons DSSCs are the best option for Si−based solar cells are their unique qualities such as low cost with moderate efficiency, energy generation in poor weather circumstances (cloudy or rainy days), and application to windowpanes and flexible substrates. Yet, commercialisation of these devices necessitates great stability with a life span of more than 20 years.

Plasmonic noble metals have gained popularity for enhancing light absorption and cell performance in various electrochemical devices, including dye−sensitised solar cells (DSSCs). Many difficulties remain to be addressed in order to ensure efficient DSSC performance. The capacity to capture and absorb the solar spectrum is difficult. The poor light absorption results in fewer electron−hole pairs produced, which may be understood

from the cell's short−circuit current (I_{sc}). Many ways have been proposed to improve incident light collection from the solar spectrum in PV cells. The use of DSSCs is perhaps the most common technique for increasing absorption. Photoanode using plasmonic noble materials on TiO₂ surface modification. Before departing, light impinge on the changed surface is dispersed and experiences many internal reflections. When light is internally dispersed, the effective optical path length in the absorbing layer of the cell is longer, allowing for higher optical absorption. Recent work in this field includes attempting to improve the plasmonic materials composition in the photoanode film in order to maximise absorption.

1.2 Characteristics of Sunlight

The Sun emits electromagnetic radiation from nuclear fusion processes, with a spectrum distribution that varies with its body temperature. The Sun's surface temperature is about 6000 K. At this temperature, the Sun behaves like a black body, releasing light in the visible area (300 nm to 700 nm) with the highest energy peak in all temperature values. AM0 is the light that remains after passing through the Sun's atmosphere. Because of the variable transmissivity of the Sun's atmosphere for each wavelength, the energy distribution spectrum of AM 0 differs from that of a black body (6000 K). The Sun is straight overhead in the AM1.0 state. AM1.5 (when the Sun is at mid−latitudes) is approved as a benchmark for photovoltaic works with a total power density of 1000 W m⁻². Figure 1.3 depicts an energy distribution versus wavelength plot for AM0, AM1.5, and 6000 K black bodies (Villalva et al., 2009).
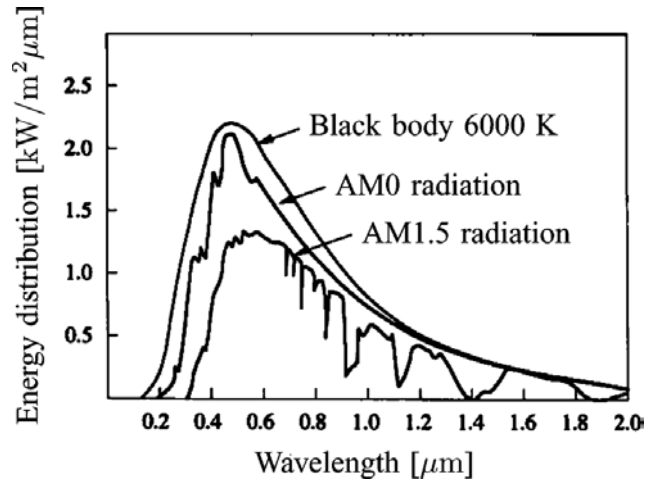
Figure 1.3: Spectral solar energy distributions of black body, AM0 and AM1.5 (Photo sourced from Villalva et al., 2009).

AM0 is the light that remains after passing through the Sun's atmosphere. Because of the variable transmissivity of the Sun's atmosphere for each wavelength, the energy distribution spectrum of AM0 differs from that of a black body (6000 K). The Sun is straight overhead in the AM1.0 state. AM1.5 (when the Sun is 480 degrees above the horizon) is approved as a benchmark for photovoltaic works with a total power density of 1000 W m^{-2}. Figure 1.3 depicts an energy distribution vs. wavelength plot for AM0, AM1.5, and 6000 K black bodies (Villalva et al., 2009).

1.3   Light with Plasmonics

Stuart and Hall described using metal island films to improve light absorption in silicon−on−insulator (SOI) waveguides in 1996 (Peter & Alkaisi, 2019; Stuart & Hall,1996). In this study, they achieved improved photocurrent in a p−n junction by adding tiny metallic particles on top of a 160 nm thick device layer on a substrate. They proposed at the time that the particles had a plasmon mode that was connected into the active device area. The particles do, in fact, display a localised surface plasmon resonance

(LSPR), which may be exploited to couple and scatter light into the absorbing layer of a solar cell.

A LSPR develops when free electrons vibrate coherently in a restricted geometry. Chapter 2 has a more extensive description of plasmons. The capacity to scatter, divert, and pair light using nano−scaled particles has recently gained attention (Lal et al.,2007; Zixian et al., 2023). It may collect more light from the solar spectrum to the surface of plasmonic dye sensitized solar cells (PDSSCs) if used to photovoltaics. Tiny particles can be put across a passivated surface, resulting in a decrease in surface recombination velocity. This arrangement would reap all of the benefits of PDSSCs while yet keeping a simple and economical fabrication procedure.

1.4   Problem Statements

In this work, low−cost materials are used for DSSC fabrication. The processing procedure is simpler compared to that for first and second generation solar cells. DSSCs absorb more sunlight per surface area than silicon−based solar panels. This enables them to be one of the most efficient third−generation solar technologies. Application of plasmonic materials may help to improve solar light trapping and absorption in DSSCs. The novelty of this work includes the use of copper and platinum nanoparticles together with gold and silver nanoparticles in the fabrication and characterization of the DSSCs.

1.5   Goal of Study

The study's ultimate objective is to show and improve plasmon−enhanced absorption in a PV device. This will be accomplished through three key considerations:

i. To optimize the conductivity of gel polymer electrolytes with GuSCN.

ii. To study the outcome of different plasmonic materials on DSSC performance.

iii. To investigate the effect of plasmonic nanoparticles (NPs) on electron transport and recombination time in DSSCs.

1.6 Organization of Thesis

This chapter describes the global energy portfolio and gives incentives for using safer, greener, non−carbon−based energy sources. An appraisal of the existing status of photovoltaics is done, and the necessity for low−cost cells that absorb a substantial percentage of the solar spectrum is established.

Plasmonic enhanced absorption is briefly discussed as a method of increasing light capture in plasmonic enhanced dye sensitised solar cells. The following chapters will go into further detail on the use of plasmonics for improved absorption and demonstrate that it is a feasible, low−cost light management technique that will help PVs achieve grid parity.

In this thesis, the effect of plasmonic materials on the optical properties of gel polymer electrolytes and their impact on the PDSSCs performance were studied. The second chapter presents a theoretical background and a qualitative description of plasmons, followed by a literature review of an LSPR in various nanometerials (Zhang et al., 2018). The localised surface−plasmon resonance governs the unusual optical characteristics of noble−metal clusters and nanoparticles (Kunwar et al., 2019; Teo et al., 2019). The significant absorption caused by LSPR in the UV and visible regions of the electromagnetic spectrum allows for a wide range of applications. In this thesis, discussion on the physical consequences, which govern and control the optical properties

of noble−metal clusters in various size ranges, with a particular emphasis on the emergence phenomenon of the LSPR and, ultimately, the optimal nanoparticle morphology required to maximise plasmon enhanced absorption in a PV cell.

The methods of research will be addressed in chapter three. The following research methodologies will be presented in this chapter: production of photoanode, preparation of electrolytes, preparation of counter electrode, and building of nanomaterials doped photoanode.

In chapter four, charecterization of gel polymer electrolytes and dye sensitised solar cells (DSSCs) based on gold nanoparticles (Au NP) will be presented and analysed using several electrochemical instruments.

Similarly, Chapters five, six and seven discuss the findings obtained from plasmonic dye sensitised solar cells (PDSSCs) based on silver nanoparticles (NP), copper nanoparticles (NP), and platinum nanoparticles (Pt NP) utilising various electrochemical instruments. Chapter eight is a discussion chapter that emphasises on reasons for the results obtained and lastly, Chapter nine is the conclusion chapter that also includes some suggestions for future work.

CHAPTER 2: LITERATURE REVIEW

2.1 Introduction

Carbon−based fuels are sources of energy that cannot be replenished. These factors linked to environmental contaminants such as CO and CO_2 emission into the air are among the problems faced today. Attempts have been made to search for other energy sources to reduce dependence on fossil fuels, minimise cost and safeguard the environment (Ahuja & Tatsutani, 2009). It is commonly accepted that the use of renewable energy is the most promising approach (Twidell & Weir, 2015). Energy from the sun, wind, water and heat, is renewable energy. Solar cells, for example, can convert sunlight into electricity. Thus, with solar cells, electrical energy can be delivered even to remote areas reported by Australian Bureau of Agricultural and Resource Economics (2010). The absence of environmental pollution and greenhouse gases such as CO_2, CO and ozone gas (O_3) are advantageous. There are several types of photovoltaic cells (Chopra et al., 2004; Gong et al., 2012; Hagfeldt & Grätzel, 2000; Kong et al., 2005; Rowell & McGehee, 2011; Wang et al., 2002; Wurfel & Wurfel, 2009). These include Si, $CuInSe_2$, $CuInS_2$ and CdTe (Swami, 2012), triple−junction solar cells, for example, GaInP/InGaAs/Ge (Zhang et al., 2015), perovskites (Chopra et al., 2004) and solar cells hsensitised by quantum−dots (Zhang et al., 2015) or dyes (Bagher et al., 2015). In this thesis, the aim is to use plasmonic materials in DSSCs. Development of solar energy management inside the cell is another technique to boost efficiency (Olaimat et al., 2021).

Metals like Au, Ag, Cu and Pt are commonly used as nanoparticles in DSSCs (Liu et al., 2017; Olaimat et al., 2021). These nanoparticles are typically mixed with TiO_2 nanopowder before being used to fabricate TiO_2−Au, TiO_2−Ag, TiO_2−Cu and TiO_2−Pt nanocomposite films as photoanodes.

These noble metals can increase light absorbance in the photoanode of the solar cell. These metals are also classified as plasmonic materials (Chandrasekharan & Kamat, 2001; Kumar et al., 2022; Qureshi et al., 2020; Rho et al., 2018). The shape and size of these plasmonics control the scatter and absorption of light (Liu et al., 2017; Subas et al., 2012).

Nobel metals such as gold (Au) with atomic weight 196.1 g mol^{-1}, platinum (Pt) with atomic weight 195.1 g mol^{-1}, silver (Ag) with atomic weight 107.9 g mol^{-1} and copper (Cu) with atomic weight 63.6 g mol^{-1} will be used as plasmonic materials for DSSC application in this work. The electronic configuration of the above plasmonic elements is included in Table 2.1. The atoms of these plasmonic elements have one electron less to complete the d−orbital.

Table 2.1: Electronic configuration of plasmonic materials.

Materials	Electron arrangement
Gold (Au)	$[Xe]4f^{14}5d^{9}6s^{2}$
Platinum (Pt)	$[Xe]4f^{14}5d^{9}6s^{1}$
Silver (Ag)	$[Kr]4d^{9}5s^{2}$
Copper (Cu)	$[Ar]3d^{9}4s^{2}$

For gold, silver, copper and platinum listed in Table 2.1, an electron is expected to move into the d orbital from the s orbital, filling the d orbital. For Pt, the 6s subshell will be void of electrons.

The optical property of plasmonic materials such as absorbance and scattering, is described as the interaction of a material surface with electromagnetic radiation. Different materials exhibit different optical properties as a result of their physical, chemical and mechanical variations. The energy of an electromagnetic light beam is given by the

equation $E = \dfrac{hc}{\lambda}$. Here, E is the electromagnetic energy of the light beam, h is Planck's constant, and c is the speed of light in vacuum. The wavelength of the light beam is represented by λ. The intensity of electromagnetic light is equal to the total of the transmitted, absorbed and reflected light wave intensities. As the light travels from one medium to another, the total light density I_o can be expressed as $I_o = I_t + I_a + I_r$. Here, I_t is intensity of transmitted light, I_a is intensity of absorbed light and I_r is the intensity of reflected light.

2.2 Plasmonic Materials

Optical properties of plasmonic materials such as absorption and scattering occur when conductive electrons at the surface of the plasmonic materials collectively oscillate with the electromagnetic radiation that resulted from surface plasmon resonance (Barnes et al., 2003; Kunwar et al., 2019; Zhang et al., 2018; Zixian et al., 2023).

The incident light interacts with the electron cloud of the metal. If the electron cloud is considered as a plasma, then, the plasma or electron cloud can oscillate with a certain frequency. When this frequency equals the frequency of incident light (photons or electrons), then there is resonance. These plasmons being weak in energy can propagate only along the interface between the negative and positive permittivity of the materials or surface of metals and are referred to as surface plasmon resonance (SPR). Thus, SPR is the vibration of conducting electrons in the plasmonic medium that is in resonance with the frequency of the incoming light (Ravindran et al., 2013). When SPR occurs, the intensities of absorption and scattering can be higher than that of the bulk materials. Many nano−sized elements (e.g., Pt, Au, Cu and Ag), can combine with incident photons by creating surface plasmon resonances (Jiang et al., 2014; Kunwar et al., 2019; Zhang et

al., 2018; Zixian et al., 2023). Properties of plasmonic materials can be influenced by the shape and their permittivity (Xiao, 2012). The metallic nanoparticles (plasmonics) can scatter light, prolong light duration and improve light incorporation by creating more optical paths (Kunwar et al., 2019; Mathew et al., 2014; Zhang et al., 2018; Zixian et al., 2023). These nanoparticles with the wavelength from the UV−visible to the NIR through SPR are able to combine incoming photons (Jiang et al., 2014). The nano−plasmonics act as electron traps to allow separation of charges and to focus light energy (Atwater & Polman, 2010; Kunwar et al., 2019; Zhang et al., 2018; Zixian et al., 2023).

These plasmonic materials (Au NP, Ag NP, Cu NP and Pt NP) have an optical property like interaction between free electrons in a metals and photon energy. When free electrons at the surface of a metal get illuminated, they oscillate collectively and are called localised surface plasmons resonance. The plasmons absorb only the percentage of incoming light that oscillates with the same frequency as the plasmons themselves. In other words, the absorbed light and the plasmon are in resonance. The rest of the light, i.e., those that oscillate with other frequencies are reflected. Localised surface plasmon resonance technic may be used to build efficient solar cells (Olaimat et al., 2021).

In this chapter, the fundamentals of DSSC and properties of nanomaterials that can enhance performance of the plasmonic DSSC are discussed. The conducting electrons in the plasmonic material oscillate when exposed to light (Sovizi & Omrani, 2017). This gives rise to SPR absorption band. Noble metal nanoparticles must be included in the photoanode layer for SPR effects to be beneficial. These benefits include the ability to trap light in plasmonic cells (Link & El−Sayed, 1999), promoting more optical tracks and increase absorption of light (Ferry et al., 2008; Kunwar et al., 2019; Zhang et al., 2018; Zixian et al., 2023). With these benefits, the DSSC performance can be improved (Liang et al., 2014).

The noble metal−induced surface plasmon has the potential to increase optical absorption. Conductive electrons in the nano−metals collectively oscillate under the influence of light to produce the surface plasmon effect. For the negative charges or electrons to vibrate with light, the nanoparticle size should be less than the exciting light wavelength (Kunwar et al., 2019; Luan & Wang, 2014; Zhang et al., 2018; Zixian et al., 2023). The electromagnetic field is enhanced at the nanoparticle surface because the metallic permittivity (which is more negative at longer wavelengths) is almost opposite to the permittivity of the surrounding medium. The electromagnetic or force field is influenced by the frequency of the incoming light and properties of the nanoparticle.

Plasmonic materials are able to capture light in the nano−meter regime (Peter & Alkaisi, 2019; Schuller et al., 2010) and the interaction of electromagnetic field with matter have made plasmonic materials an important field of study in solar cells (Gangadharan et al., 2017; Gwamuri et al., 2013). Figure 2.1 shows the characteristics and applications of plasmonic nanostructures.
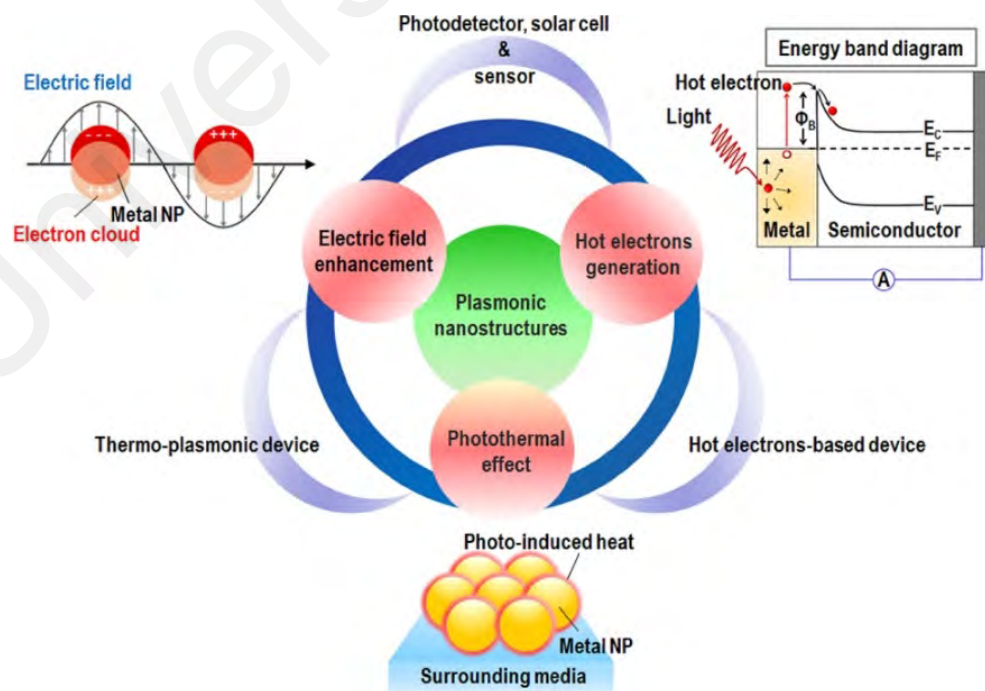
Figure 2.1: Characteristics and applications of plasmonic nanostructures (Photo sourced from Lin et al., 2020).

The maximum typical surface irradiance at sea level on a clear day is about 1000 Wm^{-2} (Frohlich & Lean, 2004). From Figure 2.1, it can be seen that plasmonic nanostructure nano materials is useful for electric field enhancement, hot electron generation and photo thermal effect. Figure 2.2 depicts the spectrum of the inbound solar radiation in $\text{Wm}^{-2}\,\text{nm}^{-1}$ versus wavelength of light.
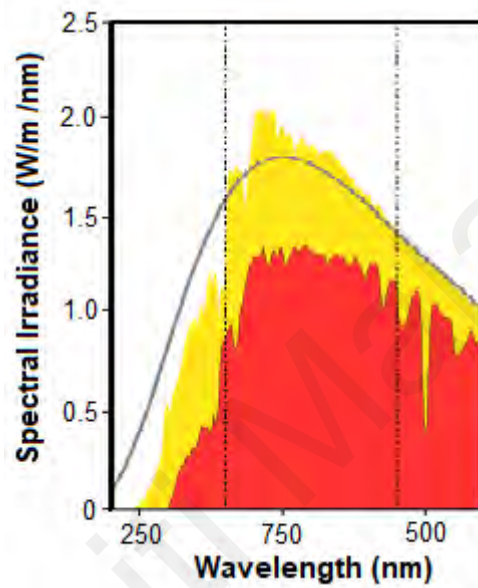
Figure 2.2: Solar irradiation power per unit area per unit wavelength versus wavelength of light that falls perpendicular to the Earth (Photo sourced from https://en.wikipedia.org/wiki/File:Solar_spectrum_en.svg).

It can be observed from Figure 2.2 that visible light between 500 to 750 nm, exhibited the highest intensity. Energy from the sun must firstly be captured by the photovoltaic cells. This photovoltaic technology is more convenient than other renewable technologies from wind turbines or generators (Schmalensee et al., 2015). In order to boost efficiency, more light has to be absorbed (particularly at longer wavelengths). These call for newer techniques like application of plasmons in DSSCs.

2.3 Photovoltaic Effect

The word "photo" in "photovoltaic", refers to photons from sunlight and "voltaic" means electricity from electron acceleration by the DSSC (Conibeer & Willoughby, 2014; Peter & Alkaisi, 2019). The solar cell converts sunlight into electricity. TiO_2 and dye are the active components of the solar cell (Green, 1992). These components constitute the photoanode. The dye absorbs light from UV to visible and to the NIR. The absorbed light will excite electrons across the band gap i.e., from the valence to conduction bands (Krč et al., 2012). Absorption by the active parts of the DSSC must be within the range of the approaching light wavelength. This will maximise the photovoltaic transformation process (Nazeeruddin et al., 1993). The dimensions of the device and its geometry are determined by the absorption characteristics of the active materials.

The DSSC consists of an organic dye that can absorb light. The inorganic dye is usually a ruthenium complex (Desilvestro et al., 1985; Sharma et al., 2018). Light absorption and electron transport are separated into two parts or constituents i.e., an inorganic dye film and an inorganic film TiO_2 semiconductor. These are the primary differences between DSSC technology and Si p−n solar cell (Sugathan et al., 2015). DSSCs with efficiency of 12.3% can be obtained from components that are less costly and easy to assemble (Yella et al., 2011). Figure 2.3 shows the wavelength of solar photons absorbed for several photovoltaic techniques. From the figure, it can be understood that many developing thin film techniques have restricted spectral response, particularly at greater than 800 nm.
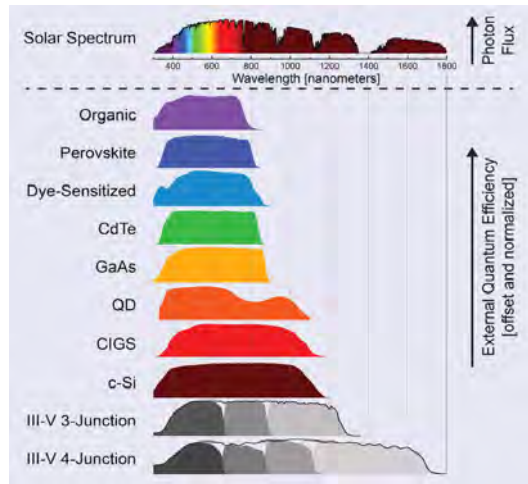
Figure 2.3: 400−1800 nm, flux of solar photons on the Earth surface and the spectra of normalised photon conversion for various kinds of solar cells modified from the research (Photo sourced from Schmalensee et al., 2015).

2.4 Dye−Sensitised Solar Cells (DSSCs)

DSSCs are the only solar cells that provide pliability and transparency. The DSSC efficiency is as good as that of amorphous silicon photovoltaic cells, but DSSCs are much cheaper. The basic structure of DSSCs includes a wide band gap n−type semiconductor. The semiconductor allows light to pass through. It is the dye sensitiser that absorbs the light. DSSCs are also referred to as Grätzel cells. Although DSSC is based on the work of O'Regan and Grätzel in 1991, the concept precedes to the 1960s and 70s. DSSCs have a porous structure. Thus, DSSCs have a much larger total interior surface area than their projected area. The semiconductors used have wide band gap. TiO_2 with band gap of about 3.2 eV or SnO_2 with band gap around 3.6 eV are good examples. The porosity of the semiconducting materials enabled a lot more organic or inorganic pigment to adhere on the walls of the semiconductors. This enables a sufficiently thin device to highly absorb visible light. In DSSCs, light absorbing organic dyes can be imbibed on the semiconductor. Alternatively, inorganic perovskite composites or QDs may be inserted within the pores of the medium in DSSCs (Rhee et al., 2013). Figure 2.3 shows the solar photon influx that reached the Earth surface for various kinds of photovoltaic cells.

The costly and energy−consuming high−vacuum manufacturing and the purification of material processes required for other thin film photovoltaic cells can be avoided by mesoscopic photovoltaic technologies (Gratzel, 2009; Sharma et al., 2018). Chlorophyll dye sensitised ZnO photoelectrode has been used since 1971 (Tributsch & Calvin, 1971). Photons were initially transformed into electricity when molecules of the excited dye injected electrons into theTiO_2, SnO_2 or other suitable wide band gap semiconductors. This led to the creation of DSSCs (O'Regan & Gratzel, 1991; Sharma et al., 2018). However, research on DSSCs only showed a significant increase in 1991, after the announcement by Grätzel and O'Regan on their innovative research work in which theTiO_2 electrode in the DSSC was sensitised with ruthenium dyes. The solar cell efficiency was over 7% (O'Regan & Gratzel, 1991).

2.5   Components in a DSSC

Figure 2.4 depicts the basic DSSC structure. In Figure 2.4, the DSSC with nano−crystalline mesoporous semiconducting material (e.g., TiO_2) photoanode has been incorporated with plasmonic nobel material, Au. A plasmonic solar cell uses plasmons to produce electricity from sunlight. However, the photovoltaic effect take place in the DSSCs application (Gwamuri et al., 2013). Plasmon improves solar cell absorbance by dispersing light with the aid of metal nanoparticles such as Au NP, Ag NP, Cu NP and Pt NP (Catchpole et al., 2008; Kunwar et al., 2019; Sharma et al., 2018; Zhang et al., 2018; Zixian et al., 2023). Inbound light with plasmon resonance wavelength, generates electron vibrations at the nanoparticles. The oscillating or vibrating electrons may then be trapped in a conducting layer of photoanode in DSSC and generate current. The amount of free negative charges or electrons present in the particle has a major impact on surface plasmon resonance. The materials used e.g., silver, platinum, gold or copper have their

SPR located in different regions of the electromagnetic spectrum. For example, in silver, the SPR is located in the UV, in platinum it is in the near UV. In gold, the SPR is in the visible and likewise in copper.
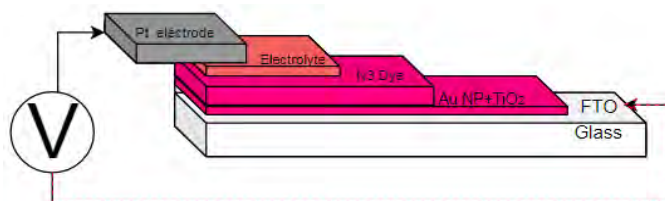
Figure 2.4: General structural of a plasmonic DSSC.

2.6   Photoanode

The nanostructured semiconductor photoanode layer is the central component of the DSSC. The photoanode of the DSSC is created by depositing the nanostructured film (e.g., TiO_2) on a transparent fluorine−doped tin oxide (FTO) or indium−doped tin oxide (ITO) glassy conductors. According to Toivola (2010), ITO and metal films have been used as flexible under layers (Toivola, 2010) on which the photoanode is deposited. The photoanode performs two functions simultaneously: (a) to support the sensitiser and (b) to serve as a channel for electrons to be transported to the external circuit. High dye loading requires a broad surface area and successful electron extraction requires a rapid charge transport. The typical semiconductor material, some of which have been stated before, include TiO_2, ZnO and SnO_2. These oxides are made into films with thickness of approximately 10 nm and about 50 $m^2\,g^{-1}$ specific surface area (Hagfeldt et al., 2010).

Au, Ag, Cu and Pt plasmonic materials can increase ability of absorbed light to enhance photocurrent density in DSSCs (Chandrasekharan & Kamat 2001; Dao et al., 2016; Dhonde et al., 2017; Dissanayake et al., 2016; Erwin et al., 2016; Gutiérrez et al., 2020; Huiyu et al., 2022; Hwang et al., 2017; Jiawei et al., 2012; Kunwar et al., 2019; Zhou et al., 2016; Shah et al., 2017; Shah et al., 2023; Zhang et al., 2018; Sharma et al.,

2018; Zixian et al., 2023) by localising the incoming photons and increasing the optical path. Different optical results can be obtained by altering the plasmonic particle size and shape, enabling the response to be tuned to the desired wavelengths (Hwang et al., 2017; Kunwar et al., 2019; Sharma et al., 2018; Zhang et al., 2018; Zixian et al., 2023).

2.7   Sensitizer

There are many types of sensitisers. These include (Hemicyanine, Merocyanine, Squarylium, and Cyanine) metal−free organic dyes (Selopal et al., 2016; Lee et al., 2017; Yousheng et al., 2005), QD sensitisers (such CdS/CdSe according to Zhang et al., 2015), perovskite−based sensitisers e.g., $CH_3NH_3PbBr_3$ and $CH_3NH_3PbI_3$ (Kojima et al., 2009; Lee et al., 2012; Rhee et al., 2013), mordant dyes (e.g., potassium dichromate ($K_2Cr_2O_7$), ferrous sulfate ($FeSO_4 \cdot 7H_2O$), copper sulfate ($CuSO_4$), stannous chloride ($SnCl_2$) and stannic chloride ($SnCl_4$) (Keith et al., 2007; Rodríguez et al., 2021) and natural dyes (e.g., anthocyanin and chlorophyll) (Smestad & Gratzel, 1998). The metal Ruthenium based dyes can be cis−bis(isothiocyanato) bis(2,2′−bipyridyl−4,4′− dicarboxylato) ruthenium (II) or N3 dye ($C_{26}H_{16}N_6O_8RuS_2$) (Nazeeruddin, et al., 1993; Nazeeruddin, et al., 1999; Peter & Alkaisi., 2019; Sharma et al., 2018), ditetrabutyl− ammonium cis bis(isothiocyanato) bis(2,2′−bipyridyl−4,4′−dicarboxylato) ruthenium(II) or N719 dye ($2C_{16}H_{36}N.2C_{12}H_7N_2O_4.C_2N_2RuS_2$) (Nazeeruddin et al., 1999) and cis−bis (isothiocyanato) (2,2′−bipyridyl−4,4′−dicarboxylato) (4,4′−di−nonyl−2′−bipyridyl) ruthenium(II) or Z907 dye ($C_{42}H_{52}N_6O_4RuS_2$) (Xie et al., 2010).

These sensitisers collect light and sends electrons into the semiconducting component. They are the light−activated part of the DSSC (Peter & Alkaisi, 2019; Sharma et al., 2018). For charge injection to be effectively imparted into the semiconductor and regenerated from the electrolyte, the sensitiser should contain chemical groups like

carboxylic groups (COOH) that binds with the TiO$_2$ semiconductor. In the structure of N3 dye, there are two bipyridine with the formula of (C$_5$H$_4$N)$_2$ and two isothiocyanate (−N=C=S) ligands. These will attach to the semiconductor surface. Due to their wide light absorption spectrum, ruthenium complex−based dyes are typically employed in DSSCs (Shalini et al., 2016).

2.8 Electrolyte

An electrolyte or ionic conductor in a DSSC is used to send electrons that have arrived at the counter electrode, e.g., platinum, back to the now positively charged dye (since the dye has been oxidised when illuminated). The electrolyte has a reducing−oxidising or redox mediator e.g., I_3^- / I^- and Br^-/Br^{-2} (Ferrere et al., 1997), SCN^-/SCN_2 (Oskam et al., 2001), and Co(II)/Co(III) according to (Nusbaumer & Moser, 2001), which is used to send electrons to the photoanode and restore the dye. The properties of the electrolyte include its ionic mobility and quick electron transfer kinetics (Peter & Alkaisi, 2019; Sharma et al., 2018; Wu & Ma, 2015). The stability and effectiveness of DSSCs depend on the following factors:

- The redox pair e.g., the iodide/triiodide pair, is extremely aggressive chemically and can destroy noble metal contacts and particles. Copper or cobalt complexes are also used as alternative redox partners. Long−term durability may be hampered by the need for adequate sealing when liquid electrolytes are used (Iftikhar et al., 2019).

- Researchers have studied ionic liquid added quasi−solid−state electrolytes or polymer gels with redox couples to prevent problems associated with vaporisation and leakage in liquid electrolytes. Liquid electrolytes are also thermodynamically

unstable at high temperatures when unprotected from solar irradiation and need to be adequately sealed (Gorlov & Kloo, 2008; Peter & Alkaisi, 2019; Sharma et al., 2018).

Electrolytes in the solid form can also provide passages for holes. The materials already studied include organic polymers (Lee et al., 2012). The use of solid electrolytes, however, raises the problem of filling the porous structure (Byrne et al., 2014). The tetrabutyl pyridine (TBP) and the TiO_2 surface interactions resulted in the quasi−Fermi level to be shifted to a higher level (Peter & Alkaisi, 2019; Sharma et al., 2018; Zhang et al., 2011). The improvement in voltage at zero current or open−circuit voltage (V_{oc}) has also been accredited to TBP−N3−TiO_2 reactions (Gao et al., 2011; Zhang et al., 2011). The efficiency of conversion from light to electricity under AM1.5 luminescence increased by 0.83% from 3.62% to 4.45% and the V_{oc} exhibited an increase from 0.615 V to 0.640 V or 4.07% increment with inclusion of TBP to the electrolyte. According to some reports (Katoh et al., 2009; Zhang et al., 2009), the addition of 4−tertbutylpyridine also improved stability of the cell. These stability gains are due to the ability of the compound to mount on the semiconductor causing the Fermi level to shift closer to the conduction band. The stability gains also prevent electron−hole recombination, thus increasing electron lifetime (Kopidakis et al., 2006). It has been emphasised that guanidinium thiocyanate (GuSCN) binds to the dye (Jean et al., 2014) rather than adhering to the TiO_2 surface (Yu et al., 2010). GuSCN can improve V_{oc} and J_{sc} (Wang et al., 2015). Adding GuSCN into the electrolyte can lead to a positive shift of the TiO_2 band−edge. GuSCN can boost the efficiency of photo electron injection and therefore the photocurrent density (Fang et al., 2019). From impedance measurements of the solar cells, authors have derived that inclusion of GuSCN in the ion conducting electrolyte can reduce interfacial recombination reaction at the TiO_2 photoanode (Dissanayake et al., 2021). The

increase in conductivity is undoubtedly the result of carrier concentration increase in the electrolyte due to dissociated free guanidinium cations (Gu^+) and thiocyanate anions (SCN^-) in the electrolyte (Dissanayake et al., 2021).

2.9   Counter Electrode

The conducting glass substrate in a DSSC, is responsible for transmitting inbound light and receiving electrons. The transference conducting oxide (TCO) is composed of tin oxide and dopants such as indium (ITO), fluorine (FTO). The two that are most frequently utilised in DSSCs are indium tin oxide (ITO) and fluorine tin oxide (FTO). FTO glass is a strong contender for electrode substrates in DSSCs since it exhibits good electrical conductivity, thermal stability and transparency even at ambient temperature. During annealing at 450°C, ITO glass showed higher sheet resistance but FTO glass remains unchanged (Sima et al., 2010). A material must minimise the state of oxidation of the charged couple before it can be used as the counter electrode (CE) in the DSSC. These materials should have low charge−transfer resistance and high exchange current density. Since 1991, platinum is used for the counter electrode in DSSCs. This is because platinum has high electrical conductance and is a good catalyst for reduction of triiodide (O'Regan & Gratzel, 1991). In DSSCs, the counter electrode receives electrons from the outer circuit. These electrons originated from the dye. The electrons induced the process of reduction of the photoanode via the I_3^- / I^- redox couple or other suitable mediators in the electrolyte. The primary requirements are high electrolyte conductivity, strong electro−catalytic performance and stability (Peter & Alkaisi, 2019; Sharma et al., 2018; Thomas et al., 2014). Carbon materials are also good as counter electrode (CE) materials. Carbon is inexpensive. It is a good conductor of electricity and a good catalyst. It is thermally stable. Carbon also exhibits high resistance to iodine corrosion and high

reactivity for triiodide reduction. These characteristics are suitable for carbon to replace the conventional and expensive Pt (Costa et al., 2014; Wu et al., 2012). Activated carbon, carbon black, graphite and graphene have all been used as CE materials (Peter & Alkaisi, 2019; Sharma et al., 2018; Wang et al., 2013). Compounds of different sulfides (Wang et al., 2009), nitrides and carbides (Wu et al., 2012) have also been used.

2.10 Operating Principle

The DSSC is divided into different functional phases. In typical wafer−based technologies, photon to electron transformation and charge movement or transfer both happen in the semiconductor. As shown in Figure 2.5, the workings of a DSSC can be explained as follows:

i.   The photons taken in through the photoanode, oxidise the dye molecules.

ii. When the dye is oxidised, the electrons released enter the outer circuit via the TiO_2 conduction band. The electrons travel to the counter electrode via the outer circuit. The electrons cannot enter the electrolyte since the electrolyte is an ion conductor.

iii. The electrolyte contains triiodide (I_3^-) ions. The electrons and triiodide ion combine to form an iodide ion at the electrolyte/counter electrode interface, according to the equation (2.1).

$$I_3^- + 2e^- \rightarrow 3I^- \tag{2.1}$$

iv. The iodide ion being negatively charged moves towards the dye in the photoanode, which is now positively charged due to its loss of electrons to the outer circuit. On releasing the electrons to the oxidised dye, the iodide ion becomes a triiodide ion again according to the equation (2.2) below:

$$3I^- \rightarrow I_3^- + 2e^- \qquad\qquad (2.2)$$

The dye is again neutral on gaining electrons released by the iodide ion and the triiodide ion goes back to the counter electrode. The process repeats (Sharma et al., 2018; Wu & Ma, 2014). The processes described above are depicted in Figure 2.5.
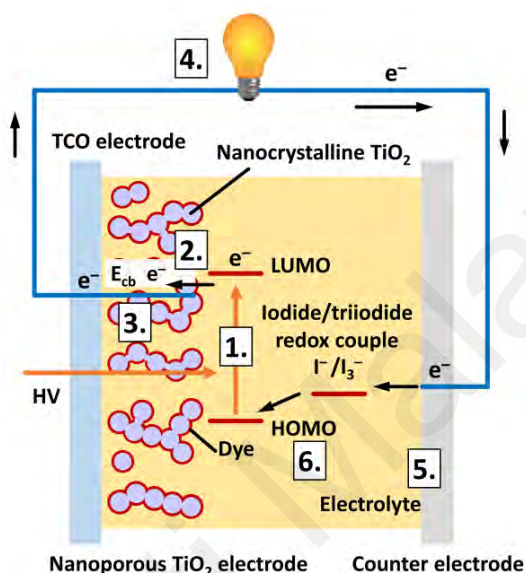
Figure 2.5: A schematic representation showing processes occurring in DSSCs when illuminated (Photo sourced from Hara & Koumura, 2009).

2.11 Plasmonic Effect

Plasmon refers to a quantum of oscillation in plasmas. A plasma is a gas in which electric charges can move freely due to gravitational or electromagnetic energies. In metals, the ground state electrons can move freely within the crystal when struck by an electromagnetic wave. However, at the surface of the metal, electron vibrations are restricted. The electron oscillations or vibrations led to transient waves or surface plasmons. However, when the surface plasmon has wavelength similar to light and is restricted to a metal surface, the phenomena is known as local surface plasmon resonance (LSPR) occurs (Louis & & Pluchery, 2012; Kunwar et al., 2019; Zhang et al., 2018; Zixian et al., 2023). Metal nanoparticles (Au NP, Ag NP, Cu NP and Pt NP) can help

solar cells absorb more light by increasing the local field and scattering light through localised surface plasmon resonance (Kunwar et al., 2019; Peedikakkandy & Bhargava., 2016; Xiayan et al., 2023; Zhang et al., 2018; Zixian et al., 2023). LSPR can be tuned in the visible wavelength. Light with visible wavelength is absorbed by most synthetic dyes. The LSPR produces two primary effects, amplification of the electric field at the surface of metallic structures and highest optical absorption at resonance frequency (Kunwar et al., 2019; Zhang et al., 2018; Zixian et al., 2023). In to avoid ambiguity, the word plasmon/plasmonic shall be used in this thesis to indicate localised surface plasmons unless otherwise specified (Ali et al., 2022; Li et al., 2023). Since the created electric field from the light pulls the electrons in the particle to one side, light incident on a metal nanoparticle causes an oscillation of free electrons in the material (Kunwar et al., 2019; Zhang et al., 2018; Zixian et al., 2023). Positive charges gather on one side, while negative charges accrue on the opposite other. Since these charges attract each other, releasing the negative charges will cause them to oscillate back and forth at a specific frequency (Ali et al., 2022; Li et al., 2023). The free electrons in the metal will undergo large vivrations if the incoming light resonates at the frequency of the free electrons. Plasmonic effects may occur in a wide range of materials with sufficient charge carrier densities. Since there is a high density of conducting electrons in the material, plasmonic effects are especially apparent in noble metals (Kunwar et al., 2019; Zhang et al., 2018; Zixian et al., 2023). The larger the electrostatic restoring force and hence the resonance frequency, the more electrons or charge carriers will be involved in the oscillation (Ali et al., 2022; Li et al., 2023). Due to the plasmonic resonances in the visible region, silver and gold have been extensively employed in the research of plasmonic phenomena (Kunwar et al., 2019; Zhang et al., 2018). Because of its negligible energy loss, silver has the strongest plasmon resonance (Kunwar et al., 2019; Zixian et al., 2023). However, since gold is highly stable chemically and physically, the metal is more frequently employed. Other materials that

exhibit plasmonic resonances can also be employed. However, noble metals are often utilised for visible and near−infrared resonances (Pelton & Bryant 2013; Kunwar et al., 2019).

2.12 Plasmonic Solar Cells

Plasmonic nanoparticles normally used to enhance the overall light absorption of PV devices in several thin film PV technologies (Ali et al., 2022; Brown, et al., 2011; Catchpole & Polman, 2008; Gangadharan et al., 2017; Li et al., 2023; Pillai & Green, 2010). Nevertheless, direct comparison of different research is difficult due to changes in the type and number of plasmonic particles utilised, as well as variances in device geometries and thicknesses. Jang et al., (2016) provide an overview of the many techniques of using plasmonic particles in solar cells (Ali et al., 2022; Jang et al., 2016; Li et al., 2023). Plasmonic particles are typically inserted into the photoanode in DSSCs to boost the optical absorption of the sensitiser or to promote charge transfer (Ali et al., 2022; Li et al., 2023; Lim et al., 2014). The quantity of particles used varies depending on the research. However, an increasing amount of plasmonic particles put into the devices exhibits a positive trend in terms of efficiency increase, levelling out at around 3 wt.% (Ali et al., 2022; Huang et al., 2015; Li et al., 2023). The boosting effects are generally ascribed to the upsurge in J_{sc}, which is caused by an increase in light absorption by the dye. Other factors can be attributed to the increase in open−circuit voltage or an inhibition of ion recombination (Ding et al., 2016; Peter & Alkaisi, 2019; Sharma et al., 2018). The differences in cell efficiency can be explained in part by the fact that the charge collecting efficiency of these devices is often not fully optimised.

Most studies have failed to consider the possibility of charge collection effects in the devices. This can markedly impact efficiency of dye sensitised solar cell. Tables 2.2, 2.3

and 2.4 list DSSC parameters with J_{sc}, V_{oc}, fill factor (*FF*) and efficiency (η) for different

DSSCs using gold nanoparticles, silver nanoparticles and copper nanoparticles.

Table 2.2: Performance parameters of DSSCs fabricated with TiO$_2$–Au NPs from literatures.

Samples	V_{oc} (V)	J_{sc} (mA cm^{-2})	*FF*	η (%)	Ref
TiO$_2$	0.70	12.6	56.0	5.0 ± 0.20	(Subas et al., 2012)
TiO$_2$–Au	0.74	13.2	61.0	6.0 ± 0.20	(Subas et al., 2012)
TiO$_2$	0.67	9.57	0.65	4.14 ± 0.02	(Teo et al., 2019)
TiO$_2$–Au	0.62	17.52	0.65	6.84 ± 0.09	(Teo et al., 2019)
TiO$_2$	0.70	14.52	0.56	5.70 ± 0.04	(Xiayan et al., 2023)
TiO$_2$–Au	0.69	17.04	0.61	7.00 ± 0.05	(Xiayan et al., 2023)

Table 2.3: Performance parameters of DSSCs fabricated with TiO$_2$–Ag NPs from the literatures.

Samples	V_{oc} (V)	J_{sc} (mA cm^{-2})	*FF*	η (%)	Ref
TiO$_2$	0.58	13.04	0.61	4.61	(Shah et al., 2017)
TiO$_2$ –Ag	0.60	15.24	0.57	5.21	(Shah et al., 2017)
TiO$_2$	0.68	9.896	0.67	4.58	(Shah et al., 2023)
TiO$_2$ –Ag	0.70	14.25	0.69	6.99	(Shah et al., 2023)
TiO$_2$	0.82	12.83	0.61	6.54	(Dao et al., 2016)
TiO$_2$ –Ag	0.82	13.49	0.67	7.49	(Dao et al., 2016)

Table 2.4: Performance parameters of DSSCs fabricated with TiO$_2$ –Cu NPs from the literatures.

Samples	V_{oc} (V)	J_{sc} (mAcm^{-2})	*FF*	η (%)	Ref
TiO$_2$	0.75	6.80	0.61	3.11	(Qureshi et al., 2020)
TiO$_2$–Cu	0.76	8.16	0.62	3.89	(Qureshi et al., 2020)
TiO$_2$	0.71	13.9	0.64	6.41	(Dhonde et al., 2017)
TiO$_2$–Cu	0.70	14.1	0.66	6.58	(Dhonde et al., 2017)
TiO$_2$	0.75	12.54	0.59	5.58	(Zhou et al., 2016)
TiO$_2$–Cu	0.73	13.11	0.64	6.12	(Zhou et al., 2016)

2.13 Summary

In this chapter, properties of plasmonic materials, plasmonic effect, photovoltaic effect, components in a DSSC, operating principles of DSSCs and the performance of plasmonic solar cells have been discussed. Development of plasmonic dye sensitised solar cells (PDSSCs) is briefly explained. The factors that could improve the photovoltaic performance of PDSSCs is also included.

Metal nanoparticles were also incorporated in the DSSCs to enhance electron transport and light harvesting. In this regard, increasing the energy−conversion efficiency by incorporating various metal nanoparticles can improve light assimilation in the active region is most likely the best approach. The technique can also be used with other kinds of photovoltaic systems.

CHAPTER 3: EXPERIMENTAL PROCEDURES

3.1   Introduction

This chapter begins with the materials used in the present study. In this chapter, compounds required to prepare the gel polymer electrolytes (GPEs), consist of phthaloyl chitosan (PhCh) and polyethylene oxide (PEO), which were mixed in the ratio of 4:1, tetrapropyl ammonium iodide (TPAI), 1−butyl−3−methylimidazolium iodide (BMII), tert−butyl pyridine (TBP) and guanidium thiocyanate (GuSCN) and iodine (I_2). In this work, the GuSCN content ranged between 0 and 5 wt.%. The structure of these materials is depicted in Table 3.1. Composition details are listed in Table 3.2. Composition with the highest conductivity will be used to prepare the gold, silver, platinum, and copper DSSCs. These are abbreviated as follows:

- i.   FTO/(TiO$_2$+Au NP)−N3 Dye/electrolyte/Pt electrode/FTO.
- ii.   FTO/(TiO$_2$+Ag NP)−N3 Dye/electrolyte/Pt electrode/FTO.
- iii.   FTO/(TiO$_2$+Pt NP)−N3 Dye/electrolyte/Pt electrode/FTO.
- iv.   FTO/(TiO$_2$+Cu NP)−N3 Dye/electrolyte/Pt electrode/FTO.

To obtain composition of the sample that exhibits highest conductivity, electrochemical impedance spectroscopy (EIS) will be employed. Plasmonic DSSCs will be characterized using the methods of intensity modulated photocurrent spectroscopy (IMPS), intensity modulated photovoltaic spectroscopy (IMVS), and photocurrent density−voltage ($J−V$).
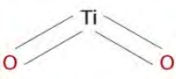
3.2   Materials

All materials used have been itemized in Table 3.1.

Table 3.1: Introduce different types of material used in this thesis and their chemical formula.

Materials	Structure	Source
Chitosan		Sigma−Aldrich
Ethylene carbonate (EC)		Merck
Propylene carbonate (PC)		Merck
Tetrapropylammonium iodide (TPAI)		Sigma−Aldrich
4−tert−butyl pyridine		Sigma−Aldrich
1−Butyl−3−methylimidazolium iodide		Sigma−Aldrich
Triton X−100 surfactant		Sigma−Aldrich
Iodine	I_2	Friendemann Schmidt
Cisbis(isothiocyanato)bis(2,2′−bipyridyl−4,4′dicarboxylato) ruthenium (II)		Sigma−Aldrich

Titanium dioxide (TiO$_2$)		Degussa Germany
Gold (Au) nanoparticles 100 nm particle size	99.9 % trace metals basis	Sigma−Aldrich
Silver (Ag) nanoparticles 100 nm particle size	99.5% trace metals basis	Sigma−Aldrich
Platinum (Pt) nanoparticle 50 nm particle size	99.9 % trace metals basis	Sigma−Aldrich
Copper (Cu) nanoparticles, 60−80 nm particle size	99.5% trace metals basis	Sigma−Aldrich

3.3   Gel Polymer Electrolyte (GPE) Preparation

Phthaloylchitosan (PhCh) was produced following the reactions between chitosan, phthalic anhydride, dimethylformamide (DMF) and N$_2$ gas. The complete reaction to produce PhCh lasted for six hours at 120°C. The PhCh product was cleaned using ethanol and vacuum dried at 60°C. Table 3.2 lists the GPEs prepared with different GuSCN compositions.

Table 3.2: GPE compositions (in wt.%).

Designation	PEO	PhCh	DMF	EC	TPAI	TBP	BMII	I$_2$
1 wt.% GuSCN	1.06	4.24	26.50	31.79	19.08	7.32	7.55	1.46
2 wt.% GuSCN	1.05	4.20	26.24	31.49	18.89	7.25	7.47	1.41
3 wt.% GuSCN	1.04	4.16	26.00	31.20	18.70	7.10	7.40	1.40
4 wt.% GuSCN	1.03	4.12	25.72	30.90	18.51	7.02	7.31	1.39
5 wt.% GuSCN	1.02	4.10	25.48	30.68	18.31	6.86	7.22	1.36

PhCh and PEO were added in the 4:1 weight ratio and solvated in DMF to create a homogeneous gel. The gel was then heated for one hour at 80°C. The gel was added with TPAI, EC, TBP, BMII and various concentrations of GuSCN to prepare the electrolytes.

The mixtures were stirred until complete homogeneity. Iodine was finally added to form the redox couple. The PhCh, PEO are ecofriendly polymers. When added with TPAI, TBP, BMII, I_2 and GuSCN can produce an ionic conducting material.

3.4 Characterization of GPEs

3.4.1 Electrochemical Impedance Spectroscopy (EIS)

Impedance measurements were carried out from 50 Hz to 1 MHz between 30°C and 100°C using the HIOKI 3532−50 LCR equipment. A sinusoidal potential of 10 mV amplitude was applied across the samples in order to detect the current. The GPEs were placed between two blocking electrodes made of stainless steel. A Nyquist plot of imaginary negative impedances to real impedance was established. The relantioship between these impedances is given by:

$$Z(\omega) = Z'(\omega) - iZ''(\omega) \tag{3.1}$$

Here $Z(\omega)$ as the complex impedance and i is $\sqrt{-1}$. From the value of $Z(\omega)$ at each frequency, the real and imaginary impedances, Z' and Z'' respectively were calculated using the equations below:

$$Z'(\omega) = |Z(\omega)| \cos\theta \tag{3.2}$$

$$-Z''(\omega) = |Z(\omega)| \sin\theta \tag{3.3}$$

$Z(\omega)$ is a complex quantity and $-Z''(\omega)$ and $Z'(\omega)$ is the imaginary and real parts of $Z(\omega)$. Angle θ represents the phase shift between the current and the voltage.

3.4.2 Ionic Conductivity Measurements

Two same size electrodes from stainless−steel were used to hold the GPEs in place. The diameter of the GPE samples was 2 cm. The impedance of the GPEs was measured between 308 K and 363 K using the HIOKI instrument from 50 Hz to 5 MHz frequencies. Equation (3.4) was used to calculate the ionic conductivity (σ).

$$\sigma = \frac{t}{R_b A} \qquad (3.4)$$

Here, t and A are the thickness and contact area of the electrolyte samples, respectively. R_b is bulk resistance of the electrolyte. R_b is the value at the intersection between the impedance plot and the Z' axis.

3.5 Fabrication of DSSC

There are three components that need to be prepared for the DSSC assembly: the working electrode, counter electrode and electrolyte.

3.5.1 Preparation of TiO$_2$−X (X = Au, Ag, Cu and Pt) Photoanodes

The photoanode was prepared on fluorine doped tin oxide (FTO) coated glass. The photoanode or working electrode layer was prepared by depositing a P90 ($\sim$30 nm) TiO$_2$ followed by a porous layer of P25($\sim$50 nm) TiO$_2$. P90 has an almost twofold greater specific surface area (90−110 m^{2}g^{-1}) than P25 (50−70 m^{2}g^{-1}). The P90 TiO$_2$ sample had an average particle size of 30 nm. It is smaller than the P25 TiO$_2$ sample (50 nm). The anatase phase content of the P90 sample is greater (91−92%) than that of the P25 TiO$_2$ (87−88%). A mortar and pestle were used to grind 0.5 g P90 TiO$_2$ powder for half an hour

in 2 ml nitric acid (HNO_3) of 0.1 M concentration. A portion of the FTO glass was covered with adhesive tape to avoid depositing P90 TiO_2 on the region required for electrical connections during the spin−coating. The prepared P90 TiO_2 paste was spun for 60 seconds at 2350 rpm on the FTO glass before sintering at 450°C for a half hour. The second TiO_2 coating consisted of 0.5 g P25 TiO_2 powder, 0.1 g carbowax and one drop surfactant (Triton X−100) and the different amounts of each nanoparticle. There will be four types of P25 TiO_2 containing films each having different types of nanoparticles. Six different weight ratios of the Au, Ag, Cu and Pt nanoparticles were mixed with the same amount of P25 TiO_2 paste to prepare the photoanodes. Hence, the paste contained the P25 TiO_2 powder (0.5 g), 2 mL of 0.1 mM HNO_3, 0.1 g carbowax and one drop surfactant (Triton X−100) together with all the four types of nanoparticles. These were ground to produce a homogenous mixture. By the doctor blade method, the P25 TiO_2 and added nanoparticle was applied on the compact layer (P90 TiO_2). The electrode was again heated at 450°C for 30 minutes. The different weight percentages of the nanoparticles used are shown in Table 3.3.

Table 3.3: Composition of nanoparticles. Here X represents the type of nanoparticle.

Designation	Weight percentage (%)	NP (g)
X0	0 wt.%	0
X1	1 wt.%	0.005
X2	2 wt.%	0.010
X3	3 wt.%	0.015
X4	4 wt.%	0.020
X5	5 wt.%	0.025

Before assembling the DSSCs, the TiO_2/X NP photoanodes were sensitized by immersing the photoanodes in 10 ml ethanol solution of ruthenium N3 dye for 24 hours in the dark at room temperature.

3.5.2 Pt−Counter Electrode

Plastisol solution (Pt in solution form) was drop cast on a clean FTO glass. The FTO glass was air−dried in order to prepare the Pt−counter electrode. After coating Pt on the FTO glass, the electrode was sintered at 450°C for 30 minutes before assembling the DSSCs.

3.5.3 Fabrication of Plasmonic DSSCs

TiO_2 working electrode, PhCh−based GPE with the highest conductivity, Pt−counter electrode, and four different kinds of nanoparticles were used to assemble the DSSCs as described below:

i.   FTO/(TiO_2+Au NP)−N3 Dye/electrolyte/Pt electrode/FTO.

ii. FTO/(TiO_2+Ag NP)−N3 Dye/electrolyte/Pt electrode/FTO.

iii. FTO/(TiO_2+ Cu NP)−N3 Dye/electrolyte/Pt electrode/FTO.

iv. FTO/(TiO_2+ Pt NP)−N3 Dye/electrolyte/Pt electrode/FTO.

Figures 3.1, 3.2, 3.3, and 3.4 show the DSSCs configuration with Au, Ag, Cu, and Pt NPs in the photoanode, respectively.
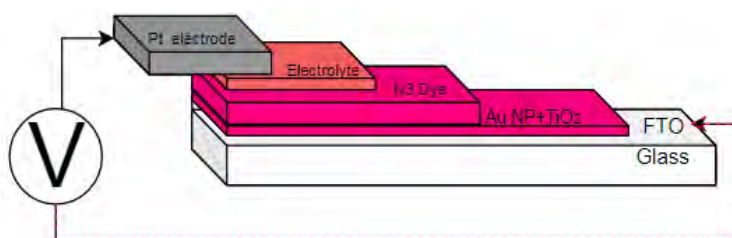
Figure 3.1: DSSCs with Au nanoparticles in the photoanode.
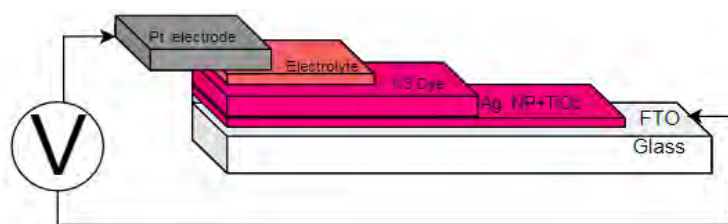
Figure 3.2: DSSCs with Ag nanoparticles in the photoanode.
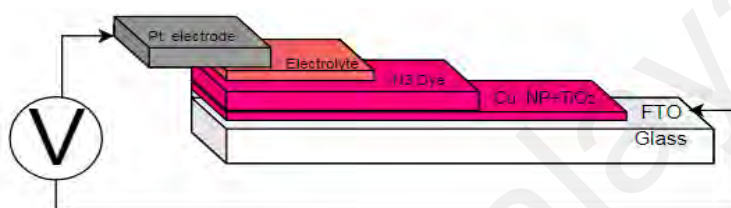
Figure 3.3: DSSCs with Cu nanoparticles in the photoanode.
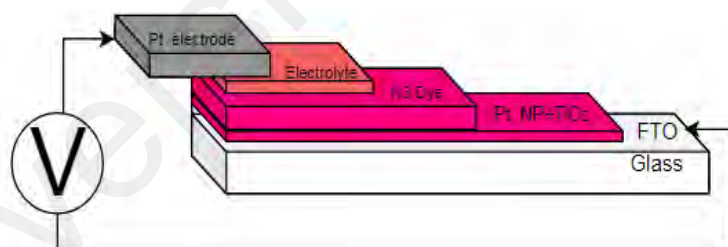
Figure 3.4: DSSCs with Pt nanoparticles in the photoanode.

The GPE was sandwiched between the Pt−counter electrode and the dye−sensitized TiO$_2$ layer to form the DSSC. An Oriel LCS−100 solar simulator instrument was used to determine the DSSC performance under 1 Sun intensity. The DSSCs had an active area of 0.2 cm^2. Figure 3.5 explains how the DSSCs were assembled.
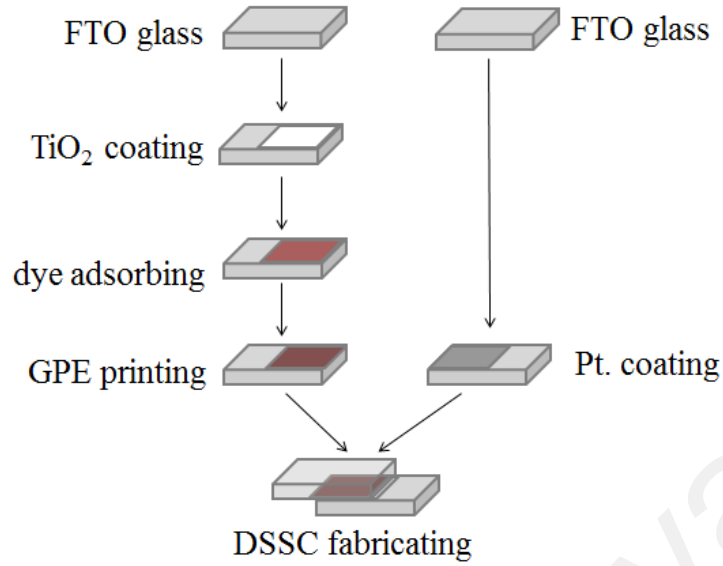
Figure 3.5: DSSC components preparation.

3.6   DSSC Characterization

Different methodologies were used to carry out DSSC characterization. The DSSCs were characterized by determining the current density, intensity modulated photovoltage spectroscopy (IMVS) and intensity modulated photocurrent spectroscopy (IMPS).

3.6.1   *J−V* Measurements

J−V characterization was carried out at one sun. This is equivalent to the solar spectrum intensity of 100 mW cm^{-2}. The DSSCs were scanned from zero current (short−circuit state) to open−circuit condition. From the *J−V* graphs the following parameters can be estimated:

i.   Open−circuit voltage $\left(V_{oc}\right)$: $V_{oc} = V\left(I = 0\right)$ $\qquad\qquad$ (3.5)

ii.   Short−circuit current $\left(J_{sc}\right)$: $J_{sc} = J\left(V = 0\right)$ $\qquad\qquad$ (3.6)

iii.   Fill factor (*FF*): $FF = \dfrac{J_{max} \times V_{max}}{J_{sc} \times V_{oc}}$ (3.7)

Here J_{max} is the maximum current density and V_{max} is the maximum voltage. The open−circuit voltage is designated as V_{oc} and J_{sc} is the short−circuit current density. The power conversion efficiency, (η), was calculated using equation (3.8) as follows:

$$\eta\left(\%\right) = \frac{V_{oc} \times J_{sc} \times FF}{P_{in}} \times 100\%$$ (3.8)

The incident light power density in the above equation is represented by P_{in}.
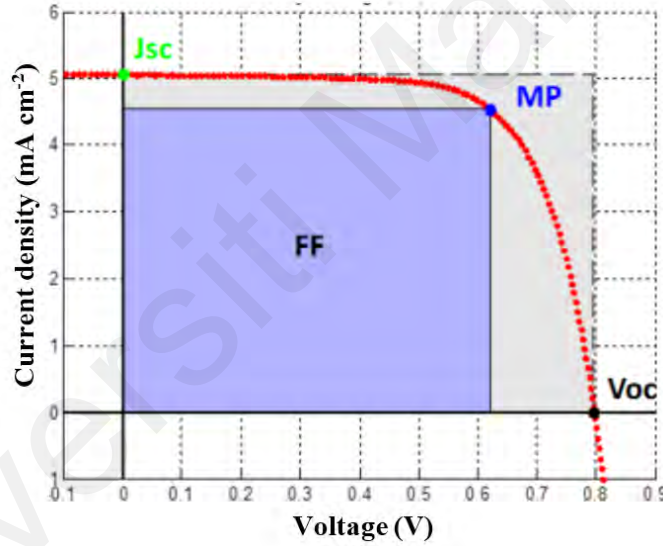
Figure 3.6: Example of a *J−V* curve for a DSSC.

In Figure 3.6, J_{sc} (*y*−axis) is short−circuit current density, V_{oc} (*x*−axis) is open−circuit voltage, *FF* is fill factor and MP is maximum power density. The *J−V* curve is ideally rectangular in shape. The ideal fill factor is one or 100% since the maximum power is V_{oc} multiplied by J_{sc}. However, non−ideal circumstances due to parasitic solar cell effects lowered the maximum power density and caused the *J−V* curve to deviate from the ideal

case. The $J-V$ curve actual area, which measures the maximum power (blue rectangle), becomes smaller.

3.6.2 Intensity Modulated Photocurrent Spectroscopy (IMPS) and Intensity Modulated Photovoltage Spectroscopy (IMVS) Experimental Methods

Instead of adjusting the amplitude of the current or potential signal, IMPS modifies the intensity of the light beam aimed at the DSSC. Fundamentally, the IMPS and IMVS work in the same way. Both methods are shown in Figure 3.7.
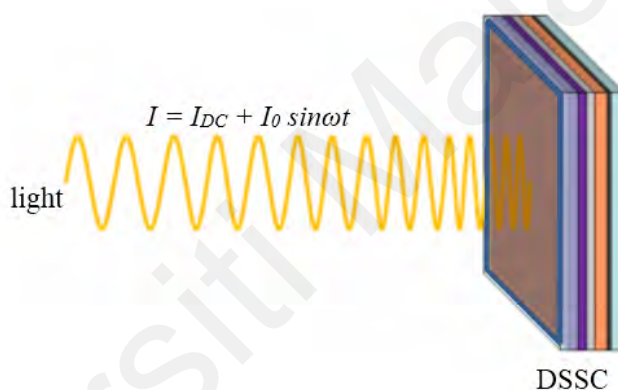
Figure 3.7: IMPS and IMVS setup.

A laser beam with a base intensity current I_{DC} is aimed towards the DSSC during IMPS and IMVS studies. On top of the constant base intensity current, I_{DC} has overlaid a sinusoidal waveform with amplitude I_o. Throughout the experiment, the frequency (*f*) is varied. The angular frequency (ω) formula can be written as $\omega = 2\pi f$. The DSSC's photovoltage (IMVS) or photocurrent (IMPS) will be monitored appropriately. The frequency of the applied signal is similar to the light signal that results but of a different phase. By altering the frequency of the light signal, time−dependent data on various processes, such as diffusion coefficients or reaction rates, may be collected.

The IMPS and IMVS can be obtained from the $J-V$ charecteristics shown in Figure 3.8. When the DSSC power output rose with increasing light intensity, the photocurrent increased, resulting in a higher short−circuit current I_{sc} at 0 V. The open−circuit potential V_{oc} also increased. Continuous illumination is often provided while varying the current or potential signal amplitude during the photovoltaic characterization of DSSCs. However, in IMVS and IMPS studies, the intensity of a laser beam aimed at a DSSC is modulated, allowing $J-V$ curve of the cell to be measured. The IMVS and IMPS section are highlighted in green and red ellipses, respectively, in Figure 3.8.
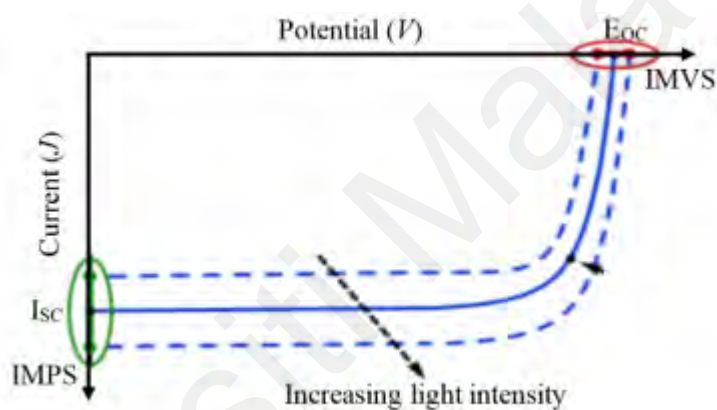
Figure 3.8: $J-V$ of a DSSC shows the regions covered by IMVS and IMPS.

During the IMVS and IMPS experiments, a red−light emitting diode (LED) was used. The red−light wavelength is 627 nm. The intensity of the red light was 0.09 mW. Measurements were carried out between 10 kHz and 10 MHz. During IMPS experiment, the DSSC was potentiostatically set to short−circuit condition, i.e., at 0 V. Under this condition was the photocurrent measured. The largest band gap between the valence and conduction bands of the semiconductor occurs under short−circuit state, which almost eliminates electron injection into the TiO_2 conduction band. The majority of reactions took place at the back layer of the anode. Electrons move from the original site to the

back layer of the electrode. The highest point on the Nyquist plot of Figure 3.9 was used to determine the characteristic frequency, f_{IMPS}.
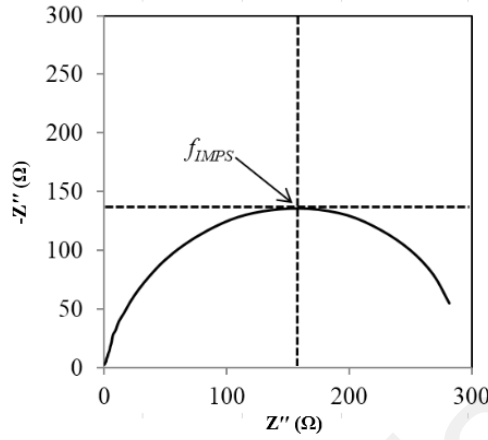
Figure. 3.9: The Nyquist plot and f_{IMPS}.

The relevant electron transport time, τ_{tr} can be derived from the IMPS result using the following equation:

$$\tau_{tr} = \frac{1}{2\pi f_{IMPS}} \tag{3.9}$$

f_{IMPS} is the DSSCs' characteristic frequency as determined by the Nyquist plot.

3.6.3 IMVS Experiment

Open−circuit or zero current density conditions have been used for IMVS experiments. At an open−circuit, the voltage exhibited by the DSSC is maximum. The highest potential of a DSSC before power is lost as opposed to being produced is known as the open−circuit potential. Under this situation, the gap between the valence and the conduction bands or the energy gap is reduced. Therefore, it is less probable that there will be reactions at the back layer of the anode. The CB of the semiconductor receives the majority of the

produced photoelectrons. Additionally, at open−circuit potential, the DSSC approaches a steady state. This suggests that the recombination rate of electrons and the electron injection rate into the CB are equivalent. The highest point on the Nyquist plot in Figure 3.10 is the characteristic frequency, f_{IMVS}.
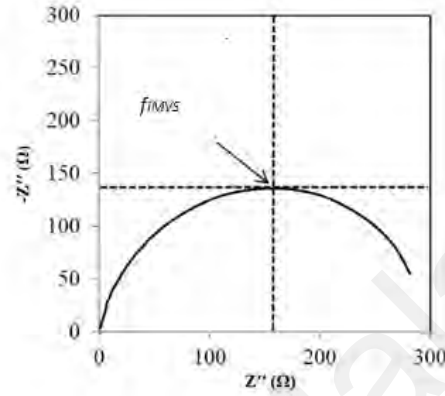
Figure 3.10: The Nyquist plot and f_{IMVS}.

Equation (3.10) can be applied to calculate the rate of electron recombination, τ_{rec} of an electron based on results from IMVS.

$$\tau_{rec} = \frac{1}{2\pi f_{IMVS}}$$

(3.10)

Here f_{IMVS} is the characteristic frequency connected to the IMVS for the DSSCs Nyquist plot.

3.6.4   Charge Collection Efficiency (η_{cc})

The charge collection efficiency η_{cc} may be calculated using time constants τ_{tr} and τ_{rec} (equation (3.11)). This is a crucial aspect in determining the overall DSSC performance. Good cells have a high charge collection efficiency. Increase the duration

for electron recombination or decrease the time for electron travel to attain high charge−collecting efficiency.

$$\eta_{cc} = 1 - \frac{\tau_{tr}}{\tau_{rec}}$$

(3.11)

3.7   Summary

This chapter discussed electrolyte preparation, DSSC fabrication, and their characterizations. Measurements of electrolyte impedance were explained. The method of developing the working electrode was also clarified. The findings and discussion will be presented in the following chapters.

CHAPTER 4: CHARACTERISTICS GEL POLYMER ELECTROLYTES AND GOLD NANOPARTICLES ADDED TiO₂ DYE SENSITIZED SOLAR CELLS [TiO₂(P90) + TiO₂(P25) + *x* Au NP)–N3 dye/GPE/Pt]

4.1 Introduction

The third generation DSSC functions via some crucial steps. These include light absorption, electron injection by the dye, transportation of electrons to the outer circuit through the TiO₂ in the photoanode, collection of electrons at the counter electrode, and the return of the electrons to the photoanode via the redox mediators in the electrolyte. All gel polymer electrolytes conductivities were carried out using electrochemical impedance spectroscopy (EIS) and highest conductive gel polymers sample was used in the DSSCs. DSSC characterizations include the photovoltaic effect, where the photovoltaic cells were measured on exposure to euivalent intensity of sunlight.

FF and η of the photovoltaic cell were also determined. IMVS and IMPS measurements were also determined. From IMPS/IMVS measurements, electron recombination time, charge transfer time, and charge collection efficiency can also be determined. For this purpose, many DSSCs were produced to investigate cell performance. The configuration of [FTO/TiO₂(P90+P25)/AuNP)–N3 dye/GPE/Pt/FTO] was used to assemble solar cells. This chapter investigated and evaluated the effect of TiO₂–Au nanoparticle photoanode on the characteristics of the fabricated DSSCs.

The bio–polymer, phthaloylchitosan based electrolytes (GPEs) of PhCh:PEO:EC:TPAI:TBP:BMII:GuSCN:I₂ have been investigated on electrochemical characteristics. This chapter are discussed about conductivity at room temparature of all prepared gel polymer electrolyte use in this work. The gel was added with TPAI, EC, TBP, BMII and various concentrations of GuSCN to prepare the electrolytes.

4.2 Ionic Conductivity Measurements by EIS

The EIS results can be obtained in the form of Nyquist plots for the PhCh:PEO:EC:TPAI:TBP:BMII:GuSCN:I_2 GPEs containing different wt.% of GuSCN (1 wt.%, 2 wt.%, 3 wt.%, 4 wt.% and 5 wt.%) at room temperature are shown in Figure 4.1, the bulk resistance, R_b was estimated and used to determine ionic conductivity (σ) of the GPEs. The values of R_b and σ for the GPEs are listed in Table 4.1. R_b decreased with the rise in GuSCN percentage and the lowest value of 9.88 Ω is at 3 wt.% GuSCN. Accordingly, σ increased with GuSCN concentrations and reached the highest value of 12.69 mS cm^{-1} at 3 wt.% of GuSCN. After 3 wt.% GuSCN concentration, conductivity declined. Figure 4.1 shows the Nyquist plots for the GPEs containing 1 wt.%, 2 wt.%, 3 wt.%, 4 wt.% and 5 wt.% GuSCN content. Figure 4.2 shows the room temperature conductivity of GPE with various GuSCN content.
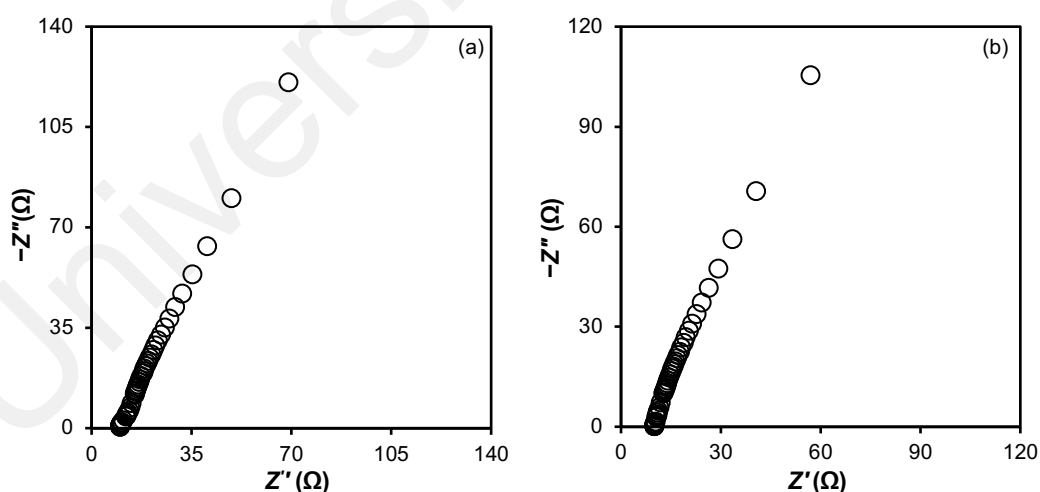
Figure 4.1, continued…
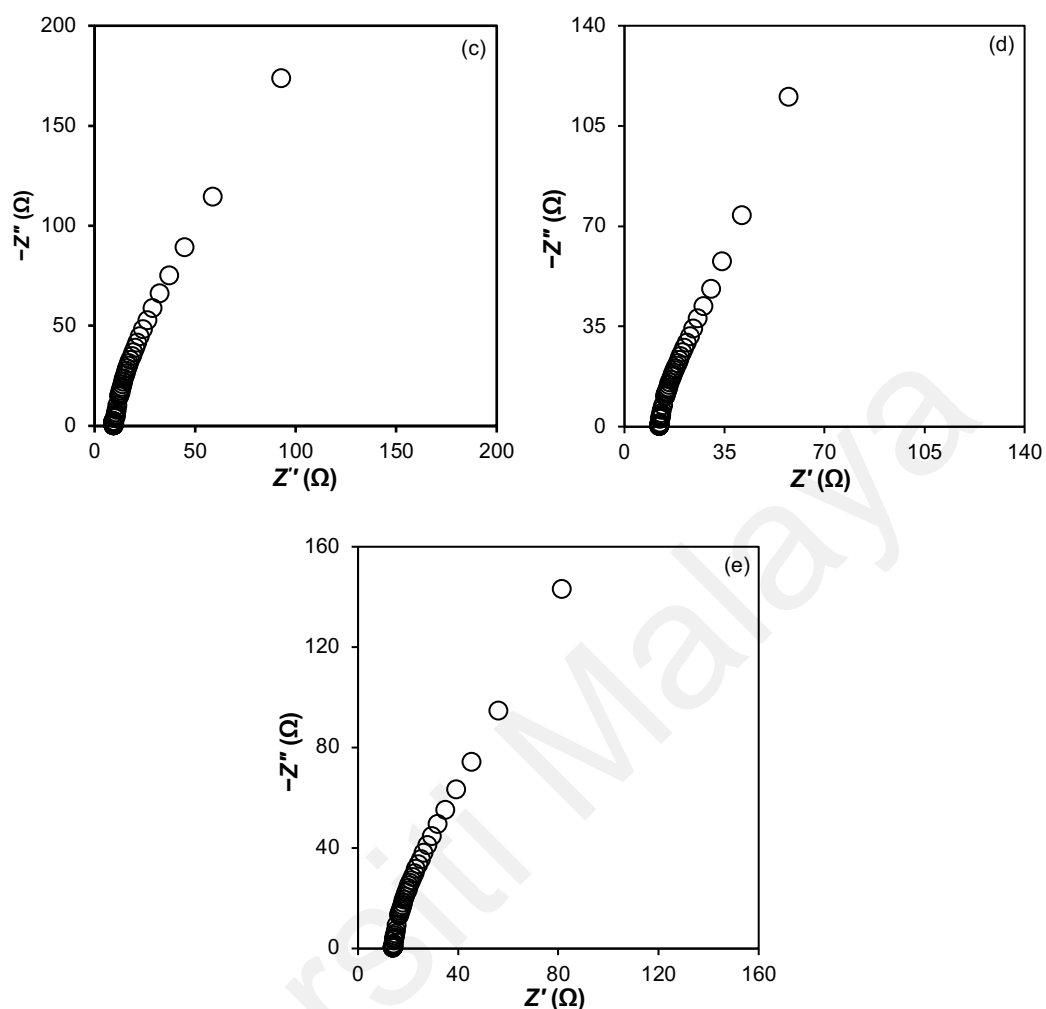
Figure 4.1: Nyquist plots for PhCh:PEO:EC:TPAI:TBP:BMII:GuSCN:I$_2$ GPEs with (a) 1 wt.%, (b) 2 wt.%, (c) 3 wt.%, (d) 4 wt.% and (e) 5 wt.% GuSCN content.

Table 4.1: Room temperature ionic conductivity and bulk resistance for GPEs with various GuSCN content.

GuSCN content (wt.%)	Conductivity, σ (mS cm^{-1})	Bulk resistance, R_b (Ω)
1	11.35	11.50
2	12.49	10.10
3	12.69	9.88
4	11.29	12.29
5	10.56	14.18
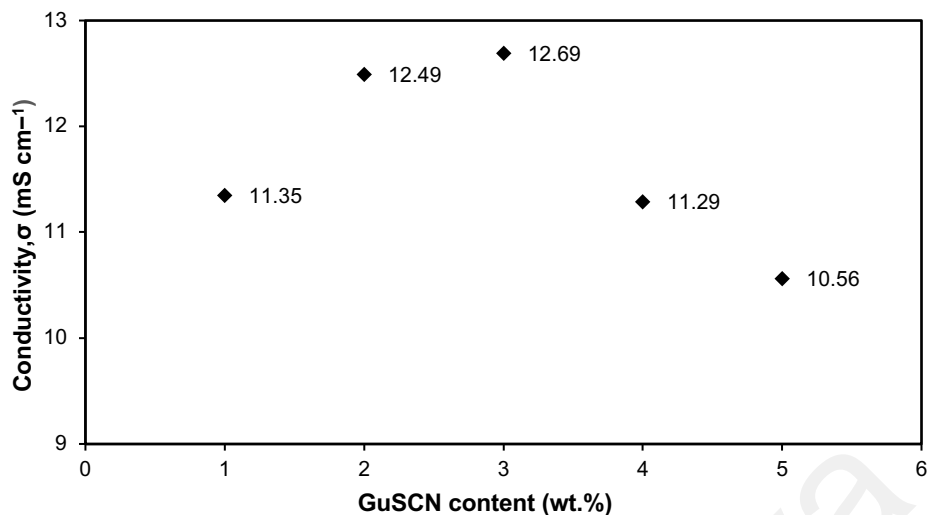
Figure 4.2: Conductivity at room temperature of PhCh:PEO:EC:TPAI:TBP: BMII:GuSCN:I₂ GPEs with various GuSCN content.

Guanidinium thiocyanate (GuSCN) was introduced to the gel polymer electrolytes PhCh−PEO−EC−TPAI−BMII−TBP−I$_2$. Earlier research (Zhang et al., 2009) shown that GuSCN altered electron injection yield by altering the TiO$_2$ flat band potential. This will result in an increase in J_{sc} and efficiency of DSSCs (Wang et al., 2015; Zhang et al., 2009). Table 4.1 lists GuSCN concentration and ionic conductivity of PhCh−PEO based GPEs at room temperature. The ionic conductivity achieved after adding 1 wt.% GuSCN to the GPE system was 11.35×10^{-3} S cm^{-1}. A further increase can be seen when additional GuSCN is added, contributing to a high numerical density of free charges. The GPE with 3 wt.% GuSCN had the highest ionic conductivity, with a value of 12.69×10^{-3} S cm^{-1}. Ionic conductivity began to decline after this concentration. This might be related to the production of neutral ion pairs resulting in a lower free ion concentration that do not contribute to conductivity. As a result, DSSCs were created in this study employing the optimised GPE with a GuSCN concentration of 3 wt.%.

4.3 Photovoltaic Measurements (*J*−*V*)

The photovoltaic (*J*–*V*) measurements of the [TiO$_2$(P90) + TiO$_2$(P25) + *x* AuNP)–N3 dye/GPE/Pt] based DSSCs were studied. In the DSSCs, *x* takes the values as follows: (*x* = 0 wt.%, 1 wt.%, 2 wt.%, 3 wt.%, 4 wt.% and 5 wt.%). The photovoltaic characteristics (*J*–*V*) of these cells have been presented in Figure 4.3. Table 4.2 displays the values of V_{oc}, J_{sc}, fill factor (*FF*) and efficiency (*η*) of the DSSCs.
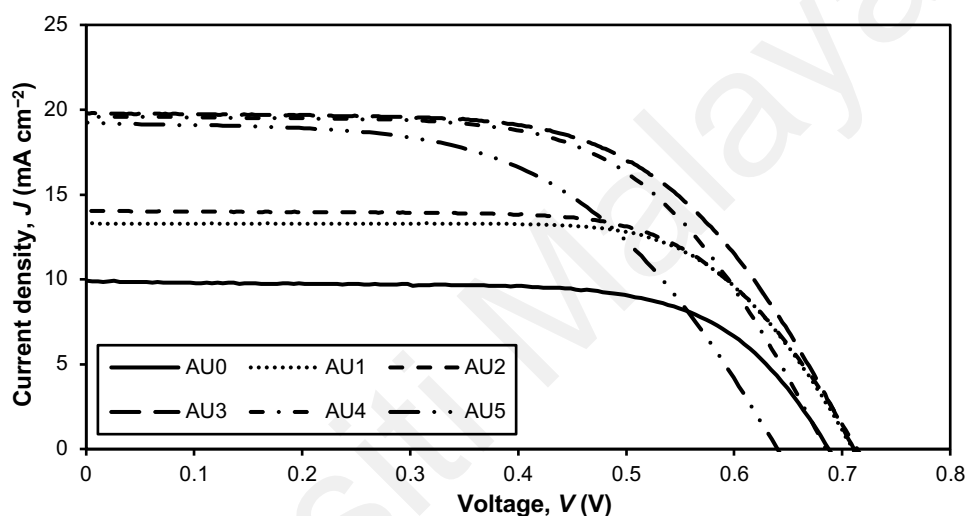
Figure 4.3: *J*–*V* plots for DSSCs with different TiO$_2$/Au photoanode.

Table 4.2: Values of J_{sc}, V_{oc}, *FF*, and *η* obtained from Figure 4.3.

Designation	Au NP (g)	J_{sc} (mA cm^{-2})	V_{oc} (V)	FF (%)	η (%)
AU0 (0 wt.%)	0	9.90 ± 0.03	0.68 ± 0.01	67.41 ± 0.34	4.59 ± 0.01
AU1 (1 wt.%)	0.005	12.81 ± 1.02	0.70 ± 0.01	68.32 ± 1.08	6.20 ± 0.42
AU2 (2wt.%)	0.010	14.04 ± 0.04	0.71 ± 0.01	66.00 ± 0.01	6.62 ± 0.01
AU3 (3 wt.%)	0.015	19.82 ± 0.11	0.72 ± 0.01	60.10 ± 0.38	8.54 ± 0.01
AU4 (4 wt.%)	0.020	19.60 ± 0.39	0.68 ± 0.01	60.32 ± 1.56	8.08 ± 0.19
AU5 (5 wt.%)	0.025	19.34 ± 0.22	0.65 ± 0.01	54.19 ± 0.9	6.78 ± 0.06

Figures 4.4 to 4.7 show the variation of V_{oc}, J_{sc}, fill factor (*FF*), and efficiency (*η*) versus Au NPs content in grams for the solar cells fabricated.
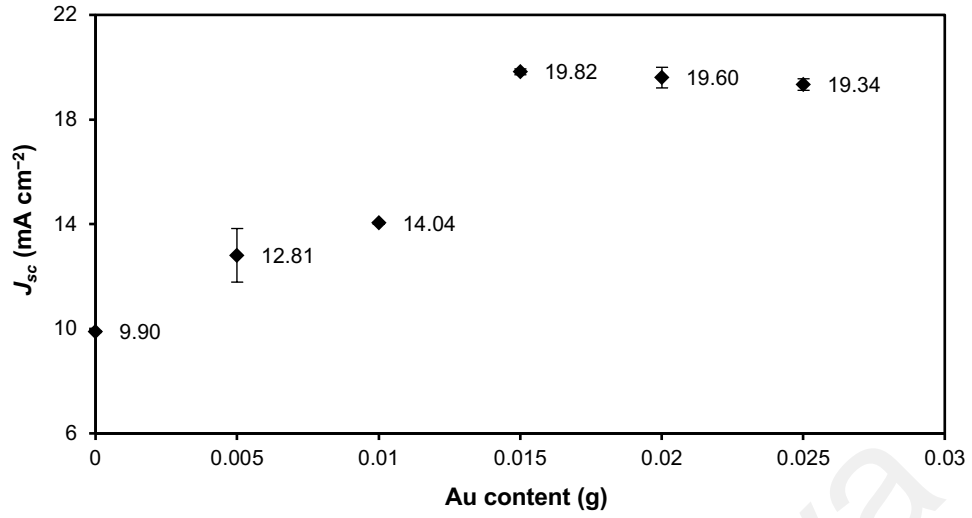
Figure 4.4: Short−circuit current density, J_{sc} for DSSC with TiO₂/Au photoanode.

Following the variation of nanoparticle contents, J_{sc} and efficiency (η) of DSSC increase with increasing gold nanoparticle concentration since the DSSC exhibited maximum J_{sc} (19.82±0.11) mA cm^{-2} and η (8.54±0.01) % for the 3 wt.% gold nanoparticle concentration and then decreased with further addition of Au NPs. The open−circuit voltage, V_{oc} reached the maximum value of (0.72±0.01) V at 3 wt.% Au concentration.
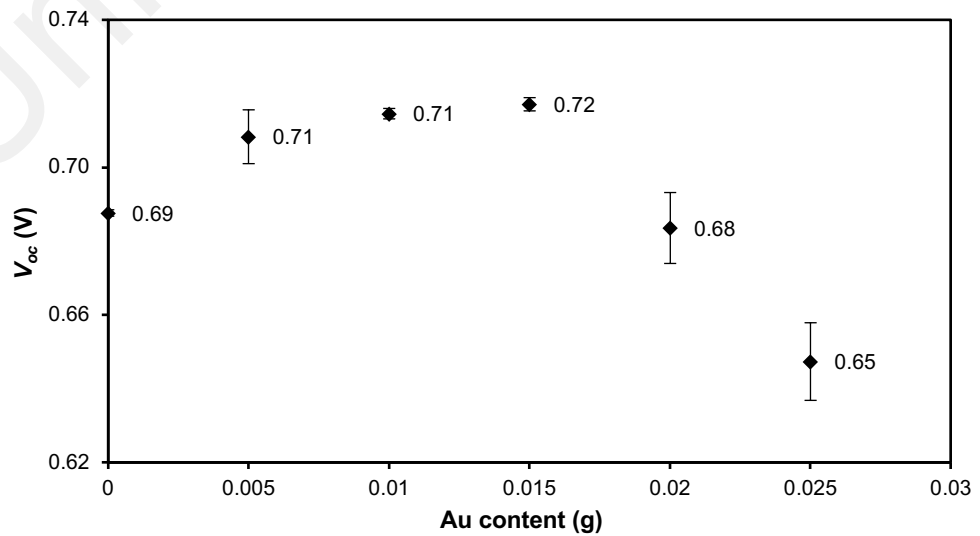
Figure 4.5: Open−circuit voltage, V_{oc} for DSSC with different TiO₂/Au photoanode.
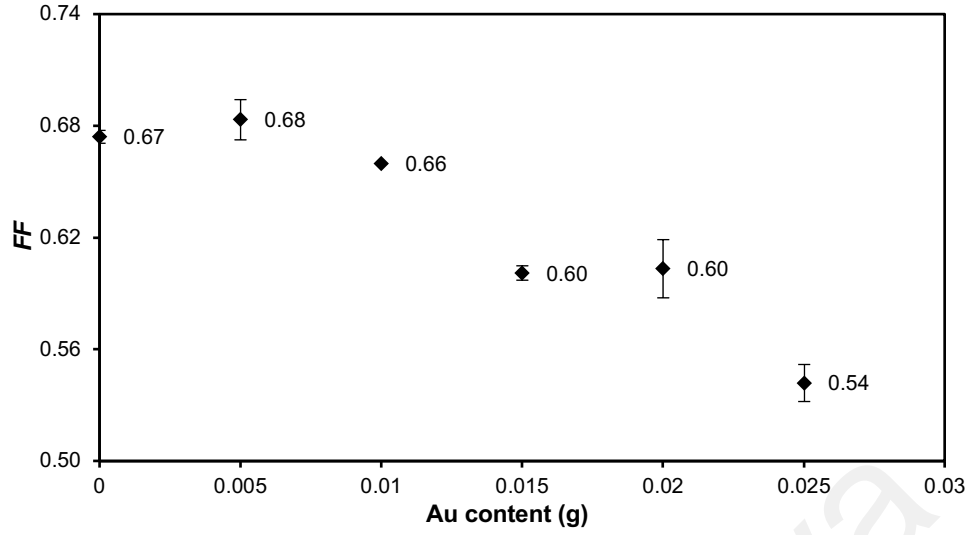
Figure 4.6: Fill factor, *FF* for DSSC with TiO₂/Au photoanode.

The DSSC without Au NP exhibited the lowest J_{sc} of (9.90±0.03) mAcm⁻² and the lowest η of (4.59±0.01) %. Increasing Au NP content from 1 wt.% to 3 wt.%, the J_{sc}, V_{oc}, and η also increased following the trend of (12.81±1.02) mA cm⁻², (0.71±0.01) V, and (6.20±0.42) % to (14.04±0.04) mA cm⁻², (0.71±0.01) V, (6.62±0.01) % and to (19.82±0.11) mA cm⁻² and (0.72±0.01) V, and (8.54±0.01) %, respectively. From 4 wt.% to 5 wt.%, the J_{sc}, V_{oc}, and η also decreased following the trend of (19.60±0.39) mA cm⁻², (0.68±0.01) V, and (8.08±0.19) % to (19.34±0.22) mA cm⁻², (0.65±0.01) V, and (6.78±0.06) %, respectively.
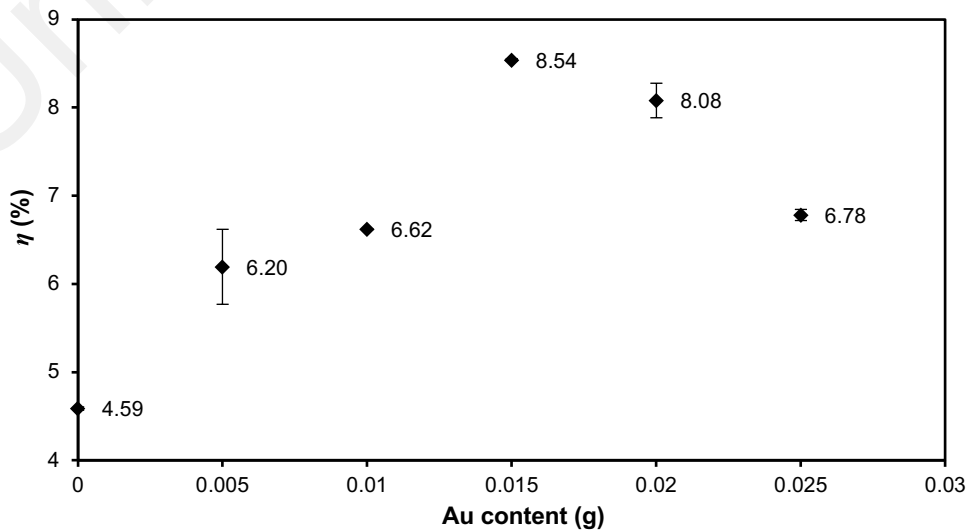
Figure 4.7: Power conversion efficiency (*η*) for DSSC with TiO₂/Au photoanode.

4.4 IMVS/IMPS

Figure 4.8 is the variation of τ_{rec} for DSSCs with different Au content in the TiO$_2$/Au photoanode. The frequencies f_{IMVS} were obtained from the maxima of the Nyquist−type semicircles from IMVS experiment. The frequencies f_{IMPS} were obtained from the maxima of the Nyquist−type semicircles from IMPS experiment. The f_{IMVS} is associated with electron recombination time τ_{rec}. The τ_{rec}, τ_{tr} and charge collection efficiency η_{cc} were calculated from corresponding characteristic frequencies using the equations (3.10), (3.9) and (3.11) of Chapter 3, respectively.

IMPS curves as Nyquist−type plots posed a maximum at intermediate frequencies, f_{IMPS} which is the characteristic parameter for the transportation of electron through the TiO$_2$ pores to the back layer. This value gives the electron transport time, τ_{tr} in the DSSC and it happened in the order of a few milliseconds through the mesoporous TiO$_2$.

The IMVS and IMPS experiments have been performed at 0.09 mW intensity of red LED light (627 nm). From the IMVS experiment, recombination time, τ_{rec} graph has been depicted in Figure 4.8 and from the IMPS experiment electron transport time, τ_{tr} graph have been depicted in Figure 4.9. All the values have been tabulated in Table 4.3. It can be observed that the DSSC containing 3 wt.% Au nanoparticles in the photoanode exhibited the lowest τ_{tr} value (7.32±0.63) ms, highest τ_{rec} value (115.33±4.16) ms and highest charge collection efficiency, η_{cc} of 0.94. If $\tau_{tr} < \tau_{rec}$, the photo−excited electron is transported in TiO$_2$ within a very short time rather and will not undergo for recombination. Due to the higher recombination time of elctrons to holes, it is possible to move longer time of elctrons transport in TiO$_2$ rather than its origine of oxidized dye to combine. The charge collection efficiencies, $\eta_{cc} = 1 - \left(\tau_{tr} / \tau_{rec} \right)$ for 0 wt.%, 1 wt.%,

2 wt.%, 3 wt.%, 4 wt.% and 5 wt.% Au nanoparticles photoanode based DSSC are 0.53, 0.74, 0.79, 0.94, 0.85 and 0.69, respectively. Figures 4.8 and 4.9 show the relationship among τ_{rec} and τ_{tr} versus Au content in grams for the solar cells fabricated. Figure 4.10 exhibits the charge collection efficiency, η_{cc} for DSSC with varying Au content in the TiO$_2$/Au photoanode.
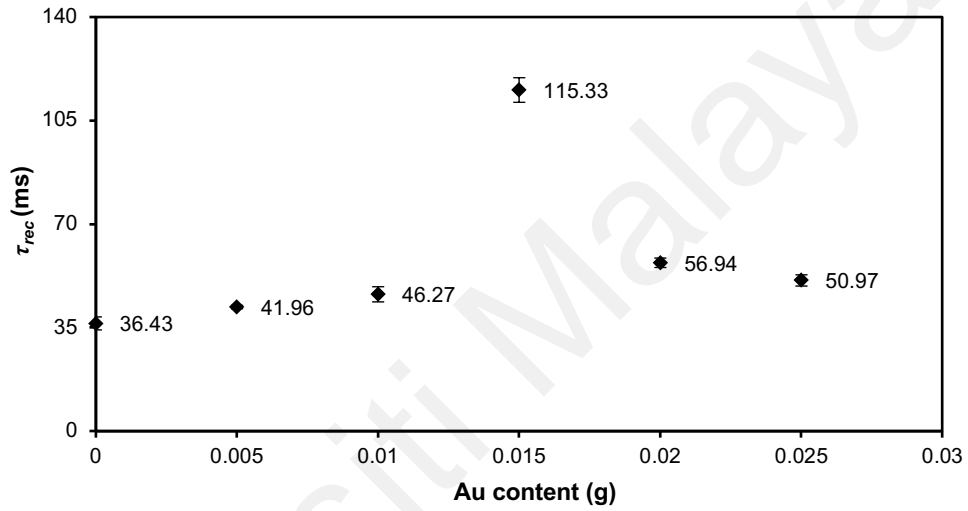
Figure 4.8. Recombination time, τ_{rec} for DSSC with TiO$_2$/Au photoanode.
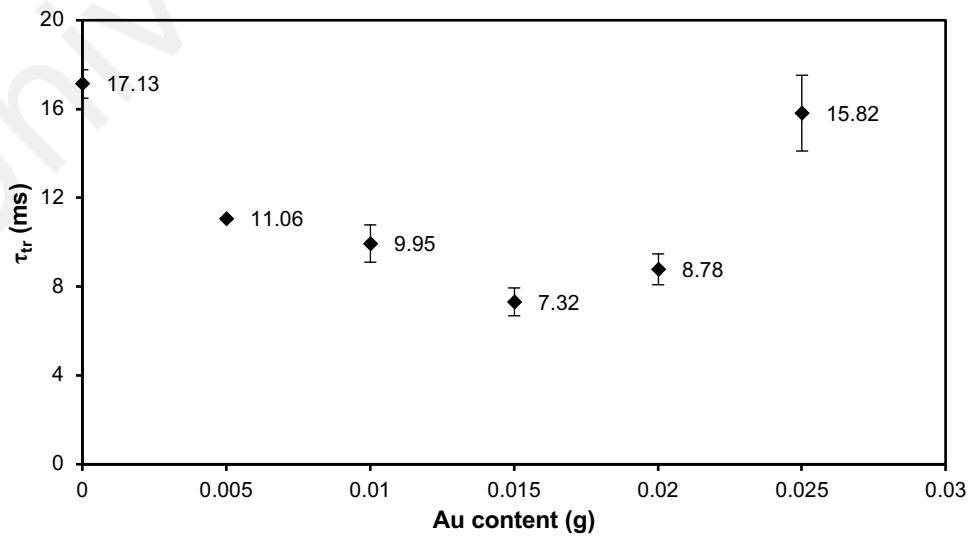
Figure 4.9: Electron transport time, τ_{tr} for DSSC with TiO$_2$/Au photoanode.

Table 4.3: Values of τ_{rec}, τ_{tr}, and η_{cc} obtained from IMVS/IMPS.

Designation	Au (g)	τ_{rec} (ms)	τ_{tr} (ms)	η_{cc} (%)
AU0 (0 wt.%)	0	36.43 ± 2.19	17.13 ± 0.64	0.53 ± 0.03
AU1 (1 wt.%)	0.005	41.96 ± 0.59	11.06 ± 0.04	0.74 ± 0.01
AU2 (2 wt.%)	0.01	46.27 ± 2.57	9.95 ± 0.84	0.79 ± 0.01
AU3 (3 wt.%)	0.015	115.33 ± 4.16	7.32 ± 0.63	0.94 ± 0.01
AU4 (4 wt.%)	0.02	56.94 ± 1.60	8.78 ± 0.70	0.85 ± 0.01
AU5 (5 wt.%)	0.025	50.97 ± 1.89	15.82 ± 1.71	0.69 ± 0.02
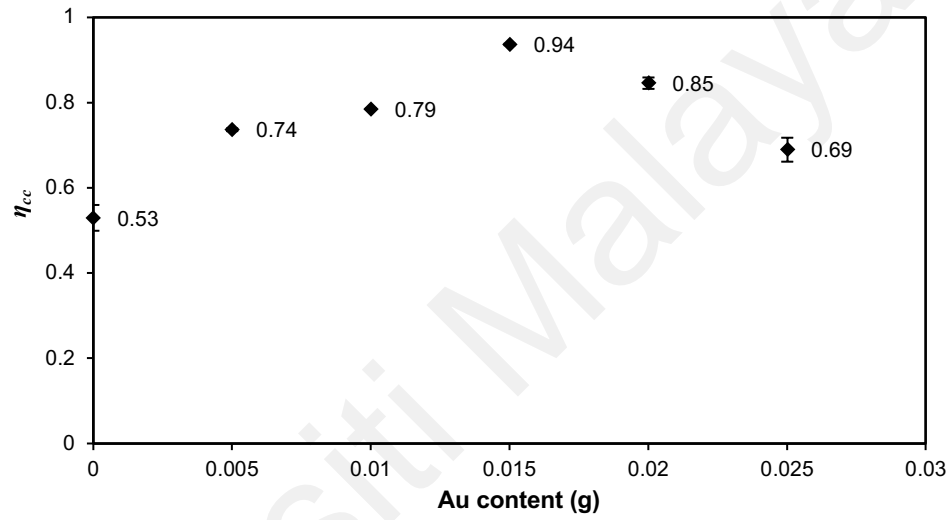
Figure 4.10: Charge collection efficiency, η_{cc} for DSSC with TiO₂/Au photoanode.

4.5 Summary

Au NPs showed improvement compared to the DSSC without the NPs. The cell with 3 wt.% Au NP exhibited 8.54 % efficiency, which is the best performance among other cells. The cell with photoanode containing 3 wt.% Au NPs exhibited the highest J_{sc} of 19.82 mA cm^{-2}, V_{oc} of 0.72 V and *FF* of 0.60%. The cell also exhibited the lowest electron transport time, τ_{tr} of 7.32 ms, and highest recombination time, τ_{rec} of 115.33 ms.

CHAPTER 5: CHARACTERISTICS OF SILVER NANOPARTICLES ADDED TiO₂ DYE SENSITIZED SOLAR CELLS

[TiO₂(P90) + TiO₂(P25) + *x* Ag NP)–N3 dye/GPE/Pt]

5.1   Introduction

In this chapter, DSSCs with configuration [FTO/TiO₂(P90+P25)/AgNP−N3 dye/GPE/Pt/FTO] have been fabricated and characterized. The *J–V* characteristics and all parameters that can be obtained have been determined. Intensity modulated photovoltage spectroscopy (IMVS) and intensity modulated photocurrent spectroscopy (IMPS) measurements were carried out. The highest conducting GPE that contained 4.16 wt.% PhCh−1.04 wt.% PEO−26.00 wt.% DMF−31.20 wt.% EC−18.70 wt.% TPAI−7.10 wt.% TBP−7.4 wt.% BMII−3 wt.% GuSCN−1.4 wt.% I₂ was used to fabricate the DSSC with area 0.20 cm². I₂ was added to form the I^- / I_3^- redox couple. Results will be described in the following sections.

5.2   Photovoltaic Measurement

The DSSCs with configuration [FTO/TiO₂(P90+P25)+*x* AgNP)–N3 dye/GPE/Pt/ FTO] were fabricated and characterized. The *x* values 0 wt.%, 1 wt.%, 2 wt.%, 3 wt.%, 4 wt.% and 5 wt.%. The photovoltaic characteristics (*J–V*) of these cells have been presented in Figure 51. Table 5.1 displays the open−circuit voltage (V_{oc}), short−circuit current density (J_{sc}), fill factor (*FF*), and efficiency (*η*). These values were obtained from photovoltaic data. Figure 5.1. depicts the *J–V* characteristics for AG0 to AG5. The characteristics of these curves are summarized in Table 5.1.
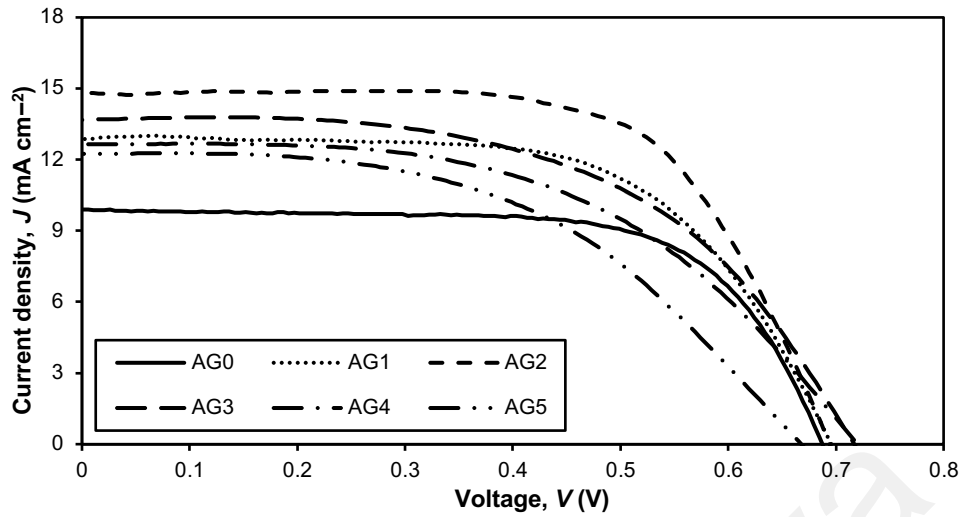
Figure 5.1: *J–V* plots of [TiO$_2$(P90) + TiO$_2$(P25) + *x* Ag NP)–N3 dye/GPE/Pt] for DSSCs with TiO$_2$/Ag photoanode.

Table 5.1 details the various information obtained from the *J−V* curves. Following the variation of nanoparticle content, J_{sc} and efficiency (η) of DSSC increase with increasing silver nanoparticle concentration. The maximum J_{sc} (14.25±0.71 mAcm^{-2}) and η (6.99±0.14) % were exhibited by the DSSC with 2 wt.% gold nanoparticle content. The efficiency then decreased with the further addition of Ag NPs. The voltage, V_{oc}, reached (0.70±0.01) *V*, and the fill factor reached the maximum value of (70.00±3.80) % for the DSSC with maximum efficiency.

The smallest J_{sc} value of (9.90±0.03) mA cm^{-2} was exhibited by the cell that did not contain Ag NPs. This cell exhibited the lowest η of (4.59±0.01) %. Increasing the Ag NP content from 1 wt.% to 2 wt.%, the J_{sc}, V_{oc}, and η increased to (12.91±0.38) mA cm^{-2}, (0.69±0.01) *V*, (5.48±0.31) % for AG1 and (14.25±0.71) mAcm^{-2}, (0.70±0.01) *V*, (6.99±0.14) % for the AG2 DSSC, respectively. From 3 wt.% to 5 wt.%, the J_{sc} also decreased following the trend (13.25±0.57) mA cm^{-2}, (12.53±0.12) mA cm^{-2}, (11.75±0.46) mA cm^{-2}, respectively.

57

Table 5.1: Values of J_{sc}, V_{oc}, FF, and η obtained from J–V curves in Figure 5.1.

Designation	Ag (g)	J_{sc} (mA cm^{-2})	V_{oc} (V)	FF (%)	η (%)
AG0 (0 wt.%)	0	9.90 ± 0.03	0.69 ± 0.01	67.41 ± 0.34	4.59 ± 0.01
AG1 (1 wt.%)	0.005	12.91 ± 0.38	0.69 ±0.01	61.11 ± 2.79	5.48 ± 0.31
AG2 (2 wt.%)	0.01	14.25 ± 0.71	0.70 ± 0.01	70.00 ± 3.80	6.99 ± 0.14
AG3 (3 wt.%)	0.015	13.25 ± 0.57	0.71 ± 0.01	57.33 ± 3.10	5.42 ± 0.03
AG4 (4 wt.%)	0.02	12.53 ± 0.12	0.72 ±0.01	52.00 ± 1.08	4.69 ± 0.13
AG5 (5 wt.%)	0.025	11.75 ± 0.46	0.66 ± 0.01	54.00 ± 2.81	4.16 ± 0.02

Figure 5.2 shows the short−circuit current density, J_{sc} for DSSC with TiO$_2$/Ag photoanode.
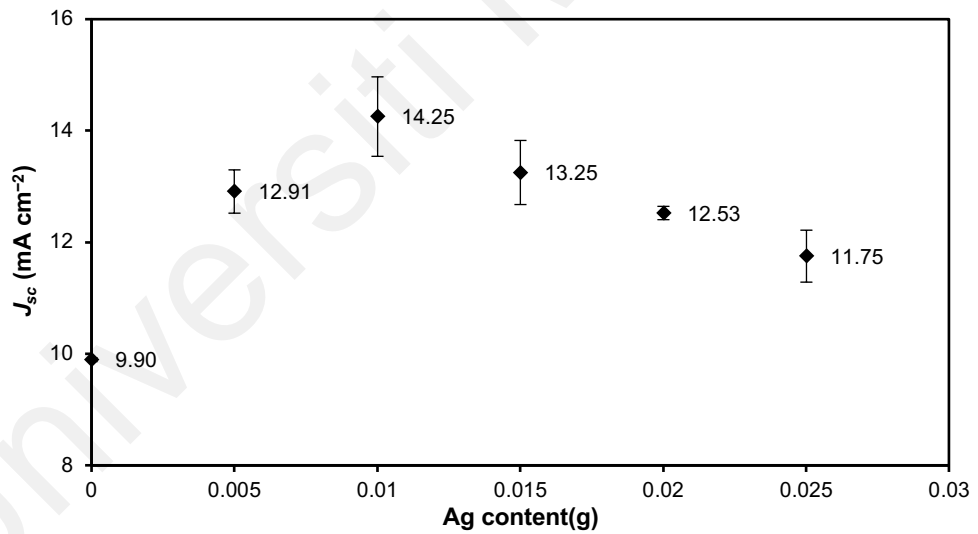
Figure 5.2: Short−circuit current density, J_{sc} for DSSC with TiO$_2$/Ag photoanode.

Figure 5.3 shows the open−circuit voltage, V_{oc} for DSSCs with different Ag content in the TiO$_2$/Ag photoanode. Figure 5.4 shows the fill factor for DSSC with different Ag content in the TiO$_2$/Ag photoanode. Figure 5.5 shows the power conversion efficiency, η for DSSC with different Ag content in the TiO$_2$/Ag photoanode.
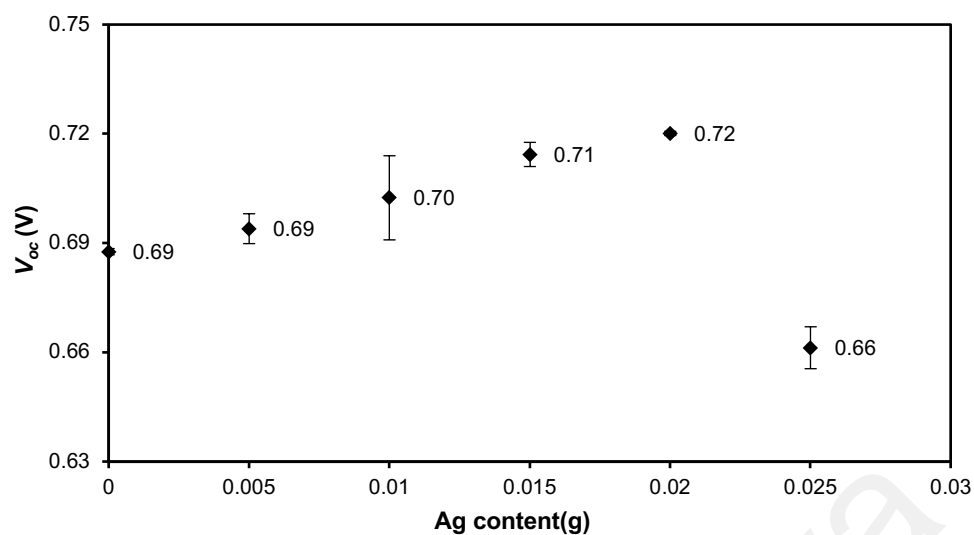
Figure 5.3: Open−circuit voltage, V_{oc} for DSSC with TiO₂/Ag photoanode.
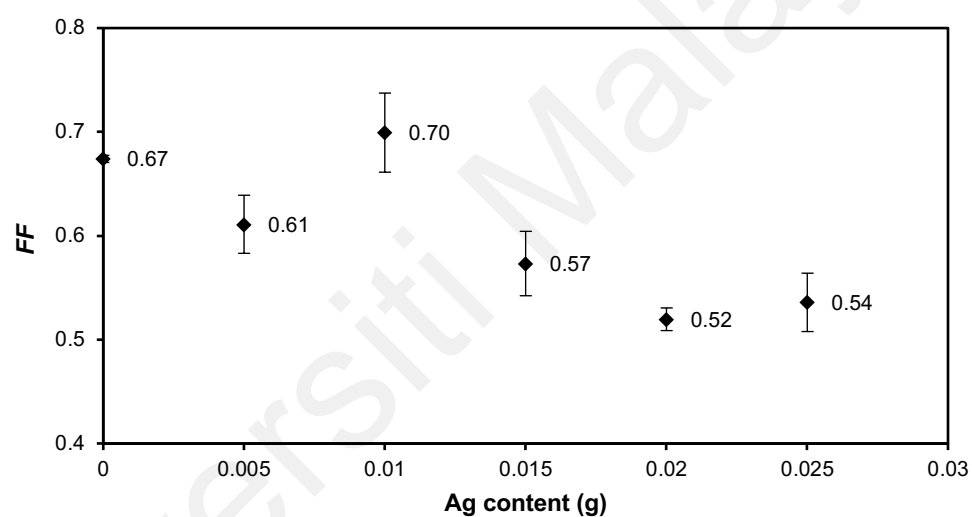
Figure 5.4: Fill Factor (*FF*) for DSSC with TiO₂/Ag photoanode.
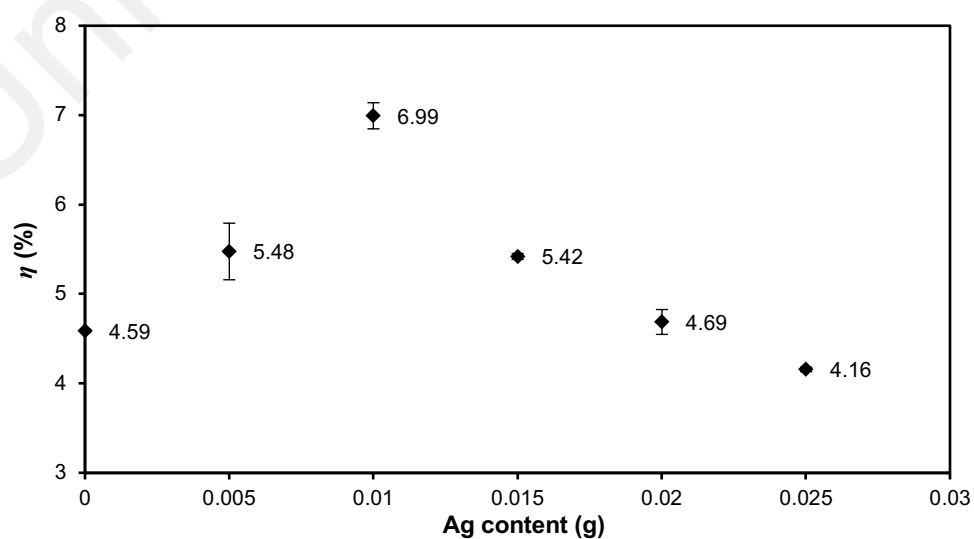
Figure 5.5: Power conversion efficiency, *η* for DSSC with TiO₂/Ag photoanode.

59

5.3 IMVS/IMPS

Figure 5.6 is the variation of τ_{rec} for DSSCs with different Ag content in the TiO$_2$/Ag photoanode. The IMVS experimental curves from the Nyquist plots at the base intensities as same for IMPS. The frequencies f_{IMVS} were obtained from the maxima of the Nyquist plots. The f_{IMVS} is associated with τ_{rec}. The τ_{rec}, τ_{tr} and η_{cc} were calculated from the corresponding characteristic frequencies using the equations (3.9), (3.10), and (3.11) of Chapter 3, respectively. IMPS curves as Nyquist−type plots posed a maximum at intermediate frequencies, f_{IMPS}. This value gives the electron τ_{tr} in the DSSC and it happened in the order of a few milliseconds through the mesoporous TiO$_2$.
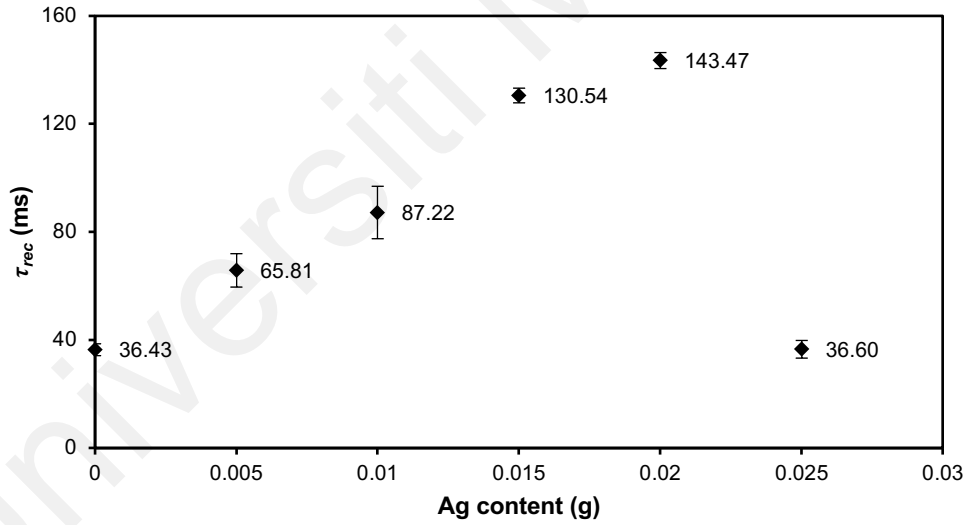
Figure 5.6: Recombination time, τ_{rec} for DSSC with TiO$_2$/Ag photoanode.

Figure 5.7 coresponds to how the electron transport time, τ_{tr} (ms) changes with Ag content for the DSSCs with TiO$_2$/Ag photoanode. The IMVS and IMPS experiments have been performed at 0.09 mW intensity of red LED light (627 nm). From the IMVS experiment, recombination time, τ_{rec} graph has been depicted in Figure 5.6 and from the

IMPS experiment electron transport time, τ_{tr} graph have been depicted in Figure 5.7. All the values have been tabulated in Table 5.2.

It can be observed that the DSSC containing 2 wt.% Ag NP in the photoanode exhibited the lowest τ_{tr} value (7.00±0.41) ms, the τ_{rec} value is (87.22±9.1) ms and highest η_{cc} of (0.92±0.01). The η_{cc} for 0 wt.%, 1 wt.%, 2 wt.%, 3 wt.%, 4 wt.% and 5 wt.% Ag nanoparticle photoanodes are (0.53±0.03), (0.81±0.01), (0.92±0.01), (0.91±0.01), (0.91±0.01) and (0.61±0.04), respectively. Figures 5.6, 5.7, and 5.8 show the relationship among τ_{rec}, τ_{tr} and, η_{cc} versus Ag content in grams for the solar cells fabricated. The graphs of electron transfer time, τ_{tr} for DSSCs with different Ag content in the TiO$_2$/Ag photoanodes are depicted in Figure 5.7. The values of τ_{rec}, τ_{tr} and, η_{cc} from IMVS and IMPS measurements are tabulated in Table 5.2.
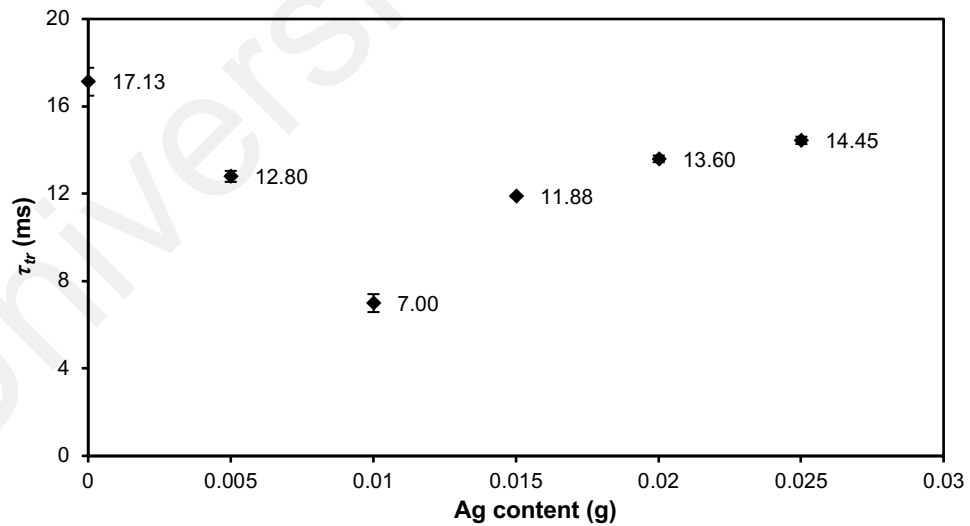
Figure 5.7: Electron transport time, τ_{tr} for DSSC with TiO$_2$/Ag photoanode.

Table 5.2: Values of τ_{rec}, τ_{tr} and η_{cc} obtained from IMVS/IMPS.

Designation	Ag (g)	τ_{rec} (ms)	τ_{tr} (ms)	η_{cc}
AG0 (0 wt.%)	0	36.43 ± 2.19	17.13 ± 0.64	0.53 ± 0.03
AG1 (1 wt.%)	0.005	65.81 ± 6.18	12.80 ± 0.25	0.81 ± 0.01
AG2 (2 wt.%)	0.01	87.22 ± 9.17	7.00 ± 0.41	0.92 ± 0.01
AG3 (3 wt.%)	0.015	130.54 ± 2.72	11.88 ± 0.03	0.91 ± 0.01
AG4 (4 wt.%)	0.02	143.47 ± 2.96	13.60 ± 0.15	0.91 ± 0.01
AG5 (5 wt.%)	0.025	36.60 ± 3.27	14.45 ± 0.17	0.61 ± 0.04
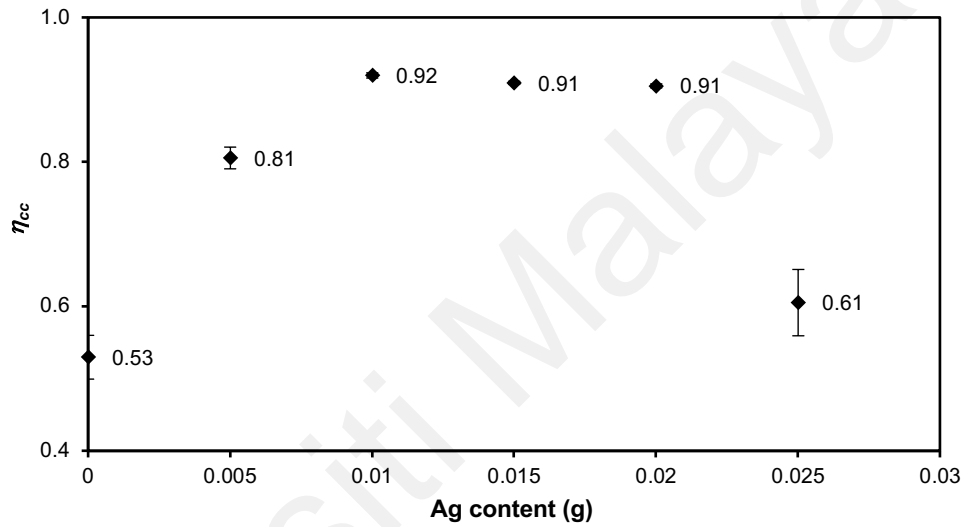
Figure 5.8: Charge collection efficiency, η_{cc} DSSC with TiO₂/Ag photoanode.

5.4 Summary

Ag NPs have shown significant effect in DSSC application. The cell with 2 wt.% composite exhibited (6.99±0.14) % efficiency, which is the best performance among other cells. Increasing Ag NPS content from 1 wt.% to 2 wt.%, increased J_{sc}, V_{oc} and η following the trend (12.91±0.38) mA cm⁻², (0.69±0.01) V, (5.48±0.31) % and (14.25±0.71) mAcm⁻², (0.70±0.01) V, (6.99±0.14) % respectively. From 3 wt.% to 5 wt.%, J_{sc}, fill factor and η decreased following the trend of (13.25±0.57) mA cm⁻², (57.33±3.10) %, and (5.42±0.03) % to (12.53±0.12) mA cm⁻², (51.97±1.08) %, and (4.69±0.13) % to (11.75±0.46) mA cm⁻², (54.00±2.81) % and (4.16±0.02) %. It can be

observed that the DSSC containing 2 wt.% Ag nanoparticles in the photoanode exhibited the lowest τ_{tr} value (7.00±0.41) ms, τ_{rec} value (87.22±9.17) ms and highest charge collection efficiency, η_{cc} of (0.92±0.01).

CHAPTER 6: CHARACTERISTICS OF COPPER NANOPARTICLES ADDED TiO₂ DYE SENSITIZED SOLAR CELLS

[TiO₂(P90) + TiO₂(P25) + *x* Cu NP)–N3 dye/GPE/Pt]

6.1 Introduction

In this chapter, the highest conducting GPE with composition 4.16 wt.% PhCh−1.04 wt.% PEO−26.00 wt.% DMF−31.20 wt.% EC−18.70 wt.% TPAI−7.10 wt.% TBP−7.4 wt.% BMII−3 wt.% GuSCN−1.4 wt.% I_2 (Shah et al., 2019) was used in the fabrication of [FTO/TiO₂ (P90 + P25)/Cu NP)–N3 dye/GPE/Pt/FTO] DSSCs. The cells were also characterized in the same manner as mentioned in the former chapters. A total of six cells were fabricated in order to obtain consistency in the results.

6.2 *J–V* Characteristics

In order to determine the Cu content that will exhibit the highest efficiency, the system consisting different Cu content in the DSSCs, [TiO₂(P90) + TiO₂(P25) + *x* Cu NP–N3 dye/GPE/Pt] were fabricated. In this thesis the values of *x* were 0 wt.%, 1 wt.%, 2 wt.%, 3 wt.%, 4 wt.% and 5 wt.%. The *J–V* characteristics of these cells are presented in Figure 6.1. Table 6.1 displays the open−circuit voltage (V_{oc}), short−circuit current density (J_{sc}), fill factor (*FF*), and efficiency (*η*) which were estimated from the photovoltaic data.
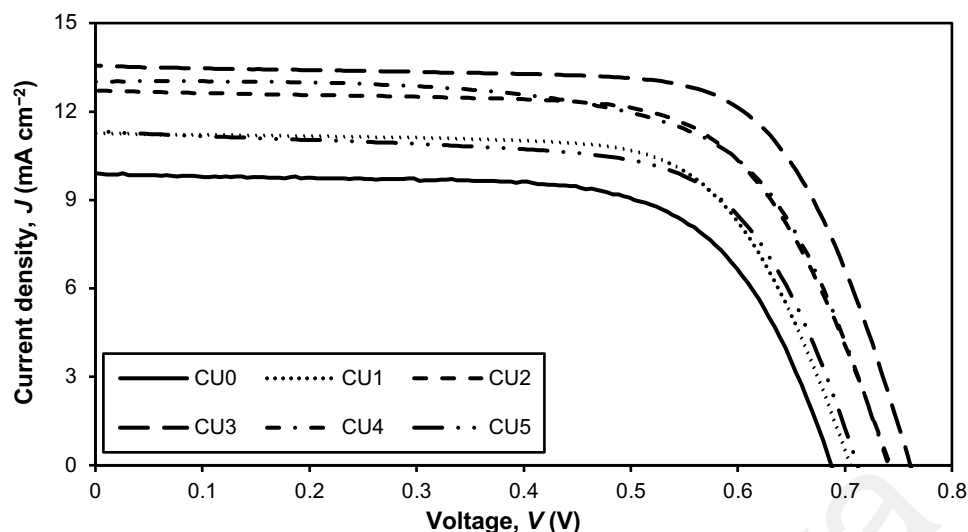
Figure 6.1: *J–V* plot for DSSC with TiO₂/Cu photoanode.

Table 6.1: The values of J_{sc}, V_{oc}, *FF,* and *η* obtained from Figure 6.1.

Designation	Cu (g)	J_{sc} (mA cm^{-2})	V_{oc} (V)	*FF* (%)	*η* (%)
CU0 (0 wt.%)	0	9.90 ± 0.03	0.69 ± 0.01	67.41 ± 0.34	4.59 ± 0.01
CU1 (1 wt.%)	0.005	11.15 ± 0.42	0.71 ± 0.01	69.32 ± 0.62	5.45 ± 0.14
CU2 (2 wt.%)	0.01	12.88 ± 0.24	0.74 ± 0.01	67.00 ± 0.71	6.34 ± 0.04
CU3 (3 wt.%)	0.015	13.35 ± 0.19	0.76 ± 0.01	71.00 ± 0.15	7.19 ± 0.08
CU4 (4 wt.%)	0.02	12.28 ± 0.67	0.74 ± 0.01	67.14 ± 1.94	6.12 ± 0.17
CU5 (5 wt.%)	0.025	11.21 ± 0.12	0.72 ± 0.01	67.64 ± 0.70	5.47 ± 0.06

Figure 6.2 shows the short−circuit current density, J_{sc}; Figure 6.3 shows open−circuit voltage, V_{oc}; Figure 6.4 shows fill factor, *FF* and Figure shows 6.5 shows power conversion efficiency, *η* for DSSC with TiO₂/Cu photoanode as a function of Cu content.

It can be observed that J_{sc} and efficiency, *η* of DSSC increased with increasing copper nanoparticle concentration until the J_{sc} and *η* values achieved a maximum at (13.35±0.19) mA cm^{-2} and (7.19±0.08) %, respectively. This is true for the 3 wt.% copper nanoparticle content. On increasing the Cu NP content, the efficiency was observed to

decrease. The voltage, V_{oc}, and fill factor for the DSSC with 3 wt.% Cu content are (0.76±0.01) V and (71.00±0.15) % respectively.

The cell with 0 wt.% Cu NP exhibits the lowest J_{sc} of (9.90±0.03) mAcm^{-2} and η of (4.59±0.01) %. Increasing the Cu NP content from 1 wt.% to 3 wt.%, the J_{sc}, V_{oc}, FF, and η also increased following the trend from (11.15±0.42) mA cm^{-2}, (0.71±0.01) V, (69.32±0.62) %, and (5.45±0.14) % to (12.88±0.24) mA cm^{-2}, (0.74±0.01) V, (67.00±0.71) %, and (6.34±0.04) % to (13.35±0.19) mA cm^{-2}, (0.76±0.01) V, (71.00±0.15) %, and (7.19±0.08) % respectively. From 4 wt.% to 5 wt.%, the J_{sc}, V_{oc}, FF and η also decreased following the trend from (12.28±0.67) mA cm^{-2}, (0.74±0.01) V, (67.14±1.94) %, and (6.12±0.17) % to (11.21±0.12) mA cm^{-2}, (0.72±0.01) V, (67.64±0.70) %, and (5.47±0.06) %.
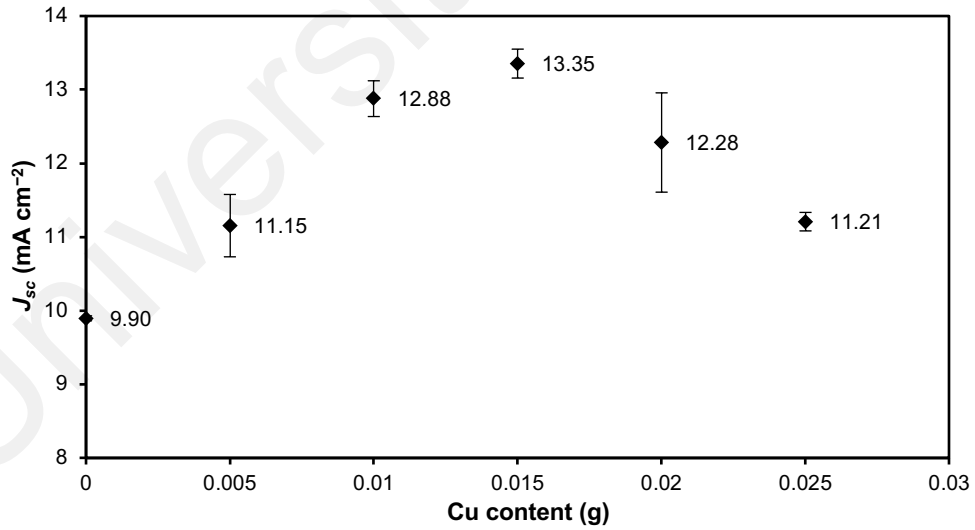
Figure 6.2: Short−circuit current density, J_{sc} for DSSC with TiO$_2$/Cu photoanode.
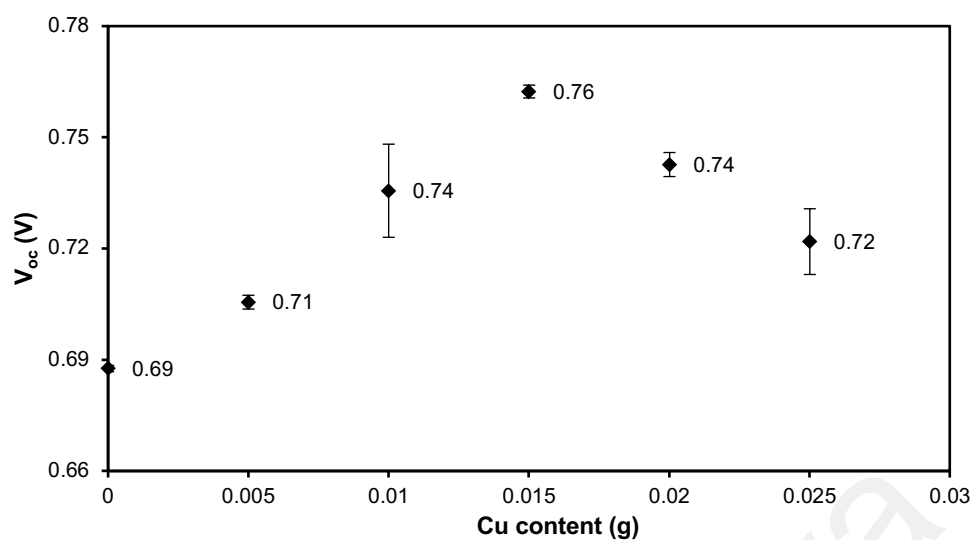
Figure 6.3: Open−circuit voltage, V_{oc} for DSSC with TiO₂/Cu photoanode.
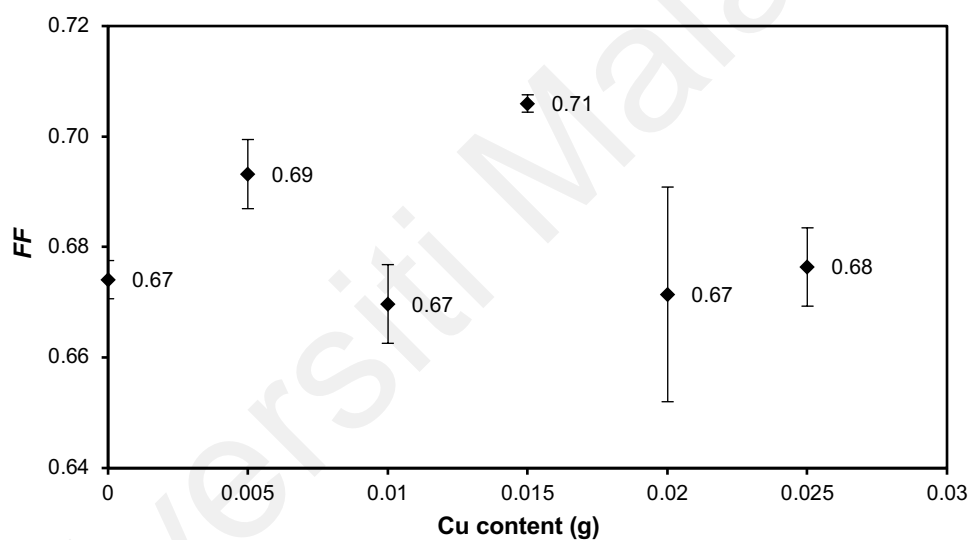
Figure 6.4: Fill factor, *FF* for DSSC with TiO₂/Cu photoanode.
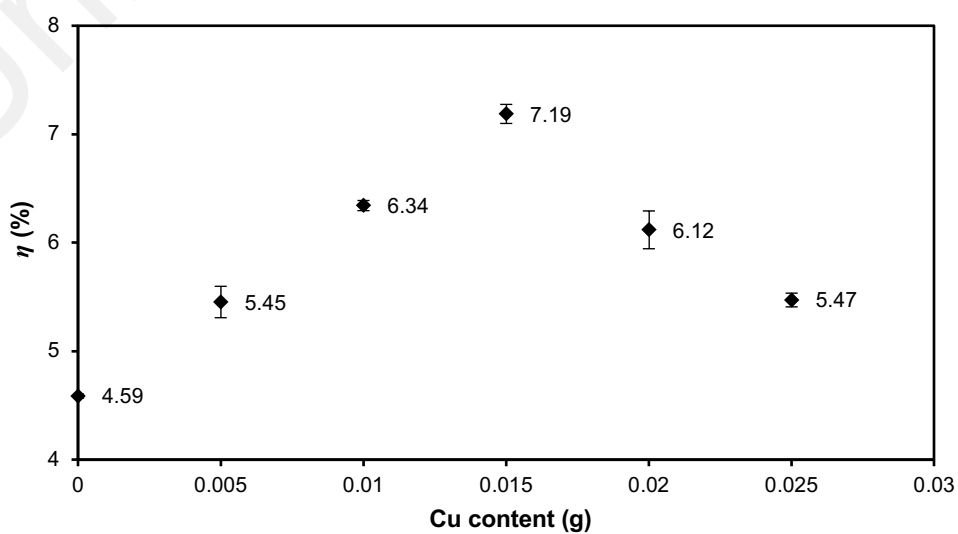
Figure 6.5: Power conversion efficiency, *η* for DSSC with TiO₂/Cu photoanode.

6.3 IMVS/IMPS

From the IMVS experiment, recombination time, τ_{rec} graph has been depicted in Figure 6.6. The frequencies f_{IMVS} were obtained from the maxima of the Nyquist plots. The f_{IMVS} is associated with τ_{rec}. The τ_{rec}, τ_{tr} and η_{cc} were calculated from corresponding characteristic frequencies using the equations (3.9), (3.10), and (3.11) of Chapter 3, respectively.
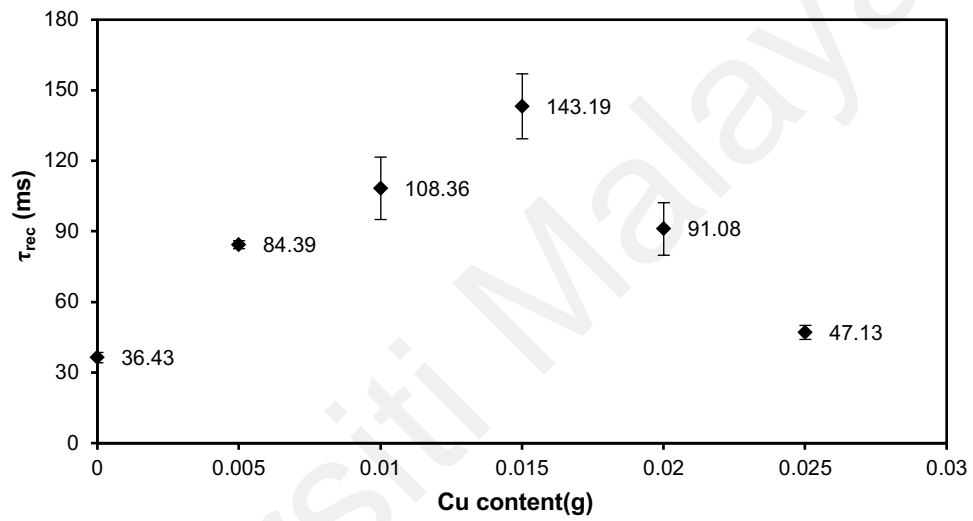
Figure 6.6: Recombination time, τ_{rec} for DSSC with TiO₂/Cu photoanode.

IMPS curves as Nyquist−type plots posed a maximum at intermediate frequencies, f_{IMPS} which is the characteristic parameter for the transportation of electrons through the TiO₂ pores to the back layer. This value gives the electron τ_{tr} in the DSSC and it happened in the order of a few milliseconds through the mesoporous TiO₂.

The IMVS and IMPS experiments have been performed at 0.09 mW intensity of red LED light (627 nm). From the IMPS experiment, electron transport time, τ_{tr} graph have been depicted in Figure 6.7. All the values have been tabulated in Table 6.2. It can be observed that the DSSC containing 3 wt.% Cu nanoparticles in the photoanode exhibited

the lowest τ_{tr} value (2.30±0.07) ms, τ_{rec} value (143.19±13.81) ms, and highest charge

collection efficiency, η_{cc} of (0.98±0.01). The efficiency of charge collection for DSSCs

containing 0 wt. %, 1 wt.%, 2 wt.%, 3 wt.%, 4 wt.% and 5 wt.% Cu nanoparticles in the

photoanode are (0.53±0.03), (0.84±0.01), (0.97±0.01), (0.98±0.01), (0.96±0.01) % and

(0.85±0.03), respectively. Figures 6.6 and 6.7 show the relationship between τ_{rec} and

τ_{tr}, of the Cu content in grams for the solar cells fabricated. Figure 6.8 exhibits the charge

collection efficiency, η_{cc} for DSSCs with varying Cu content in the TiO₂/Cu photoanode.
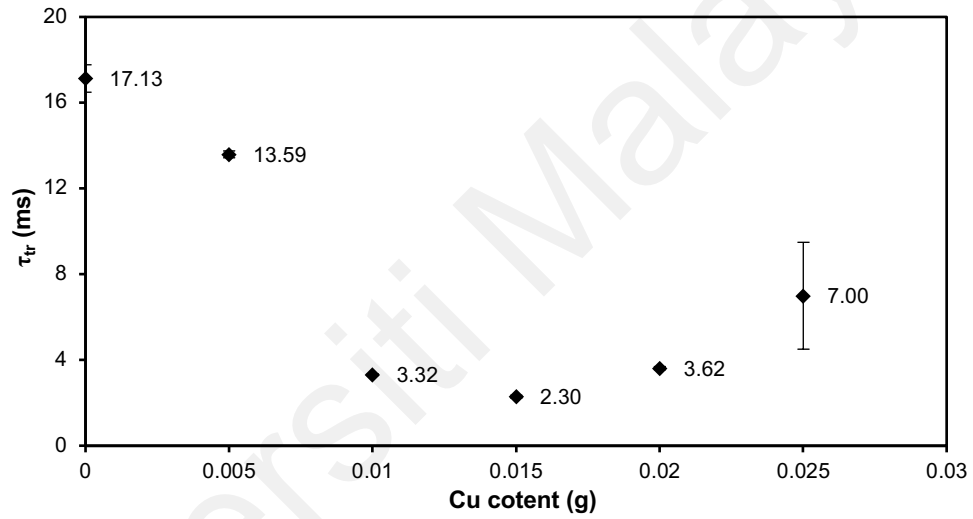
Figure 6.7: Electron transport time, τ_{tr} for DSSC with TiO₂/Cu photoanode.

Table 6.2: Values of τ_{rec}, τ_{tr} and η_{cc} obtained from IMVS/IMPS.

Designation	Cu (g)	τ_{rec} (ms)	τ_{tr} (ms)	η_{cc}
CU0 (0 wt.%)	0	36.43 ± 2.19	17.13 ± 0.64	0.53 ± 0.03
CU1 (1 wt.%)	0.005	84.39 ± 1.70	13.59 ± 0.16	0.84 ± 0.01
CU2 (2 wt.%)	0.01	108.36 ± 13.81	3.32 ± 0.04	0.97 ± 0.01
CU3 (3 wt.%)	0.015	143.19 ± 13.81	2.30 ± 0.07	0.98 ± 0.01
CU4 (4 wt.%)	0.02	91.08 ± 11.16	3.62 ± 0.08	0.98 ± 0.01
CU5 (5 wt.%)	0.025	47.13 ± 2.98	7.00 ± 2.49	0.85 ± 0.03
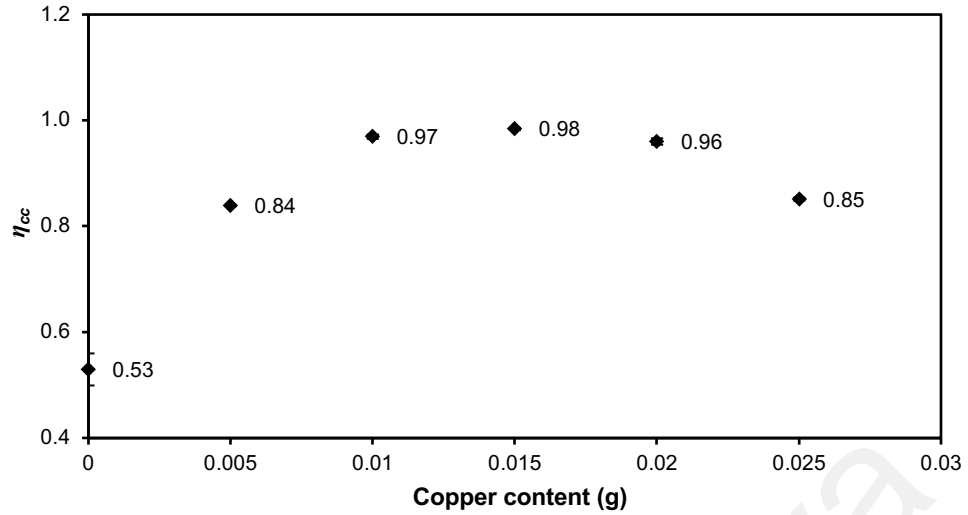
Figure 6.8: Charge collection efficiency, η_{cc} for DSSC with TiO₂/Cu photoanode.

6.4 Summary

Cu NPs have significantly improved DSSC efficiency. The best performing DSSC contained 3 wt.% Cu NPs with J_{sc}, V_{oc}, *FF* and η of (13.35 ± 0.19) mA cm^{-2}, (0.76 ± 0.01) V, (71.00 ± 0.15) %, (7.19 ± 0.08) %. With increased Cu NP content from 1 wt.% to 3 wt.%, the J_{sc}, V_{oc} and η also increased following the trend (11.15 ± 0.42) mA cm^{-2}, (0.71 ± 0.01) V, (5.45 ± 0.14) %: (12.88 ± 0.24) mA cm^{-2}, (0.74 ± 0.01) V, (6.34 ± 0.04) % : (13.35 ± 0.19) mA cm^{-2}, (0.76 ± 0.01) V, (7.19 ± 0.08) %, respectively. It can be observed that the DSSC contains 0 wt.%, 1 wt.%, 2 wt.%, 3 wt.%, 4 wt.% and 5 wt.% Cu nanoparticles in the photoanode exhibit the charge collection efficiency, η_{cc} is (0.53 ± 0.03), (0.84 ± 0.01), (0.97 ± 0.01), (0.98 ± 0.01), (0.96 ± 0.01) and (0.85 ± 0.03), respectively.

CHAPTER 7: CHARACTERISTICS OF PLATINUM ADDED TiO$_2$ DYE SENSITIZED SOLAR CELLS

[TiO$_2$(P90) + TiO$_2$(P25) + *x* Pt NP)–N3 dye/GPE/Pt]

7.1   Introduction

In this chapter platinum, Pt, has been added as plasmonic material with TiO$_2$ semiconductor. As with other additives, in the previous chapters, the characteristics of Pt added DSSCs would be explored. For this purpose, [FTO/TiO$_2$(P90+P25)/Pt NP–N3 dye/GPE/Pt/FTO] DSSCs were fabricated and the optimum Pt composition in the photoanode will be determined. It is to be noted that Pt was also used in the cathode of the DSSCs.

7.2   Photovoltaic Measurements

The photovoltaic (*J–V*) measurements of the DSSCs with configuration [TiO$_2$(P90) + TiO$_2$(P25) + *x* Pt NP)–N3 dye/GPE/Pt] were studied. As in the previous chapters, the values of *x* are 0 wt.%, 1 wt.%, 2 wt.%, 3 wt.%, 4 wt.% and 5 wt.%. The characteristics (*J–V*) of these cells have been presented in Figure 7.1. Table 7.1 displays the open−circuit voltage (V_{oc}), short−circuit current density (J_{sc}), fill factor (*FF*), and efficiency (*η*) which have been estimated from the photovoltaic data.

Figure 7.1 and Table 7.1 shows *J−V* curve of platinum nanoparticles and with nanoparticles based DSSCs and parameters of DSSCs. Figures 7.2 to 7.5 show the short−circuit current density (J_{sc}), the open−circuit voltage (V_{oc}), fill factor (*FF*) and the efficiency (*η*) versus Pt NP content in grams for the solar cells fabricated.
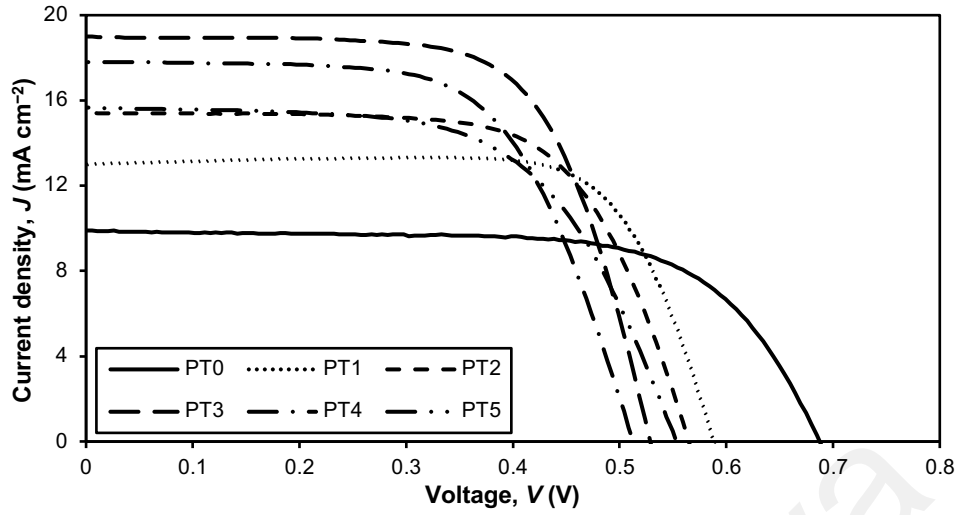
Figure 7.1: $J-V$ plot of DSSC with TiO₂/Pt photoanode.

Table 7.1: Values of J_{sc}, V_{oc}, FF and η obtained from Figure 7.1.

Designation	Pt (g)	J_{sc} (mA cm⁻²)	V_{oc} (V)	FF (%)	η (%)
PT0 (0 wt.%)	0	9.90 ± 0.03	0.69 ± 0.01	67.41 ± 0.34	4.59 ± 0.01
PT1 (1 wt.%)	0.005	13.62 ± 0.92	0.58 ± 0.01	73.00 ± 3.18	5.70 ± 0.01
PT2 (2 wt.%)	0.01	15.62 ± 0.29	0.56 ± 0.00	72.58 ± 1.37	5.81 ± 0.06
PT3 (3 wt.%)	0.015	19.60 ± 0.57	0.51 ± 0.01	65.01 ± 2.78	6.54 ± 0.26
PT4 (4 wt.%)	0.02	17.55 ± 0.44	0.53 ± 0.01	64.00 ± 3.67	5.95 ± 0.19
PT5 (5 wt.%)	0.025	15.61 ± 0.03	0.55 ± 0.01	61.10 ± 0.62	5.29 ± 0.09

Following the variation of nanoparticle contents, J_{sc} and efficiency, η of DSSC increase with increasing platinum nanoparticle concentration. The maximum J_{sc} was (19.60±0.57) mA cm⁻² and the highest efficiency, η was (6.54±0.26) %. These characteristics were exhibited by the DSSC with 3 wt.% platinum nanoparticles and then efficiency decreased with further addition of Pt NPs. The voltage, V_{oc}, decreased upon adding Pt NPs from 1 wt.% to 3 wt.% following the trend (0.58±0.01) V, (0.56±0.01) V and (0.51±0.01) V but from 4 wt.% to 5 wt.% Pt nanoparticle concentration, the voltage was observed to increase to (0.53±0.01) V and (0.55±0.01) V, respectively.
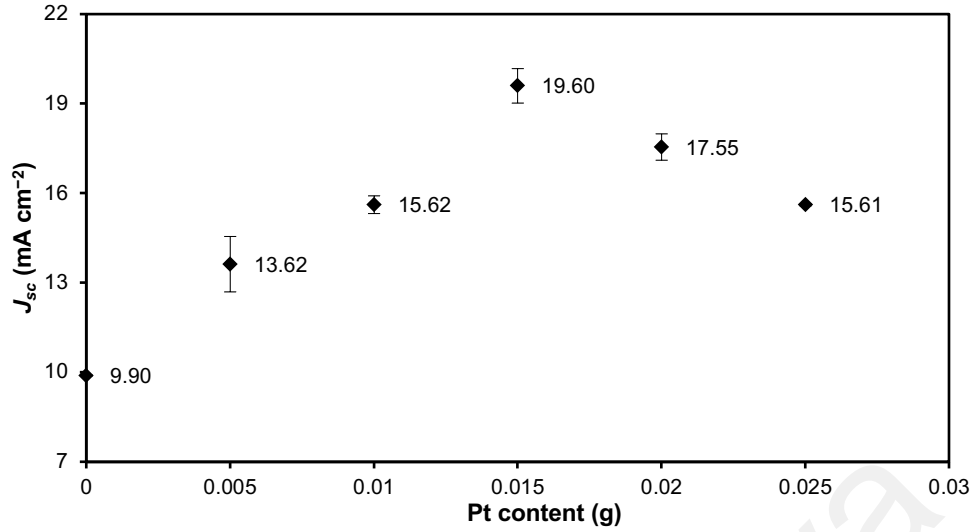
Figure 7.2: Short−circuit current density, J_{sc} for DSSCs with TiO₂/Pt photoanode.
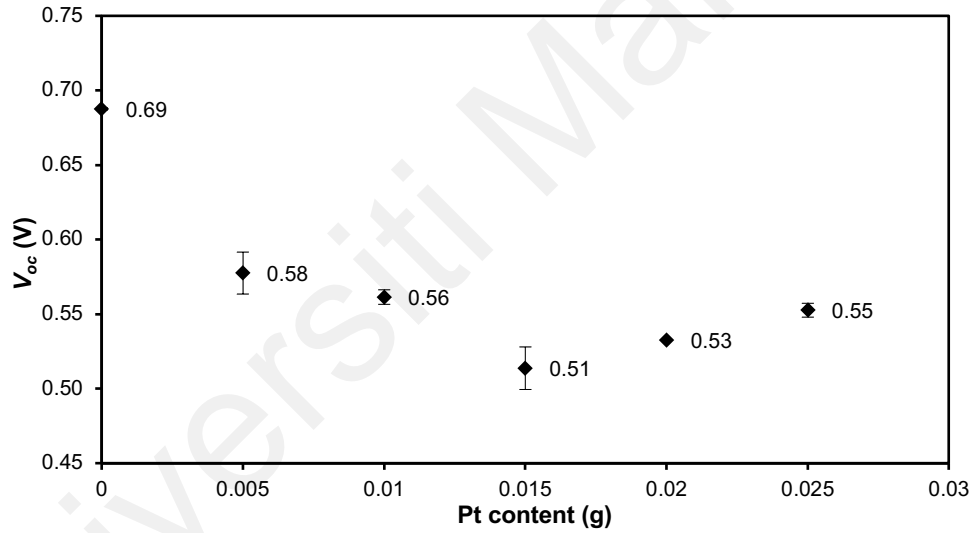
Figure 7.3: Open−circuit voltage, V_{oc} for DSSC with TiO₂/Pt photoanode.

The DSSC with 0 wt.% Pt NPs exhibited the lowest J_{sc} of (9.90±0.03) mA cm⁻² and η of (4.59±0.01) %. On increasing the Pt NPs content from 1 wt.% to 3 wt.%, the J_{sc}, and η also increased according to the trend (13.62±0.92) mA cm⁻², (5.70±0.01) %: (15.62±0.29) mA cm⁻², (5.81±0.06) %: (19.60±0.57) mA cm⁻², (6.54±0.26) %, respectively. From 4 wt.% to 5 wt.% of Pt NPs, the J_{sc}, and η also decreased as follows:

(17.55±0.44) mA cm^{-2}, (5.95±0.19) % for the DSSC with 4 wt.% Pt and (15.61±0.03)

mA cm^{-2}, (5.29±0.09) % for the 5 wt.% Pt contents.
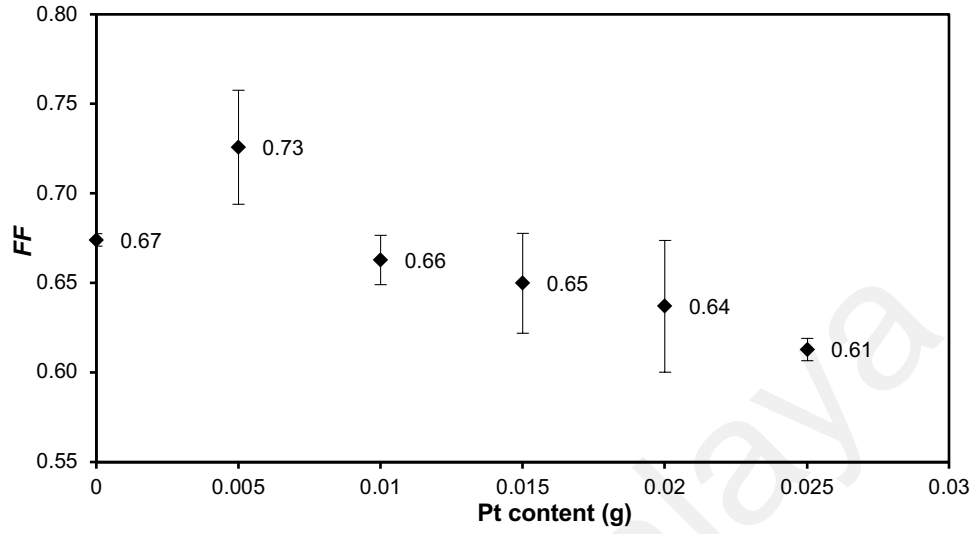
Figure 7.4: Fill factor, *FF* for DSSC with TiO₂/Pt photoanode.
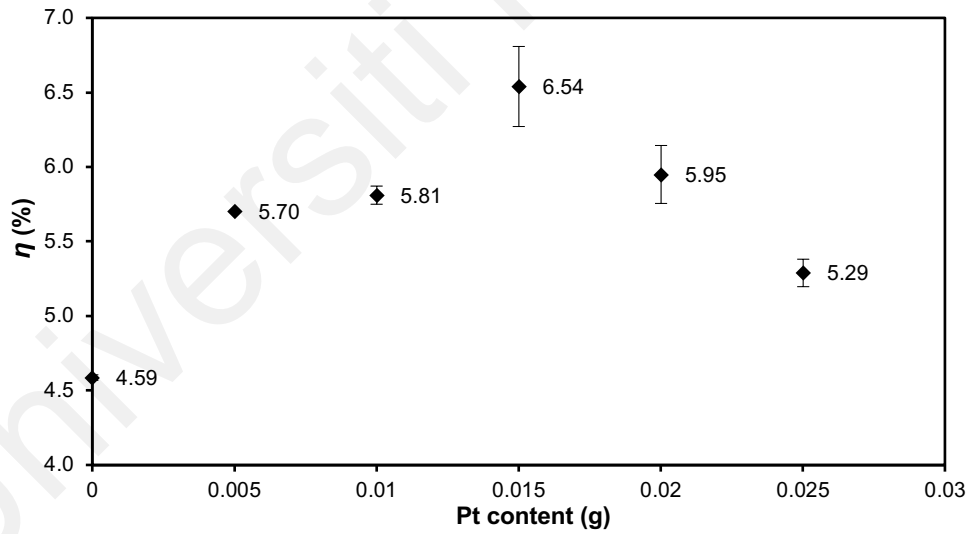
Figure 7.5: Power conversion efficiency, *η* for DSSC with TiO₂/Pt photoanode.

7.3 IMVS/IMPS

The IMVS frequency characteristic curves, f_{IMVS} are depicted in Figure 4.6. The

frequencies f_{IMVS} were obtained from the maxima of the Nyquist plots. The frequency,

f_{IMVS} is associated with electron τ_{rec}. The τ_{rec}, τ_{tr} and η_{cc} were calculated from

corresponding characteristic frequencies using the equations (3.9), (3.10) and (3.11) of Chapter 3, respectively. The maximum in the IMPS curves occur at intermediate frequencies, f_{IMPS}. This is the characteristic frequency for the transportation of electron through the TiO$_2$ pores to the back layer. This value gives the electron τ_{tr} in the DSSC and it occurred in the order of a few milliseconds through the mesoporous TiO$_2$. Table 7.2 lists the values of τ_{rec}, τ_{tr} and η_{cc} obtained from IMVS/IMPS results.
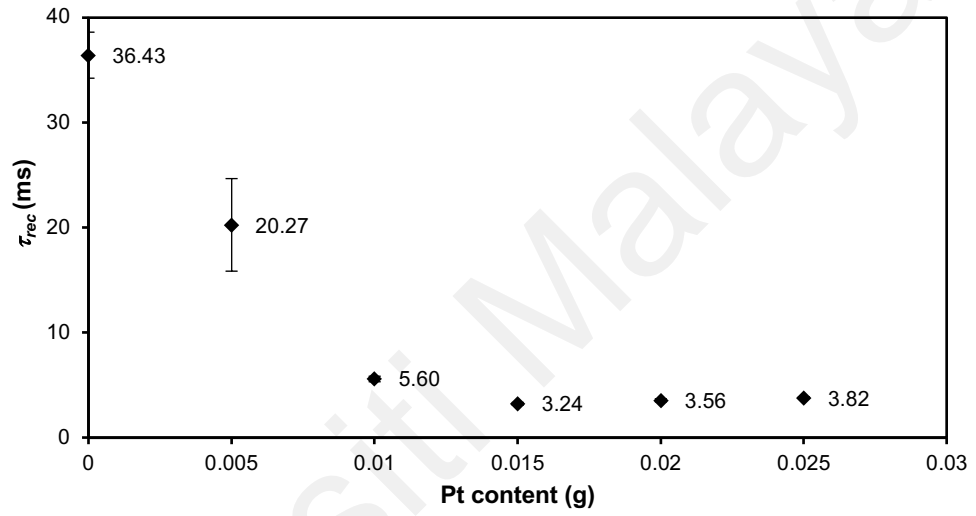
Figure 7.6: Recombination time, τ_{rec} for DSSC with TiO$_2$/Pt photoanode.
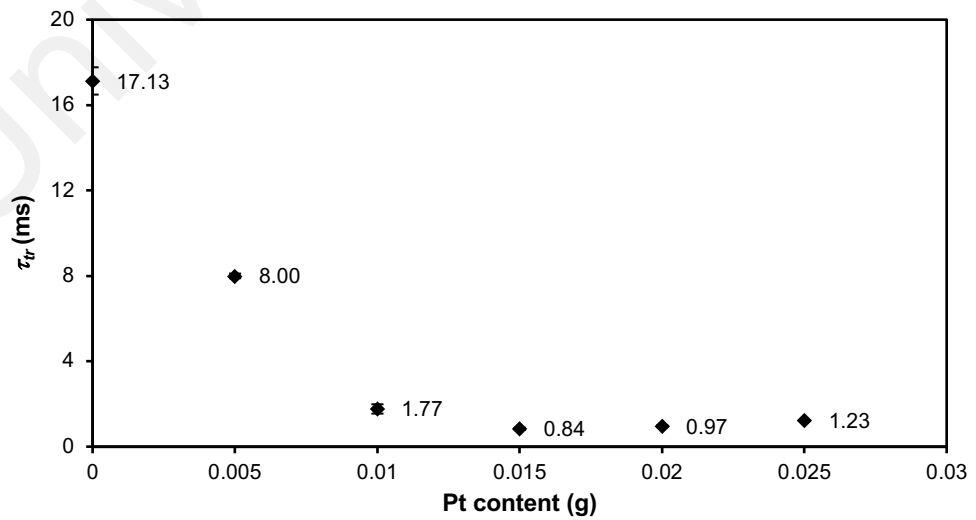
Figure 7.7: Electron transport time, τ_{tr} for DSSC with TiO$_2$/Pt photoanode.

Table 7.2: Values of τ_{rec}, τ_{tr} and η_{cc} obtained from IMVS/IMPS.

Designation	Pt (g)	τ_{rec} (ms)	τ_{tr} (ms)	η_{cc}
PT0 (0 wt.%)	0	36.43 ± 2.19	17.13 ± 0.64	0.53 ± 0.03
PT1 (1 wt.%)	0.005	20.27 ± 4.41	8.00 ± 0.11	0.61 ± 0.02
PT2 (2 wt.%)	0.01	5.60 ± 0.27	1.77 ± 0.22	0.68 ± 0.03
PT3 (3 wt.%)	0.015	3.24 ± 0.13	0.84 ± 0.05	0.74 ± 0.02
PT4 (4 wt.%)	0.02	3.56 ± 0.15	0.94 ± 0.04	0.73 ± 0.01
PT5 (5 wt.%)	0.025	3.82 ± 0.07	1.23 ± 0.03	0.68 ± 0.01

The Nyquist plots can be drawn from the IMVS and IMPS results at 0.09 mW intensity as presented in Figures 7.6 and 7.7. All the values have been tabulated in Table 7.2. It can be observed that the DSSC containing 3 wt.% platinum nanoparticles in the photoanode exhibited the lowest τ_{tr} value of (0.84±0.05) ms, lowest τ_{rec} value of (3.24±0.13) ms, but the overall charge collection efficiency, η_{cc} is highest being (0.74±0.02). The η_{cc} for 0 wt.%, 1 wt.%, 2 wt.%, 3 wt.%, 4 wt.% and 5 wt.% Pt nanoparticles in the DSSC photoanode are (0.53±0.03), (0.61±0.02), (0.68±0.03), (0.74±0.02), (0.73±0.01) and (0.68±0.01), respectively. Figures 7.6, 7.7, and 7.8 show the relationship between τ_{rec}, τ_{tr}, and η_{cc} versus Pt NPs content in grams for the solar cells fabricated. Figure 7.8 exhibits the charge collection efficiency, η_{cc} for DSSCs with varying Pt NP content in the TiO_2/Pt photoanode.
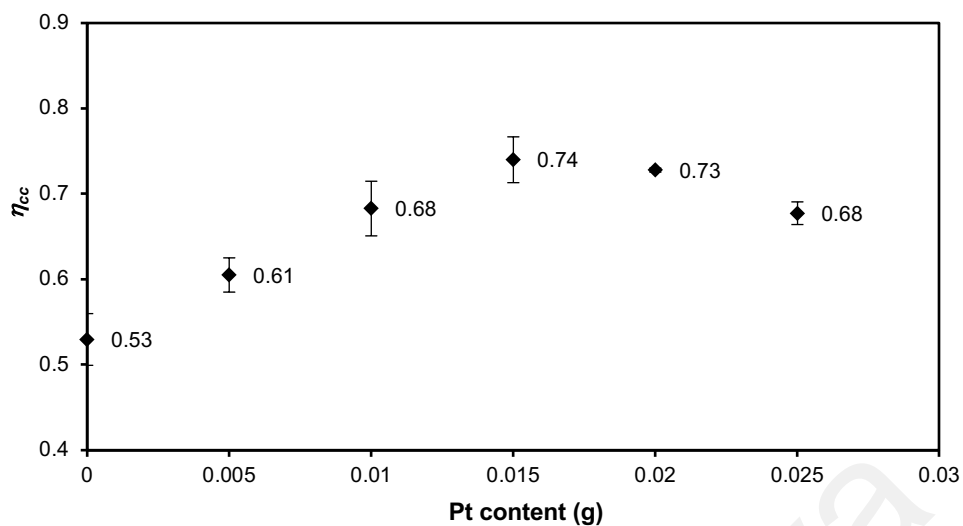
Figure 7.8: Charge collection efficiency, η_{cc}, for DSSC with TiO$_2$/Pt photoanode.

7.4   Summary

Pt NPs showed improvement in DSSC efficiency. The cell with 3 wt.% Pt NP exhibited (6.54±0.26) % efficiency and is the best performing cell. The cell with photoanode contained 3 wt.% Pt NPs exhibited highest J_{sc} of (19.60±0.57) mA cm^{-2}. The cell also exhibited the electron transport time, τ_{tr} of (0.84±0.05) ms. The overall charge collection efficiency, η_{cc} is highest with a value (0.74±0.02).

CHAPTER 8: DISCUSSION

The four series of DSSCs were prepared with the configuration of: (i) FTO/(TiO$_2$/AuNP)−N3 dye/GPE/Pt/FTO, (ii) FTO/(TiO$_2$/AgNP)−N3 dye/GPE/Pt/FTO, (iii) FTO/(TiO$_2$/PtNP)−N3 dye/GPE/Pt/FTO, (iv) FTO/(TiO$_2$/CuNP)−N3 dye/GPE/Pt/ FTO and characterized. The DSSCs were characterized by $J−V$, IMPS and IMVS techniques.

The maximum values are tabulated extracted from $J−V$ characteristic parameters: (open−circuit voltage (V_{oc}), short−circuit current (J_{sc}), fill factor (FF) and the efficiency (η) of the dye−sensitized solar cells (DSSCs) fabricated with the GPEs are presented in Table 8.1.

Table 8.1: Maximum values of short−circuit current (J_{sc}), open−circuit voltage (V_{oc}), fill factor (FF) and efficiency (η) for DSSCs fabricated with different plasmonic noble metals.

Nobel metals	J_{sc} (mA cm^{-2})	V_{oc} (mV)	FF (%)	η (%)
Without NP (0 wt.%)	9.90 ± 0.03	0.69 ± 0.01	67.41 ± 0.34	4.59± 0.01
Au NP (3 wt.%)	19.82 ± 0.11	0.72 ± 0.01	60.10 ± 0.38	8.54 ± 0.01
Ag NP (2 wt.%)	14.25 ± 0.71	0.70 ± 0.01	70.00 ± 3.80	6.99 ± 0.14
Cu NP (3 wt.%)	13.35 ± 0.19	0.76 ± 0.01	71.00 ± 0.15	7.19 ± 0.08
Pt NP (3 wt.%)	19.60 ± 0.57	0.51 ± 0.01	65.00 ± 2.7	6.54 ± 0.26

Specifically, it is expected that a comparison of $I−V$ measurements from a PV cell before and after the addition on nanoparticles should result in no change in V_{oc}, an increase in J_{sc}, and an increase in η, which corresponds to better light collection and more converted energy, respectively in the cell. The value of V_{oc} for the DSSC without nanoparticles is 0.68 V. The value of V_{oc} for the DSSC with 3 wt.% of Cu NP was the highest. In general, V_{oc} is determined as the difference between Fermi level of TiO$_2$ and

the electrolyte. This enhancement in V_{oc} could be due to the fact that incorporation of Cu^{2+} ions into TiO$_2$ induces extension of space charge region due to increased structural disorder. This elevated the conduction band (CB) edge of TiO$_2$. Therefore, the Fermi level is shifted towards the CB edge and consequently, the open−circuit voltage (V_{oc}) increases. The measured J_{sc} of the cell before the presence of nanoparticles was ~9.90 mA cm^{-2}. After forming a nanoparticle over the surface of the cell and taking the IV measurement again, the J_{sc} increased to ~13.35 mA cm^{-2}. As previously discussed in Chapter 2, J_{sc} indicates the amount of light captured by a cell. In this case, the presence of a nanoparticle array resulted in a net increase in light capture and subsequent increase in J_{sc}. Another important consideration is the measured V_{oc} of the cell. If formation of the nanoparticle array caused damage to the cell it could result in an overall lower efficiency. This is because recombination of carriers would negate any gains in light collection. This variation in V_{oc} is a result of process variations during the fabrication of the cells prior to formation of nanoparticles. As stated before and as observed for the majority of $I-V$ measurements, the V_{oc} before and after the presence of nanoparticles were nearly identical. The first PV cell in Table 4.1 had a change in V_{oc} after nanoparticles were applied.

In every DSSC fabricated, the J_{sc} increased when the nanoparticles were deposited on the surface of TiO$_2$ in the cell. Without nanoparticles cell exibits J_{sc} of 9.90 mA cm^{-2} and the relative increase in J_{sc} for PV cells with Cu, Ag, Pt and Au nanoparticles was 13.35 mA cm^{-2}, 14.25 mA cm^{-2}, 19.60 mA cm^{-2} and 19.82 mA cm^{-2}, respectively. The largest absolute increase in J_{sc} observed was for the DSSC with gold nanoparticles. Overall, the presence of nanoparticles led to increase in current density and corresponds to increase in efficiency. This gain was a direct result of improved light capture that

increased the J_{sc} value; note that the V_{oc} was mostly unchanged, and this contribute to efficiency gains. The fabrication of such a device was a success. A typical PV cell without nanoparticles had a V_{oc} = 0.69 V, J_{sc} = 9.90 mA cm^{-2}, FF = 67% and efficiency of 4.59%. Upon the formation of a nanoparticle array over the surface of the cell, an increase in light collection was measured and $I-V$ measurements that showed increase in the photo generated current. The formation of nanoparticles onto the cells did not reduce the V_{oc} so much and a subsequent increase in device efficiency occurred. The largest measured absolute increase in J_{sc} was 19.82 mA cm^{-2}. To the best of the author's knowledge, this work marks the largest increase in photocurrent density measured in a plasmon enhanced PV cell to date. The PV cells presented in this chapter are of high enough quality to successfully demonstrate plasmon enhanced absorption. It is however possible to develop this cell further. Improving the V_{oc} basically for copper nanoparticles–based cell could make the largest impact on device efficiency.

Table 8.2: The electron transport time time (τ_{tr}), electron recombination time (τ_{rec}), charge collection efficiency (η_{cc}), for DSSCs fabricated with different nanoparticles.

Nobel metals	τ_{rec} (ms)	τ_{tr} (ms)	η_{cc}
Without NP (0 wt.%)	36.43 ± 2.19	17.13 ± 0.64	0.53 ± 0.03
Au NP (3 wt.%)	115.33 ± 4.16	7.32 ± 0.63	0.94 ± 0.01
Ag NP (2 wt.%)	87.22 ± 9.17	7.00 ± 0.41	0.92 ± 0.01
Cu NP (3 wt.%)	143.19 ± 13.81	2.30 ± 0.07	0.98 ± 0.01
Pt NP (3 wt.%)	3.24 ± 0.13	0.84 ± 0.05	0.74 ± 0.01

Table 8.2 displays the electron transport time, τ_{tr} through the pores of the anode to the back layer and the electron recombination time, τ_{rec} which indicated the degradation of DSSCs efficiency. The τ_{tr} is lower (7.32 ms) and the τ_{rec} is higher (115.33 ms) for gold

nanoparticles based DSSCs which confirmed its superiority in electron transferring ability through TiO_2 surface to FTO substrate that could lead to the best cell efficiency compared to without NPs DSSC. The τ_{tr} is much higher than τ_{rec} which means that the transport of photo−excited electrons in TiO_2 was fast enough preventing the electrons from undergoing recombination. A good solar cell must have such electrodynamics character. The charge collection efficiency (η_{cc}), for the gold nanoparticle showed the highest values of 0.94 compared to without NPs DSSC. Copper nanoparticle based DSSC has efficiency increment over platinum based DSSC. Copper nanoparticle based DSSC has shown higher charge collection efficiency (η_{cc}) compared to platinum based DSSC as well as higher recombination time of electron to transport to TiO_2. All the results have been found to show well conceivable with other DSSC and electrochemical characterizations. Also, it indicates that the DSSC fabricated with gold nanoparticles based DSSCs is best to other DSSCs in the present investigation.

Comparison of the IMPS and IMVS results revealed that the electron transport time, τ_{tr} increased by 95 % and electron recombination time, τ_{rec} decreased by 75% from Ag NP to Au NP which indicated the efficient electron transport ability and reduced electron recombination tendency for their corresponding DSSCs. The τ_{tr} and τ_{rec} showed 42% increment and 31% decrement, respectively from Au NP to without NP based DSSCs which further supports the superiority of the DSSC of Au NP based cells over without NP based DSSCs. Again, the τ_{tr} and τ_{rec} showed 40% increment, and 41% decrement respectively from Ag NP to without NP based DSSCs which further supports the superiority of the DSSC of Ag NP based cells over without NP based DSSCs. Furthermore, the charge collection efficiency, increased based on gold nanoparticles, silver nanoparticles and without nanoparticle based DSSCs followed by 0.94, 0.92, and 0.53, respectively.

CHAPTER: 9 CONCLUSIONS AND SUGGESTIONS FOR FUTURE WORK

9.1   Conclusions

To achieve the objectives related to the preparation and characterization of Nanoparticles coated photoanode based DSSCs, firstly four types of nanoparticles such as gold, silver, copper and platinum photoanode were prepared and characterized by $J-V$, IMVS and IMVS techniques. Au NPs is shown significant effect in DSSCs application. The cell with 3 wt.% composite exhibited with 8.54 % efficiency which is the best performance among other cells. The cell with photoanode containing 3 wt.% Au NPs exhibited the highest J_{sc} of 19.82 mA cm^{-2}, V_{oc} of 0.72 V and FF of 0.60%. The cell also exhibited electron transport time, τ_{tr} of 7.32 ms and recombination time, τ_{rec} of 115.33 ms. We have fabricated solar cells using N3 dye. The top layer of the DSSCs consists of TiO$_2$ and Ag nanoparticles. The highest efficiency for Ag NP based DSSC was exhibited by 2 wt.% Ag nanoparticles. This is ascribed to the close optical matching between the two visible absorptions of N3 dye and the LSPR of Ag NPs. This is the evidence of plasmon−enhanced absorption in DSSCs with metal nanoparticles. In addition, it is suggested that metal nanoparticle aggregation be controlled to improve surface plasmon−enhanced DSSC performance. Under 100 mW cm^{-2} light irradiation, the DSSC with Ag added TiO$_2$ photoanode showed an improved light−to−electrical efficiency of 6.99%. Without Ag nanoparticles the efficiency was only 4.59 %. The Ag nanoparticles increased visible light absorption due to the surface plasmon effect that helped to improve photovoltaic efficiency. Additionally, these Ag nanoparticles dramatically enhanced interfacial charge transfer that reduced charge recombination. The 2 wt.% Ag content in TiO$_2$ was discovered to be the ideal level for creating an effective photoanode. The synergistic effects of Ag nanoparticles, the effect of surface plasmon,

band gap narrowing, and efficient charge transport improved photocurrent production and conversion efficiency of the DSSC.

Cu NP have proved to be one of the efficient materials in TiO_2 photoanode layer to reduce the electron recombination rate in DSSCs. Solar cell with 3 wt.% of Cu NP gave the best performance with the value of 7.19% and is higher compared to the sample without Cu NP (4.59%).

The IMPS and IMVS results revealed that the electron transport time, τ_{tr} increased by 95% and electron recombination time, τ_{rec} decreased by 75% from Ag NP to Au NP which indicated the efficient electron transfer ability and reduced electron recombination tendency for their corresponding DSSCs. The τ_{tr} and τ_{rec} showed 42% increment and 31% decrement, respectively from Au NP to without NP based DSSCs which further supports the superiority of the DSSC of Au NP based cells over without NP based DSSCs. Again, the τ_{tr} and τ_{rec} showed 40% increment, and 41% decrement respectively from Ag NP to without NP based DSSCs which further supports the superiority of the DSSC of Ag NP based cells over without NP based DSSCs. Furthermore, the charge collection efficiency, increased based on without nanoparticle, silver nanoparticles and gold nanoparticles based DSSCs followed by 0.53, 0.92 and 0.94 respectively. Objectives related to the studies of electron transport properties of the DSSCs fabricated with these nanoparticles has been fulfilled by the $J-V$, IMPS and IMVS analysis.

9.2 Suggestions for Future Work

The present study has developed some thoughts for future dimension of research. For the continuation of this research in future, some suggestions can be made based on the findings/insights of the present work.

- The noble metals like ruthenium, rhodium, palladium, osmium, iridium nanoparticle systems will enrich the literature.

- Nanoparticles alloy can be doped in the photoanode system for further enhancement of DSSC efficiency.

- Modeling and simulation of the $J-V$ characteristics of these nobel metals based DSSCs can contribute to the knowledge of DSSC study.

- Other side, molecular or atomic interaction also need to understand among photo induced electrons and long−life stability of DSSCs performance to get a more comprehensive understanding of the plasmonic effect in DSSC performance.

- The effect of plsmonic surface resonance or localized surface resonance on electron trapping−detrapping of the DSSCs can be studied.

REFERENCES

Ahuja, D., & Tatsutani, M. (2009). Sustainable energy for developing countries. *Surveys and Perspectives Integrating Environment and Society*, 2, 1.

Ali, A., El−Mellouhi, F., Mitra, A., & Aïssa, B. (2022). Research progress of plasmonic nanostructure−enhanced photovoltaic solar cells. *Nanomaterials*, 12(5), 788.

Atwater, H. A., & Polman, A. (2010). Plasmonics for improved photovoltaic devices. *Nature Materials*, 9(3), 205−213.

Bagher, A. M., Vahid, M. M. A., & Mohsen, M. (2015). Types of solar cells and application. *American Journal of optics and Photonics*, 3(5), 94−113.

Barnes, W. L., Dereux, A., & Ebbesen, T. W. (2003). Surface plasmon subwavelength optics. *Nature*, 424(6950), 824−830.

Binks, B., Stenekes, N., Kruger, H., & Kancans, R. (2018). Australian Bureau of Agricultural and Resource Economics (ABARES) Insights: *Snapshot of Australia's Agricultural Workforce*. Department of Agriculture: Canberra, Australia.

Breidenich, C., Magraw, D., Rowley, A., & Rubin, J. W. (1998). The Kyoto protocol to the United Nations framework convention on climate change. *American Journal of International Law*, 92(2), 315−331.

Brown, M.D., Suteewong, T., Kumar, R.S.S.K., D'Innocenzo, V., Petrozza, A., Lee, M.M., Wiesner, U., & Snaith, H.J. (2011). Plasmonic dye−sensitized solar cells using core−shell metal−insulator nanoparticles. *Nano Letters*, 11(2), 438–445.

Byrne, O., Ahmad, I., Surolia, P. K., Gun'ko, Y. K., & Thampi, K. R. (2014). The optimisation of dye sensitised solar cell working electrodes for graphene and SWCNTs containing quasi−solid state electrolytes. *Solar energy*, 110, 239−246.

Catchpole, K. A., & Polman, A. (2008). Plasmonic solar cells. *Optics Express*, 16(26), 21793−21800.

Chandrasekharan, N., & Kamat, P. V. (2001). Assembling gold nanoparticles as nanostructured films using an electrophoretic approach. *Nano Letters*, 1(2), 67−70.

Chopra, K. L., Paulson, P. D., & Dutta, V. (2004). Thin-film solar cells: an overview. *Progress in Photovoltaics: Research and Applications*, 12(2−3), 69−92.

Conibeer G., & Willoughby, A. (2014). Solar cell materials: developing technologies. John Wiley & Sons Ltd, Chichester, UK.

Costa, R. D., Lodermeyer, F., Casillas, R., & Guldi, D. M. (2014). Recent advances in multifunctional nanocarbons used in dye−sensitized solar cells. *Energy & Environmental Science*, 7(4), 1281−1296.

Dao, V. D., & Choi, H. S. (2016). Highly−efficient plasmon−enhanced dye−sensitized solar cells created by means of dry plasma reduction. *Nanomaterials*, 6(4), 70.

Desilvestro, J., Graetzel, M., Kavan, L., Moser, J., & Augustynski, J. (1985). Highly efficient sensitization of titanium dioxide. *Journal of the American Chemical Society*, 107(10), 2988−2990.

Dhonde, M., Sahu, K., Murty, V. V. S., Nemala, S. S., & Bhargava, P. (2017). Surface plasmon resonance effect of Cu nanoparticles in a dye sensitized solar cell. *Electrochimica Acta*, 249, 89−95.

Ding, Y., Sheng, J., Yang, Z., Jiang, L., Mo, L.E., Hu, L., Que, Y. and Dai, S., (2016). High Performance Dye−Sensitized Solar Cells with Enhanced Light−Harvesting Efficiency Based on Polyvinylpyrrolidone−Coated Au−TiO$_2$ Microspheres. *ChemSusChem*, 9(7), 720−727.

Dissanayake, M. A. K. L., Umair, K., Senadeera, G. K. R., & Kumari, J. M. K. W. (2021). Effect of electrolyte conductivity, co−additives and mixed cation iodide salts on efficiency enhancement in dye sensitized solar cells with acetonitrile−free electrolyte. *Journal of Photochemistry and Photobiology A: Chemistry*, 415, 113308.

Duan, H., Wang, T., Su, Z., Pang, H., & Chen, C. (2022). Recent progress and challenges in plasmonic nanomaterials. *Nanotechnology Reviews*, 11(1), 846−873.

Dudley, B. (2014, June). BP statistical review of world energy 2014. In World Petroleum Conference, Moscow (Vol. 16).

Erwin, W. R., Zarick, H. F., Talbert, E. M., & Bardhan, R. (2016). Light trapping in mesoporous solar cells with plasmonic nanostructures. *Energy & Environmental Science*, 9(5), 1577−1601.

Fang, Y., Ma, P., Cheng, H., Tan, G., Wu, J., Zheng, J., Zhou, X., Fang, S., Dai, Y. & Lin, Y., (2019). Synthesis of Low−Viscosity Ionic Liquids for Application in Dye−Sensitized Solar Cells. *Chemistry−An Asian Journal*, 14(23), 4201−4206.

Feldman, D., Barbose, G., Margolis, R., Bolinger, M., Chung, D., Fu, R., Seel, J., Davidson, C., Darghouth, N., & Wiser, R. (2015). Photovoltaic system pricing trends: historical, recent, and near−term projections 2015 edition. *National Renewable Energy Laboratory*.

Ferrere, S., Zaban, A., & Gregg, B. A. (1997). Dye sensitization of nanocrystalline tin oxide by perylene derivatives. *Journal of Physical Chemistry B*, 101(23), 4490−4493.

Ferry, V. E., Sweatlock, L. A., Pacifici, D., & Atwater, H. A. (2008). Plasmonic nanostructure design for efficient light coupling into solar cells. *Nano Letters*, 8(12), 4391−4397.

Fröhlich, C., & Lean, J. (2004). Solar radiative output and its variability: evidence and mechanisms. *Astronomy and Astrophysics Review*, 12(4), 273−320.

Gangadharan, D. T., Xu, Z., Liu, Y., Izquierdo, R., & Ma, D. (2017). Recent advancements in plasmon−enhanced promising third−generation solar cells. *Nanophotonics*, 6(1), 153−175.

Gao, R., Wang, L., Geng, Y., Ma, B., Zhu, Y., Dong, H., & Qiu, Y. (2011). Interface modification effects of 4−tertbutylpyridine interacting with N3 molecules in quasi−solid dye−sensitized solar cells. *Physical Chemistry Chemical Physics*, 13(22), 10635−10640.

Garnett, E. C., Brongersma, M. L., Cui, Y., & McGehee, M. D. (2011). Nanowire solar cells. *Annual Review of Materials Research*, 41, 269−295

Gong, J., Liang, J., & Sumathy, K. (2012). Review on dye−sensitized solar cells (DSSCs): Fundamental concepts and novel materials. *Renewable and Sustainable Energy Reviews*, 16(8), 5848−5860.

Gong, X., Nie, Z., Wang, Z., Cui, S., Gao, F., & Zuo, T. (2012). Life cycle energy consumption and carbon dioxide emission of residential building designs in Beijing: A comparative study. *Journal of Industrial Ecology*, 16(4), 576−587.

Gorlov, M., & Kloo, L. (2008). Ionic liquid electrolytes for dye−sensitized solar cells. *Dalton Transactions*, (20), 2655−2666.

Grätzel, M. (2009). Recent advances in sensitized mesoscopic solar cells. *Accounts of Chemical Research*, 42(11), 1788−1798.

Gwamuri, J., Güney, D. Ö., & Pearce, J. M. (2013). Advances in Plasmonic Light Trapping in Thin-Film Solar Photovoltaic Devices. *Solar Cell Nanotechnology*, 241−269.

Hagfeldt, A., & Grätzel, M. (2000). Molecular photovoltaics. *Accounts Of Chemical Research*, 33(5), 269−277.

Hagfeldt, A., Boschloo, G., Sun, L., Kloo, L., & Pettersson, H. (2010). Dye−sensitized solar cells. *Chemical Reviews*. 110, 6595–6663.

Hameed, S., & Dignon, J. (1988). Changes in the geographical distributions of global emissions of NOx and SOx from fossil−fuel combustion between 1966 and 1980. *Atmospheric Environment* (1967), 22(3), 441−449.

Hara, K., & Koumura, N. (2009). Organic dyes for efficient and stable dye−sensitized solar cells. *Material Matters*, 92(4), 1−4.

Huang, P. C., Chen, T. Y., Wang, Y. L., Wu, C. Y., & Lin, T. L. (2015). Improving interfacial electron transfer and light harvesting in dye−sensitized solar cells by using Ag nanowire/TiO_2 nanoparticle composite films. *RSC Advances*, 5(86), 70172−70177.

Hwang, H. J., Joo, S. J., Patil, S. A., & Kim, H. S. (2017). Efficiency enhancement in dye−sensitized solar cells using the shape/size−dependent plasmonic nanocomposite photoanodes incorporating silver nanoplates. *Nanoscale*, 9(23), 7960−7969.

Iftikhar, H., Sonai, G. G., Hashmi, S. G., Nogueira, A. F., & Lund, P. D. (2019). Progress on electrolytes development in dye−sensitized solar cells. *Materials*, 12(12), 1998.

Jang, Y. H., Jang, Y. J., Kim, S., Quan, L. N., Chung, K., & Kim, D. H. (2016). Plasmonic solar cells: from rational design to mechanism overview. *Chemical Reviews*, 116(24), 14982−15034.

Jean, B.X. A., Li, X., Law, C., Barnes, P. R. F., Humphry−Baker, R., Lund, P., Asghar, M.I., & O'Regan, B. C. (2014). Rediscovering a key interface in dye−sensitized solar cells: guanidinium and iodine competition for binding sites at the dye/electrolyte surface. *Journal of the American Chemical Society*, 136(20), 7286−7294.

Jia, Z., Li, J., Gao, L., Yang, D., & Kanaev, A. (2023). Dynamic Light Scattering: A Powerful Tool for In Situ Nanoparticle Sizing. *Colloids and Interfaces*, 7(1), 15.

Jiang, R., Li, B., Fang, C., & Wang, J. (2014). Metal/semiconductor hybrid nanostructures for plasmon-enhanced applications. *Advanced Materials*, 26(31), 5274−5309.

Judkins, R. R., Fulkerson, W., & Sanghvi, M. K. (1993). The dilemma of fossil fuel use and global climate change. *Energy & Fuels*, 7(1), 14−22.

Katoh, R., Kasuya, M., Kodate, S., Furube, A., Fuke, N., & Koide, N. (2009). Effects of 4−tert−butylpyridine and Li ions on photoinduced electron injection efficiency in black−dye−sensitized nanocrystalline TiO2 films. The *Journal of Physical Chemistry C*, 113(48), 20738−20744.

Kojima, A., Teshima, K., Shirai, Y., & Miyasaka, T. (2009). Organometal halide perovskites as visible−light sensitizers for photovoltaic cells. *Journal of the American Chemical Society*, 131(17), 6050−6051.

Kong, F., Dai, S., & Wang, K. (2005). Dye sensitizers used in dye sensitized solar cells. *Huaxue Tongbao*, 68(5), 338−345.

Kopidakis, N., Neale, N. R., & Frank, A. J. (2006). Effect of an adsorbent on recombination and band−edge movement in dye−sensitized TiO_2 solar cells: evidence for surface passivation. *Journal of Physical Chemistry B*, 110(25), 12485−12489.

Krč, J., Lipovšek, B., & Topič, M. (2012). Light management in thin−film solar cell. *In Next Generation of Photovoltaics: New Concepts* (pp. 95−129). Berlin, Heidelberg: Springer Berlin Heidelberg.

Kumar, Y., Chhalodia, T., Bedi, P. K. G., & Meena, P. L. (2023). Photoanode modified with nanostructures for efficiency enhancement in DSSC: a review. *Carbon Letters*, 33(1), 35−58.

Kunwar, S., Pandey, P., & Lee, J. (2019). Enhanced localized surface plasmon resonance of fully alloyed AgAuPdPt, AgAuPt, AuPt, AgPt, and Pt nanocrystals: systematical investigation on the morphological and LSPR properties of mono−, bi−, tri−, and quad−metallic nanoparticles. *ACS Omega*, 4(17), 17340−17351.

Lal, S., Link, S., & Halas, N. J. (2007). Nano−optics from sensing to waveguiding. *Nature Photonics*, 1(11), 641−648.

Lameirinhas, R. A.M., Torres, J. P. N., & de Melo Cunha, J. P. (2022). A photovoltaic technology review: history, fundamentals and applications. *Energies*, 15(5), 1823.

Lee, C. P., Li, C. T., & Ho, K. C. (2017). Use of organic materials in dye−sensitized solar cells. *Materials Today*, 20(5), 267−283.

Lee, M. M., Teuscher, J., Miyasaka, T., Murakami, T. N., & Snaith, H. J. (2012). Efficient hybrid solar cells based on meso−super structured organometal halide perovskites. *Science*, 338(6107), 643−647.

Li, X., Yang, W., Deng, J., & Lin, Y. (2023). Surface plasmon resonance effects of silver nanoparticles in graphene−based dye−sensitized solar cells. *Frontiers in Materials*, 10, 1137771.

Liang, Z., Sun, J., Jiang, Y., Jiang, L., & Chen, X. (2014). Plasmonic enhanced optoelectronic devices. *Plasmonics*, 9, 859−866.

Lim, S. P., Pandikumar, A., Huang, N. M., & Lim, H. N. (2014). Enhanced photovoltaic performance of silver @ titania plasmonic photoanode in dye−sensitized solar cells. *RSC Advances*, 4(72), 38111−38118.

Lin, K. T., Lin, H., & Jia, B. (2020). Plasmonic nanostructures in photodetection, energy conversion and beyond. *Nanophotonics*, 9(10), 3135−3163.

Link, S., & El−Sayed, M. A. (1999). Spectral properties and relaxation dynamics of surface plasmon electronic oscillations in gold and silver nanodots and nanorods. *Journal of Physical Chemistry B*, 103(40), 8410−8426.

Liu, L., Zhang, X., Yang, L., Ren, L., Wang, D., & Ye, J. (2017). Metal nanoparticles induced photocatalysis. *National Science Review*, 4(5), 761−780.

Losurdo, M., Moreno, F., Cobet, C., Modreanu, M., & Pernice, W. (2021). Plasmonics: Enabling functionalities with novel materials. *Journal of Applied Physics*, 129(22), 220401

Louis, C., & Pluchery, O. (2012). Gold nanoparticles for physics, chemistry and biology. Imperial College Press, London. World Scientific

Luan, X., & Wang, Y. (2014). Plasmon−enhanced performance of dye−sensitized solar cells based on electrodeposited Ag nanoparticles. *Journal of Materials Science & Technology*, 30(1), 1−7.

Mathew, S., Yella, A., Gao, P., Humphry−Baker, R., Curchod, B.F., Ashari−Astani, N., Tavernelli, I., Rothlisberger, U., Nazeeruddin, M.K. & Grätzel, M., (2014). Dye−sensitised solar cells with 13% efficiency achieved through the molecular engineering of porphyrin sensitisers. *Nature Chemistry*, 6(3), 242–247.

Millington, K. R., Fincher, K. W., & King, A. L. (2007). Mordant dyes as sensitisers in dye−sensitised solar cells. *Solar Energy Materials and Solar Cells*, 91(17), 1618−1630.

Nazeeruddin, M. K., Kay, A., Rodicio, I., Humphry−Baker, R., Müller, E., Liska, P., Vlachopoulos, N. & Grätzel, M., (1993). Conversion of light to electricity by cis−X_2 bis(2, 2'−bipyridyl−4, 4'−dicarboxylate) ruthenium (II) charge−transfer

sensitizers (X= Cl−, Br−, I−, CN−, and SCN−) on nanocrystalline titanium dioxide electrodes. *Journal of the American Chemical Society*, 115(14), 6382−6390.

Nazeeruddin, M. K., Zakeeruddin, S. M., Humphry−Baker, R., Jirousek, M., Liska, P., Vlachopoulos, N., Shklover, V., Fischer, C. H. & Grätzel, M., (1999). Acid−Base equilibria of (2, 2 '−Bipyridyl−4, 4 '−dicarboxylic acid) ruthenium (II) complexes and the effect of protonation on charge−transfer sensitization of nanocrystalline titania. *Inorganic Chemistry*, 38(26), 6298−6305.

NREL Best Research−Cell Efficiency Chart 2022. [(accessed on 15 September 2023)]; Available online: https://www.nrel.gov/pv/assets/pdfs/best−research−cell−efficiencies. pdf

Nusbaumer, H., Moser, J. E., Zakeeruddin, S. M., Nazeeruddin, M. K., & Grätzel, M. (2001). Co^{II} $(dbbip)_2^{2+}$ complex rivals tri−iodide/iodide redox mediator in dye−sensitized photovoltaic cells. *Journal of Physical Chemistry B*, 105(43), 10461−10464.

O'Regan, B., & Gratzel, M. (1991). A low−cost, high−efficiency solar cell based on dye−sensitised colloidal TiO_2 films. *Nature*, 6346(53), 737−740.

Olaimat, M. M., Yousefi, L., & Ramahi, O. M. (2021). Using plasmonics and nanoparticles to enhance the efficiency of solar cells: review of latest technologies. *Journal Optical Society Amirica B*, 38(2), 638−651.

Oskam, G., Bergeron, B.V., Meyer, G.J., & Searson, P.C. (2001). Pseudohalogens for dye sensitised TiO_2 photo electrochemical cell. *Journal of Physical Chemistry B*, 105, 6867–6873.

Pastuszak, J., & Węgierek, P. (2022). Photovoltaic cell generations and current research directions for their development. Materials, 15(16), 5542.

Peedikakkandy, L., & Bhargava, P., (2016). A Study of photocurrent enhancement by Au, Ag and Cu nanoparticles in dye sensitized solar cells. *Advanced Science Letters*, 22(4), 958−963.

Pelton, M., & Bryant, G. W. (2013). Introduction to metal−nanoparticle plasmonics. John Wiley & Sons, Ltd, ProQuest E−book Central.

Peter, A. A., & Alkaisi, M. M. (2019). Nanostructures for light trapping in thin film solar cells. *Micromachines*, 10(9), 619.

Pillai, S., & Green, M. A., (2010). Plasmonics for photovoltaic applications. *Solar Energy Materials and Solar Cells*, 94, 1481–1486.

Qureshi, A. A., Javed, S., Javed, H. M. A., Akram, A., Jamshaid, M., & Shaheen, A. (2020). Strategic design of Cu/TiO_2−based photoanode and $rGO−Fe_3O_4$−based counter electrode for optimized plasmonic dye−sensitized solar cells. *Optical Materials*, 109, 110267.

Ravindran, A., Chandran, P., & Khan, S.S. (2013). Bio functionalised silver nanoparticles: advances and prospects. *Colloids Surface B: Biointerfaces*, 105(1), 342–352.

Rhee, J. H., Chung, C. C., & Diau, E. W. G. (2013). A perspective of mesoscopic solar cells based on metal chalcogenide quantum dots and organometal−halide perovskites. *NPG Asia Materials*, 5(10), e68−e68.

Rho, W.−Y., Song, D.H.,Yang, H.−Y., Kim, H.−S., Son, B. S.,Suh, J.S., & Jun, B.−H. (2018). Recent advances in plasmonic dye−sensitised solar cells. *Journal of Solid State Chemistry*, 258, 271−282.

Rodríguez, R., Vargas, S., Castaño, V., & Santamaría−Holek, I. (2021). Electrical response of optimized DSSC's by different dye−mordant−assistant combinations: A multi−time−hierarchical theoretical approach. *Results in Physics*, 23, 104064.

Rowell, M. W., & McGehee, M. D. (2011). Transparent electrode requirements for thin film solar cell modules, *Energy Environmental Science*, 4, 131−134.

Schmalensee, R., Bulovic, V., Armstrong, R., Batlle, C., Brown, P., Deutch, J., Jacoby, H., Jaffe, R., Jean, J., Miller, R., O'Sullivan, F., Parsons, J., Perez−Arriaga, J. I., Seifkar, N., Stoner, R., & Vergara C. (2015). The future of solar energy: An interdisciplinary MIT study. Massachusetts Institute of Technology, MIT Energy Initiative.

Schuller, J. A., Barnard, E. S., Cai, W., Jun, Y. C., White, J. S., & Brongersma, M. L. (2010). Plasmonics for extreme light concentration and manipulation. *Nature Materials*, 9, 193–204.

Selopal, G.S., Wu, H.P., Lu, J., Chang, Y.C., Wang, M., Vomiero, A., Concina, I. & Diau, E.W.G., (2016). Metal−free organic dyes for TiO_2 and ZnO dye−sensitized solar cells. *Scientific Reports*, 6(1), 18756.

Shah, S., Abidin, Z. H. Z., Noor, I. M., Osman, Z., & Arof, A. K. (2023). Performance improvement of dye−sensitized solar cells with Ag nanoparticles. *Molecular Crystals and Liquid Crystals*, 1−11.

Shah, S., Noor, I. M., Pitawala, J., Albinson, I., Bandara, T. M. W. J., Mellander, B. −E., & Arof, A. K. (2017). Plasmonic effects of quantum size metal nanoparticles on dye−sensitised solar cell. *Optical Materials Express*, 6(7), 2069.

Shalini, S., Balasundaraprabhu, R., Kumar, T.S., Prabavathy, N., Senthilarasu, S., & Prasanna, S. (2016). Status and outlook of sensitisers/dyes used in dye sensitised solar cells (DSSC): a review, *International Journal of Energy Research*. 40, 1303–1320.

Sharma, K., Sharma, V., & Sharma, S. S. (2018). Dye−sensitized solar cells: fundamentals and current status. *Nanoscale Research Letters*, 13, 1−46.

Sima, C., Grigoriu, C., & Antohe, S. (2010). Comparison of the dye−sensitized solar cells performances based on transparent conductive ITO and FTO. *Thin Solid Films*, 519(2), 595−597.

Smestad, G. P., & Gratzel, M. (1998). Demonstrating electron transfer and nanotechnology: a natural dye−sensitized nanocrystalline energy converter. *Journal of Chemical Education*, 75(6), 752.

Solar spectrum (available from: https://en.wikipedia.org/wiki/File:Solar_spectrum_en.svg)

Sovizi, M., & Omrani, M. K. (2017). Design and simulation of high sensitive cylindrical nanogear shell sensors according to localized surface plasmon resonance. *Optik*, 144, 300−307.

Streets, D. G., & Waldhoff, S. T. (2000). Present and future emissions of air pollutants in China:SO_2, NOx, and CO. *Atmospheric Environment*, 34, 363–374.

Stuart, H., & Hall, D. (1996). Absorption enhancement in silicon−on−insulator waveguides using metal island films. *Applied Physics Letter*, 69, 2327–2329.

Subas, M., Onkar, G., Vivek, D., Vijayamohanan, K., Bogle, K. A., Valanoor, N., & Satishchandra B. O. (2012). TiO_2–Au plasmonic nanocomposite for enhanced dye−sensitised solar cell (DSSC) performance. *Solar Energy*, 86, 1428–1434.

Sugathan, V., John, E., & Sudhakar, K. (2015). Recent improvements in dye sensitised solar cells: a review, *Renewable and Sustainable Energy Reviews*. 52, 54–64.

Swami, R. (2012). Solar cell. *International Journal of Scientific and Research Publications*, 2(7), 1−5.

Teo, L. P., Akub, M. K., Buraidah, M. H. (2019). Boosting the efficiency of dye−sensitised TiO_2 solar cells using plasmonic gold nanoparticles. *Materials Today: Proceedings*, 17, 465–471.

Thomas, S., Deepak, T. G., Anjusree, G. S., Arun, T. A., Nair, S. V. & Nair, A. S. (2014). A review on counter electrode materials in dye−sensitised solar cells. *Journal of Materials Chemistry A*, 2, 4474–4490.

Toivola, M. (2010). Dye−sensitised solar cells on alternative substrates, TKK dissertations, 214.

Tributsch, H., & Calvin, M. (1971). Electrochemistry of Excited Molecules: Photo−Electrochemical Reactions of Chlorophylls. *Photochemical: Photobiology*, 14, 95–112.

Twidell, J., & Weir, T. (2015). Renewable energy resources. routledge. U.S. energy information administration. (2012). *International energy statistics.* Retrieved October 18, eBook ISBN978131576641.

Victoria, M., Haegel, N., Peters, I. M., Sinton, R., Jäger−Waldau, A., Canizo, C. D., Breyer, C., Stocks, M., Blakers, A., Kaizuka, I., Komoto, K., & Smets, A. (2021). Solar photovoltaics is ready to power a sustainable future. *Joule*, 5, 1041–1056.

Villalva, M. G., Gazoli J. R. & Ruppert, E. F., (2009). Comprehensive Approach to modelling simulation of photovoltaic arrays, *IEEE Transactions on Power Electronics*, 24(5), 1198– 1208.

Wang, L., Liu, H., Konic, R., Misewich, J., & Wang, S. (2013). Carbon nanotube−based hetero structures for solar energy applications, *Chemical Society Review*, 42, 8134–8156.

Wang, M., Anghel, A., Marsan, B., Ha, C., Pootrakulchote, N., Zakeeruddin, S., & Gratzel, M. (2009). CoS supersedes Pt as efficient electrocatalyst for triiodide reduction in dye−sensitized solar cells. *Journal of American Chemical Society*, 131, 15976–15977.

Wang, P., Zakeeruddin, S. M., Exnar, I., & Grätzel, M. (2002). High efficiency dye−sensitised nanocrystalline solar cells based on ionic liquid polymer gel electrolyte. *Chemical Communications*, 24(8), 2972−2973.

Wang, Y., Lu, J., Yin, J., Lü, G., Cui, Y., Wang, S., Deng, S., Shan, D., Tao, H., & Sun, Y. (2015). Influence of 4−tert−butylpyridine/guanidinium thiocyanate co−additives on band edge shift and recombination of dye−sensitized solar cells: experimental and theoretical aspects. *Electrochimica Acta*, 185, 69−75.

Wu, M., & Ma, T. (2014). Recent progress of counter electrode catalysts in dye−sensitized solar cells. *Journal of Physical Chemistry C*, 118, 16727–16742.

Wu, M., Lin, X., Wang, Y., Wang, L., Guo, W., Qu, D., Peng, X., Hagfeldt, A., Gratzel, M., & Ma, T. (2012). Economical Pt−free catalysts for counter electrodes of dye−sensitized solar cells. *Journal of American Chemical Society*, 134, 3419–3428.

Wurfel, P., & Wurfel, U. (2009). Physics of solar cells: From basic principles to advanced concepts. John Wiley & Sons, Hoboken.

Xiao, F. X. (2012). Layer−by−layer self−assembly construction of highly ordered metal−TiO$_2$ nanotube arrays heterostructures (M/TNTs, M=Au, Ag, Pt) with tunable catalytic activities. *Journal of Physical Chemistry C*, 116, 16487–16498.

Xie, Z. B., Midya, A., Loh, K. P., Adams, S., Blackwood, D. J., Wang, J., Zhang, X. J., & Chen, Z. K. (2010). Highly efficient dye-sensitized solar cells using phenothiazine derivative organic dyes. *Progress in Photovoltaics: Research and Applications*, 18(8), 573−581.

Yella, A., Lee, H. −W., Tsao, H. N., Yi, C., Chandiran, A. K., Nazeeruddin, M. K., Diau, E. W. −G., Yeh, C. −Y., Zakeeruddin, S. M., & Gratzel, M. (2011). Porphyrin−sensitized solar cells with cobalt (II/III)−based redox electrolyte exceed 12% efficiency. *Science*, 334, 629−635.

Yoshikawa, K., Kawasaki, H., Yoshida, W., Irie, T., Konishi, K., Nakano, K., Uto, T., Adachi, D., Kanematsu, M., Uzu, H. and Yamamoto, K., (2017). Silicon heterojunction solar cell with interdigitated back contacts for a photoconversion efficiency over 26%. *Nature Energy*, 2(5), 1−8.

Yousheng, C., Zhanghua, Z., Chao, L., Weibo, W., Xuesong, W., & Baowen, Z. (2005). Highly efficient co−sensitisation of nanocrystalline TiO2 electrodes with plural organic dyes. *New Journal Chemistry*, 29, 773−776.

Yu, Z., Gorlov, M., Boschloo, G., & Kloo, L. (2010). Synergistic effect of N−methylbenzimidazole and guanidinium thiocyanate on the performance of dye−sensitized solar cells based on ionic liquid electrolytes. *Journal of Physical Chemistry C* ,114 (50), 22330–22337.

Zhang, C., Huang, Y., Huo, Z., Chen, S., & Dai, S. (2009). Photoelectrochemical effects of guanidinium thiocyanate on dye−sensitized solar cell performance and stability. *Journal of Physical Chemistry C*, 113 (52), 21779–21783.

Zhang, H., Wang, C., Li, H., Jiang, L., Men, D., Wang, J., & Xiang, J (2018). Physical process−aided fabrication of periodic Au−M (M= Ag, Cu, Ag−Cu) alloyed nanoparticle arrays with tunable localized surface plasmon resonance and diffraction peaks. *Royal Society of Chemistry Advanced*, 8, 9134−9140

Zhang, Q., Zhou, S., Li, Q., & Li, H. (2015). Toward highly efficient CdS/CdSe quantum dot−sensitised solar cells incorporating a fullerene hybrid−nanostructure counter electrode on transparent conductive substrates. *Royal Society of Chemistry Advanced*, 5, 30617–30623.

Zhang, S., Yang, X., Zhang, K., Chen, H., Yanagida, M., & Han, L. (2011). Effects of 4−tert−butylpyridine on the quasi−fermi levels of TiO_2 films in the presence of different cations in dye−sensitized solar cells. *Physical Chemistry Chemical Physics*, 13, 19310–19313.

Zhou, L., Wei, L., Yang, Y., Xia, X., Wang, P., Yu, J., & Luan, T. (2016). Improved performance of dye sensitised solar cells using Cu−doped TiO_2 as photoanode materials: band edge movement study by spectroelectrochemistry. *Chemical Physics*, 475, 1−8.